INTERNATIONAL ATOMIC ENERGY AGENCY
UNITED NATIONS EDUCATIONAL, SCIENTIFIC AND CULTURAL ORGANIZATION
INTERNATIONAL CENTRE FOR THEORETICAL PHYSICS
I.C.T.P., P.O. BOX 586, 34100 TRIESTE, ITALY, CABLE CENTRATOM TRIESTE

UNITED NATIONS INDUSTRIAL DEVELOPMENT ORGANIZATION

INTERNATIONAL CENTRE FOR SCIENCE AND HIGH TECHNOLOGY

H4.SMR/540-29

Second Training College on Physics and Technology of Lasers and Optical Fibres

21 January - 15 February 1991

Switching & Modulation

A. Neyer
Universität Dortmund
Dortmund, Germany

SWITCHING AND MODULATION

A. Neyer

Universität Dortmund

OUTLINE

1) **Introduction**

2) **Interaction of light with matter**

3) **Physical effects** and basic devices for the modulation of light

- Electrooptics
- Acoustooptics
- Electroabsorption
- Electrorefraction
- Carrier injection
- Quantum effects

4) Integrated optic devices for **modulation and switching** of light

- Electrooptic devices
- Acoustooptic devices
- Semiconductor devices

5) Applications

- External modulation
- Switch arrays
- Coherent receivers

MOTIVATION

FOR OPTICAL MODULATION AND SWITCHING

- OPTICAL COMMUNICATIONS
  - Need for high frequency modulators to utilize the Terabit/sec information capacity of coherent light.
  - Need for optical switching in fiber optic networks for routing and multiplexing signals in the optical domain.
- OPTICAL SENSORS
  - Enhanced sensitivity in optical sensors especially in interferometric sensors by phasemodulation, frequency shifting etc.
- OPTICAL SIGNAL PROCESSING
  - Processing of optical signals by optical signals. → Need of optical bistable elem. → Opt. logic; Opt. computer; Opt. neur. netw.

MODULATION OF LIGHT

LIGHT: Coherent optical radiation

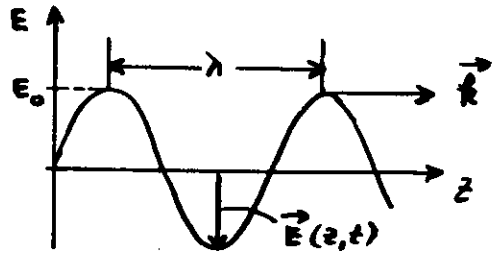

$$\vec{E}(\vec{r},t) = E_0\,\vec{e}\,\cos\underbrace{(\vec{k}\vec{r} - \omega t)}_{\varphi(\vec{r},t)} \qquad k = \frac{2\pi}{\lambda} n$$

MODULATION OF LIGHT:
Controlled change of one of the quantities of $\vec{E}$

- E_0 : Amplitude (AM/IM)
- $\vec{e}$: Polarization
- $\vec{k}$: Direction
- ω : Frequency (FM)
- φ : Phase (PM)

SWITCHING OF LIGHT

SWITCHING OF LIGHT:
Change of the local position of a light beam

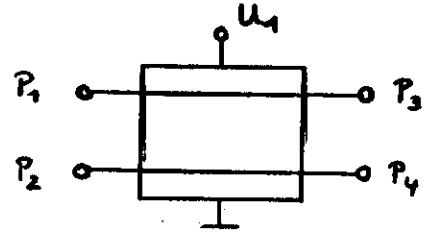

"STRAIGHT-THROUGH"- OR "BAR"- STATE : ⊖

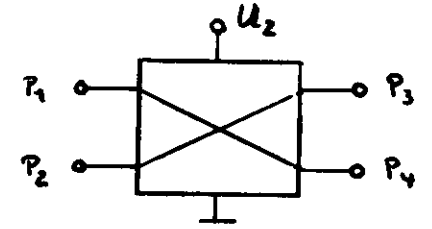

"CROSS"- STATE : ⊗

Characteristics of optical switches:

- Bidirectional
- Independent of data-rate and-format
- In general not digital

INTERACTION OF LIGHT WITH MATTER

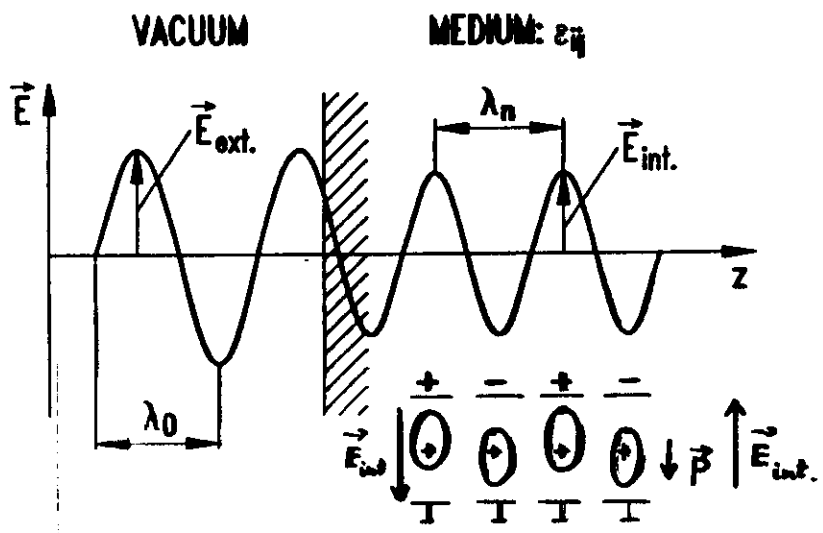

Induced polarization: $\vec{P} = \varepsilon_0 \chi \vec{E}_{in}$

Resulting electrical field in the medium is characterized by: $\vec{D} = \varepsilon_0 \vec{E}_{in} + \vec{P}$

$$\vec{D} = \varepsilon_0 \varepsilon \vec{E}_{in}$$

$$\varepsilon = 1 + \chi = n^2$$

INTERACTION OF LIGHT WITH MATTER

All information about the interaction of light with matter is contained in the (generally complex) refractive index:

$$\bar{n} = n - i\varkappa \qquad \alpha = \varkappa \frac{4\pi}{\lambda}$$

Example: The phase velocity of light in a medium:

$$v_p = c_0 / n$$

Changing of v_p implies a change of:

$$(n) \rightarrow \chi \rightarrow P/E$$

Changing of the polarization P requires a redistribution of bound charges (e.g. by strong electric fields) or a deformation of the ion lattice (e.g. by sound waves).

PHYSICAL EFFECTS FOR THE MODULATION AND SWITCHING OF LIGHT

MODULATION AND SWITCHING OF LIGHT
IMPLIES A
CHANGE OF THE REFRACTIVE INDEX !

PHYSICAL EFFECTS
causing a change of the refractive index :

- ELECTROOPTIC EFFECT
- ACOUSTOOPTIC EFFECT
- THERMOOPTIC EFFECT
- ELECTROABSORPTION
- ELECTROREFRACTION
- CARRIER INJECTION
- QUANTUM CONFINED STARK EFFECT
- OPTICAL CONTROL

THE ELECTROOPTIC EFFECT

The electrooptic effect describes the change of the refractive index of a medium in the presence of strong electric fields.

- Changing of n by electric fields requires a change of P/E by electric fields.
- Changing of P/E by electric fields implies a nonlinear dependence of P on E :

$$P(E) = \varepsilon_0 \left(\chi^{(1)} E + \chi^{(2)} E^2 + \chi^{(3)} E^3 + \dots \right)$$

$$P(E)/\varepsilon_0 E = \chi^{(1)} + \chi^{(2)} E + \chi^{(3)} E^2 + \dots \sim n(E)$$

- Strong electrooptic changes of n require $\chi^{(2)} \neq 0$.
- $\chi^{(2)} \neq 0$ is obtained only in crystals with no inversion symmetry.

POLARIZATION IN CRYSTALS WITH INVERSION SYMMETRY

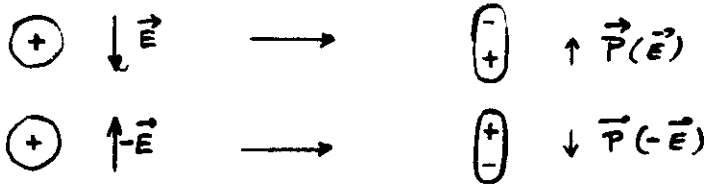

$$\rightarrow \quad \vec{P}(-\vec{E}) = -\vec{P}(\vec{E})$$

In crystals with inversion symmetry $\vec{P}$ must be an odd function of $\vec{E}$!

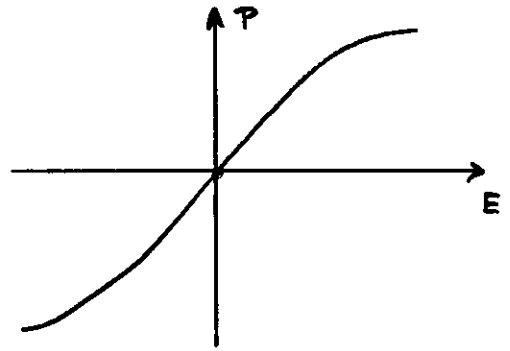

$$P(E) = \varepsilon_0 \left(\chi^{(1)} E + \chi^{(3)} E^3 + \cdots \right)$$

$$\chi^{(2)} = \chi^{(4)} = \cdots = 0$$

POLARIZATION IN CRYSTALS WITH NO INVERSION SYMMETRY

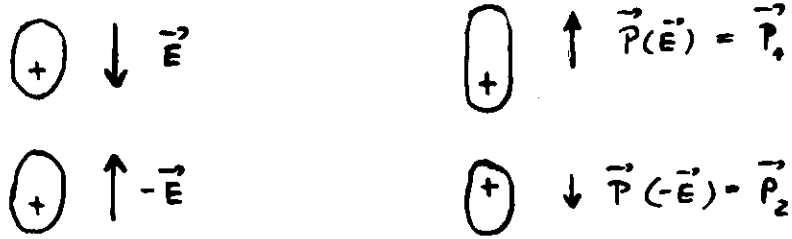

$$\rightarrow \quad \vec{P}(-\vec{E}) \neq -\vec{P}(\vec{E})$$

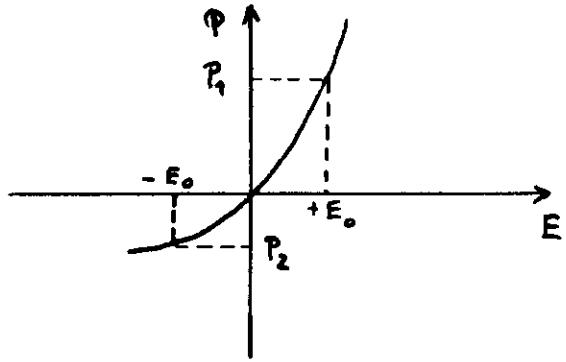

$$P(E) = \varepsilon_0 \left(\chi^{(1)} E + \chi^{(2)} E^2 + \chi^{(3)} E^3 + \cdots \right)$$

$\chi^{(2)}$ - EFFECTS REQUIRE CRYSTALS WITH NO INVERSION SYMMETRY!

How does the electrooptic effect change the properties of an incident light wave ?

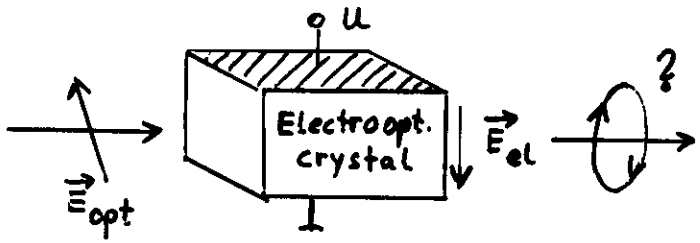

Δn_x , Δn_y , Δn_z ?

The answer is given by the

"INDEX ELLIPSOID"

THE INDEX ELLIPSOID

The light propagation in anisotropic media is determined by the energy density of the stored electrical field :

$$u_e = 1/2\ \vec{E}\,\vec{D} \qquad \vec{E} = \vec{D}/\varepsilon_0 n^2$$

$$2u_e\varepsilon_0 = \frac{D_x^2}{n_x^2} + \frac{D_y^2}{n_y^2} + \frac{D_z^2}{n_z^2}$$

with $\vec{D}/\sqrt{2u_e\varepsilon_0} = \vec{r}$

$$\frac{x^2}{n_x^2} + \frac{y^2}{n_y^2} + \frac{z^2}{n_z^2} = 1$$

"INDEX ELLIPSOID"

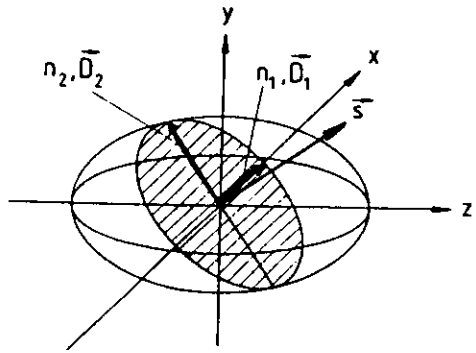

THE INDEX ELLIPSOID

Without applied electric field:

$$\boxed{\sum_i \eta_i x_i^2 = 1} \qquad i = 1,2,3 \;=\; x, y, z$$

with $\eta_i = 1/n_i^2$: Dielectric impermeability

with applied electric field:

$$\boxed{\sum_{ij} \eta_{ij}(\vec{E})\; x_i x_j = 1} \qquad i,j = 1,2,3$$

The change of the impermeability tensor η_{ij} under electrical fields is called:

ELECTROOPTIC EFFECT

$$\Delta\eta_{ij}(\vec{E}) = \eta_{ij}(\vec{E}) - \eta_{ij}(0) = \sum_k r_{ijk} E_k + \sum_{kl} s_{ijkl} E_k E_l$$

r_{ijk}: linear electrooptic $\sim \chi^{(2)}$ (POCKELS EFFECT)

s_{ijkl}: quadratic coefficient $\sim \chi^{(3)}$ (KERR EFFECT)

THE ELECTROOPTIC EFFECT

THE LINEAR ELECTROOPTIC COEFFICIENT:

r_{ijk}

- Component of induced polar.
- Component of inc. opt. field
- Component of appl. electr. field

ABBREVIATED NOTATION: r_{ik}

$11 = 1$
$22 = 2$
$33 = 3$
$23 = 32 = 4$
$13 = 31 = 5$
$12 = 21 = 6$

$$\begin{bmatrix} \Delta\eta_1 \\ \Delta\eta_2 \\ \Delta\eta_3 \\ \Delta\eta_4 \\ \Delta\eta_5 \\ \Delta\eta_6 \end{bmatrix} = \begin{bmatrix} r_{11} & r_{12} & r_{13} \\ r_{21} & r_{22} & r_{23} \\ r_{31} & r_{32} & r_{33} \\ r_{41} & r_{42} & r_{43} \\ r_{51} & r_{52} & r_{53} \\ r_{61} & r_{62} & r_{63} \end{bmatrix} \cdot \begin{bmatrix} E_1 \\ E_2 \\ E_3 \end{bmatrix}$$

THE ELECTROOPTIC EFFECT

INFLUENCE ON THE INDEX ELLIPSOID

$$\sum_{ij} \underbrace{\eta_{ij}(\vec{E})}_{\rightarrow \eta_{ij}(\vec{E}=0) + \sum_k r_{ijk} E_k} x_i x_j = 1$$

$$\left(\frac{1}{n_x^2} + r_{1k} E_k\right) x^2 + \left(\frac{1}{n_y^2} + r_{2k} E_k\right) y^2 + \left(\frac{1}{n_z^2} + r_{3k} E_k\right) z^2$$
$$+ 2yz\, r_{4k} E_k + 2zx\, r_{5k} E_k + 2xy\, r_{6k} E_k = 1$$

EFFECTS:

r_{1k}, r_{2k}, r_{3k}: change the length of the axes of the index ellipsoid

r_{4k}, r_{5k}, r_{6k}: lead to a rotation of the index ellipsoid

The new main axes of the index ellipsoid may be found by a coordinate transform. into the x', y', z' - system.

EXAMPLE 1: $LiNbO_3$

SYMMETRY GROUP 3m

Uniaxial crystal: $n_x = n_y = n_o$
$n_z = n_e$

Electrical field along z-axis: $E_k = E_z = E_3$

Electrooptic coefficients:

r_{13} ; $r_{23} = r_{13}$; r_{33} ; $r_{43} = r_{53} = r_{63} = 0$

$$\underbrace{\left(\frac{1}{n_o^2} + r_{13} E_z\right)}_{1/n_x'^2} x^2 + \left(\frac{1}{n_o^2} + r_{13} E_z\right) y^2 + \left(\frac{1}{n_z^2} + r_{33} E_z\right) z^2 = 1$$

$$n_x' = 1/\sqrt{\frac{1}{n_o^2} + r_{13} E_z} \simeq n_o \left(1 - \tfrac{1}{2} n_o^2 r_{13} E_z\right)$$

$$\Delta n_x' = n_x' - n_o = -\tfrac{1}{2} n_o^3 r_{13} E_z$$

$$\Delta n_y' = -\tfrac{1}{2} n_o^3 r_{13} E_z$$

$$\Delta n_z' = -\tfrac{1}{2} n_e^3 r_{33} E_z$$

ELECTROOPTIC PHASE MODULATOR

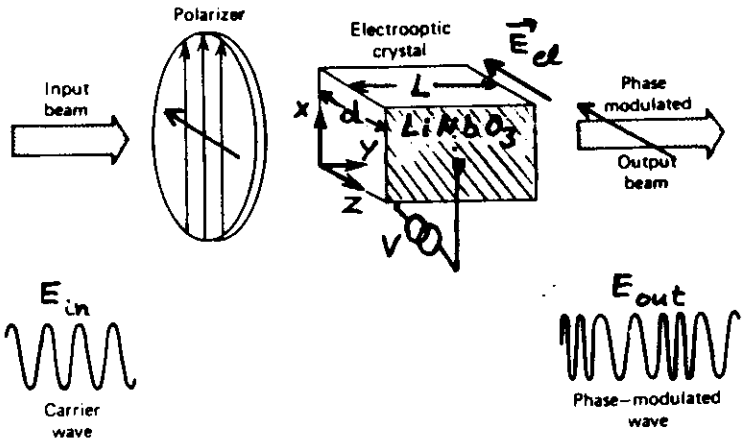

Electrooptically induced phase change:

$$\Delta\varphi(\vec{E}_{el}) = k_0 \cdot \Delta n(\vec{E}_{el}) \cdot L$$

$\vec{E}_{el} = (0,0,E_z)$: $\Delta\varphi_z(E_z) = k_0 n_e^3 r_{33} E_z/2 \cdot L$

$E_z = V/d$: $\boxed{\Delta\varphi_z(V) = \dfrac{\pi n_e^3 r_{33} V \cdot L}{d \cdot \lambda}}$

$$E_{in} = A \cdot \cos \omega t$$

$$E_{out} = A \cdot \cos(\omega t + \Delta\varphi_z(V))$$

EXAMPLE 2: GaAs

CUBIC CRYSTAL; SYMMETRY: $\bar{4}3m$

ISOTROPIC CRYSTAL: $n_x = n_y = n_z = n$

Electric field along the diagonal: $E/2\,(0,1,1)$

Electrooptic coefficients:

$\boxed{r_{41}} = r_{52} = r_{63}$ (all other $r_{ij} = 0$)

$$\boxed{\frac{x^2}{n^2} + \frac{y^2}{n^2} + \frac{z^2}{n^2} + \sqrt{2}\, r_{41} xz E + \sqrt{2}\, r_{41} xy E = 1}$$

Transformation into the new main axis coordinate system:

$$\frac{x'^2}{n_{x'}^2} + \frac{y'^2}{n_{y'}^2} + \frac{z'^2}{n_{z'}^2} = 1$$

$$\frac{1}{n_{x'}^2} = \frac{1}{n^2} - r_{41} E \;;\; \frac{1}{n_{y'}^2} = \frac{1}{n^2} + r_{41} E \;;\; \frac{1}{n_{z'}^2} = \frac{1}{n^2}$$

$$\rightarrow \quad \boxed{\begin{aligned} \Delta n_{x'} &= n^3 r_{41} E/2 \\ \Delta n_{y'} &= -n^3 r_{41} E/2 \\ \Delta n_{z'} &= 0 \end{aligned}}$$

} Electrooptic induced birefringence

ELECTROOPTIC INTENSITY MODULATOR

BY POLARIZATION ROTATION

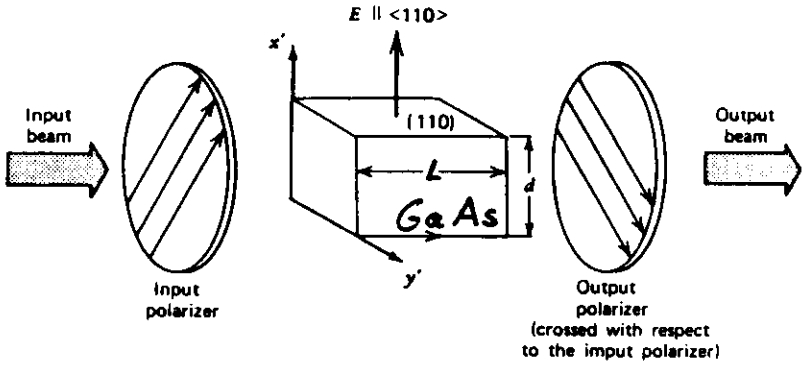

In cubic crystals the electrooptic effect induces BIREFRINGENCE.

$$n_{x'} = n + n^3 r_{41} E/2$$

$$n_{y'} = n - n^3 r_{41} E/2$$

POLARIZATION ROTATION IN BIREFRINGENT MEDIA

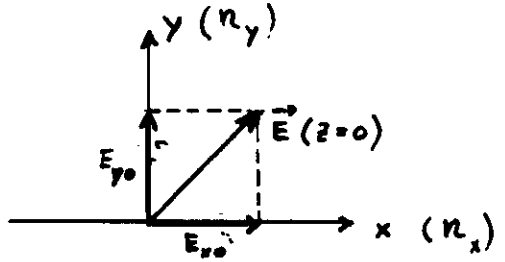

At $z=0$: $\vec{E} = \begin{pmatrix} E_{xo} \\ E_{yo} \end{pmatrix}$

At $z=L$: $\vec{E} = \begin{pmatrix} E_{xo} \cdot \cos(k_o n_x L) \\ E_{yo} \cdot \cos(k_o n_y L) \end{pmatrix}$

$$\vec{E} = \begin{pmatrix} E_{xo} \\ E_{yo} \cdot \cos\left(k_o (n_x - n_y) L\right) \end{pmatrix}$$

At $z = L_\pi$: $\vec{E} = \begin{pmatrix} E_{xo} \\ -E_{yo} \end{pmatrix}$ $\quad k_o (n_x - n_y) L_\pi \stackrel{!}{=} \pi$

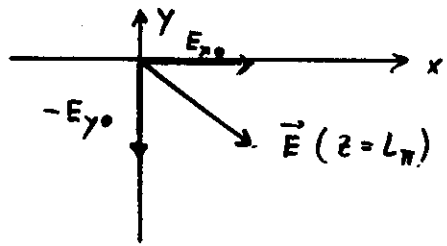

ELECTROOPTIC INTENSITY MODULATOR

Condition for maximum transmission at polarization rotation by 90°:

$$\Delta\varphi_{xy} = \varphi_x - \varphi_y = k_0 (n_x - n_y) \cdot L \doteq \pi$$

Here:

$$k_0 \cdot n^3 r_{41} E_\pi \cdot L \doteq \pi \qquad E_\pi = \frac{V_\pi}{d}$$

$$V_\pi = \frac{d}{L} \frac{\lambda}{2 n^3 r_{41}}$$

Transmission:

$$T = P_{out} / P_{in} = \sin^2 \left(\frac{\pi}{2} \frac{V}{V_\pi} \right)$$

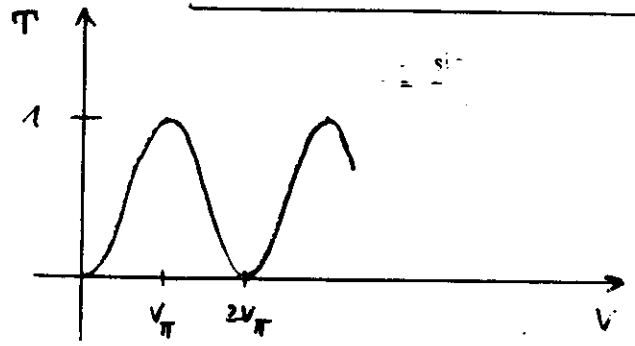

BASIC OPERATING CHARACTERISTICS OF SWITCHES AND MODULATORS

MODULATOR

- INSERTION LOSS

  Loss [dB] = $10 \log \left(P_{out}^{max} / P_{in} \right)^{opt.}$

- MODULATION DEPTH / EXTINCTION RATIO

  Ext. Ratio [dB] = $10 \log \left[\frac{P_{min}(V_1)}{P_{max}(V_2)} \right]^{opt.}$

  ~ −20 dB

- MODULATION VOLTAGE (ON/OFF)

  $V_{ON/OFF} = V_2 (P_{max}) - V_1 (P_{min})$

  $V_{ON/OFF} = V_\pi$ in interferom. modulators

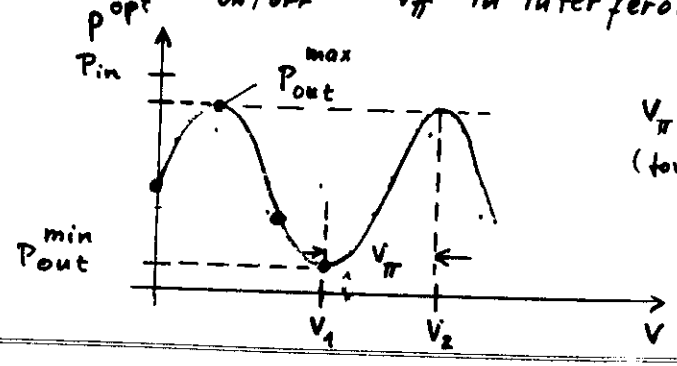

V_π = 300V – 1kV
(for bulk mod.)

BANDWIDTH

RC - LIMITED

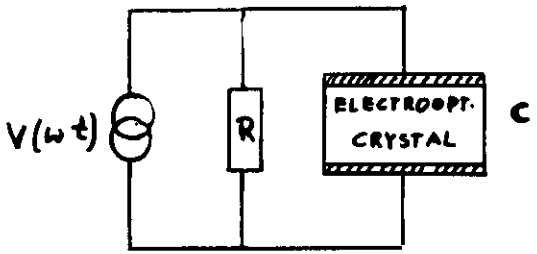

For broad bandwidth:

$R_{termination} = 50\Omega$

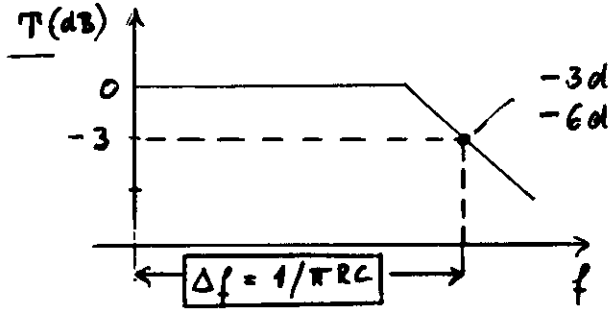

-3dB (optical)
-6dB (electrical)

Δf_{typ}: 1GHz

$$T[dB] = 10 \log \left[P_{out}/P_{in}\right]^{opt} = 10 \log \left[U_2/U_1\right]^{DIODE}$$

$$\Rightarrow \; [dB]^{opt}$$

$$T'[dB]' = 10 \log \left[P_{out}/P_{in}\right]^{el} = 20 \log \left[U_2/U_1\right]^{DIODE}$$

$$\Rightarrow \; [dB]^{el}$$

TRANSIT-TIME LIMITATION IN A LUMPED MODULATOR

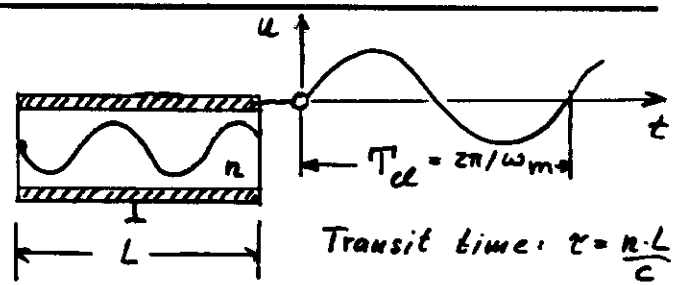

Transit time: $\tau = \frac{n \cdot L}{c}$

For $\tau = T_{el}$ $(\omega_m \cdot \tau = 2\pi)$

there is <u>no modulation</u>

$$(f_m)_{max} = c/2Ln$$

KDP:
n = 1,5
L = 2cm
→ f_{max} = 5GHz

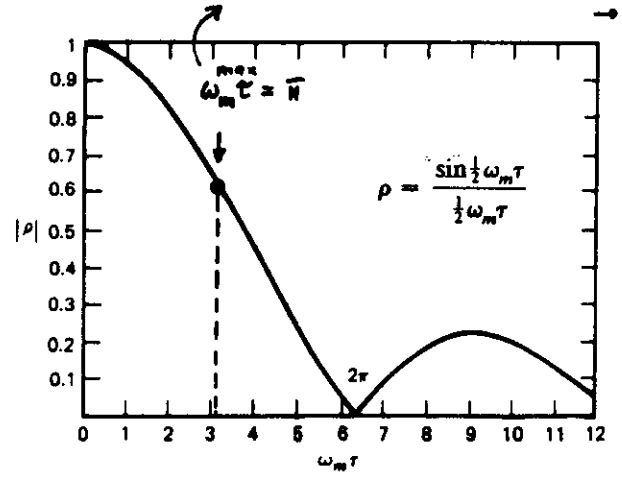

TRAVELING-WAVE MODULATOR

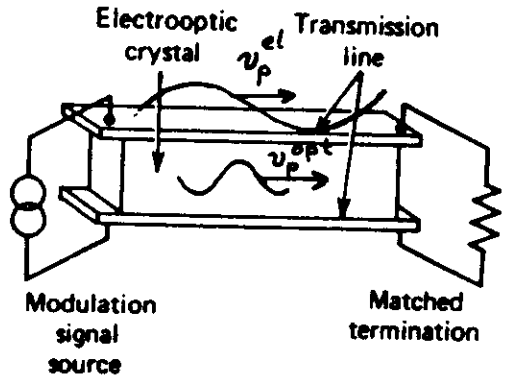

- No transit time limitation for phase-velocity matching

$$v_p^{el} = v_p^{opt} \Rightarrow \Delta f \to \infty$$

For phase-velocity mismatch

$$\boxed{(f_m)^{max} = c / 2L(n - n_m)}$$

n_m: index of refraction at modulation frequency

typical $f_m^{max} \approx 5\ GHz \cdot cm$

BASIC OPERATING CHARACTERISTICS OF SWITCHES AND MODULATORS

SWITCHES

- CROSSTALK

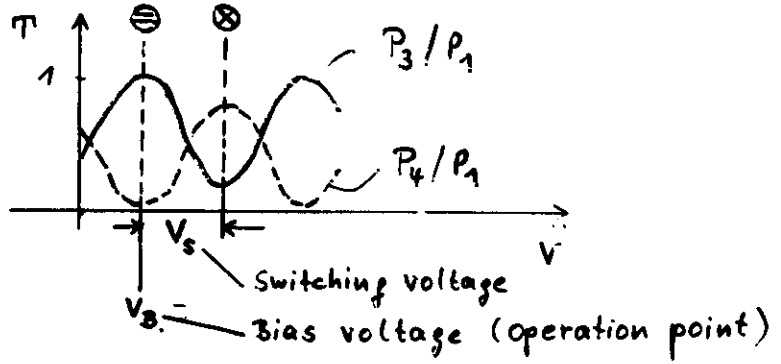

Crosstalk for the bar-state:

$$C_{\ominus} = 10 \log \left[P_4 / P_3 \ (V_B) \right]$$

Crosstalk for the cross-state:

$$C_{\otimes} = 10 \log \left[P_3 / P_4 \ (V_B + V_s) \right]$$

ACOUSTOOPTICS :

INTERACTION OF LIGHT WITH
ACOUSTIC WAVES IN MATERIAL MEDIA

ACOUSTIC WAVE
(periodically modulated density of a medium)
↓
MECHANICAL STRAIN
↓
(Photoelastic effect)
↓
CHANGE IN THE REFRACTIVE INDEX
(periodically modulated)

The traveling refractive index grating is utilized for:

- BRAGG REFLECTION
- DOPPLER FREQUENCY SHIFT

THE PHOTOELASTIC EFFECT

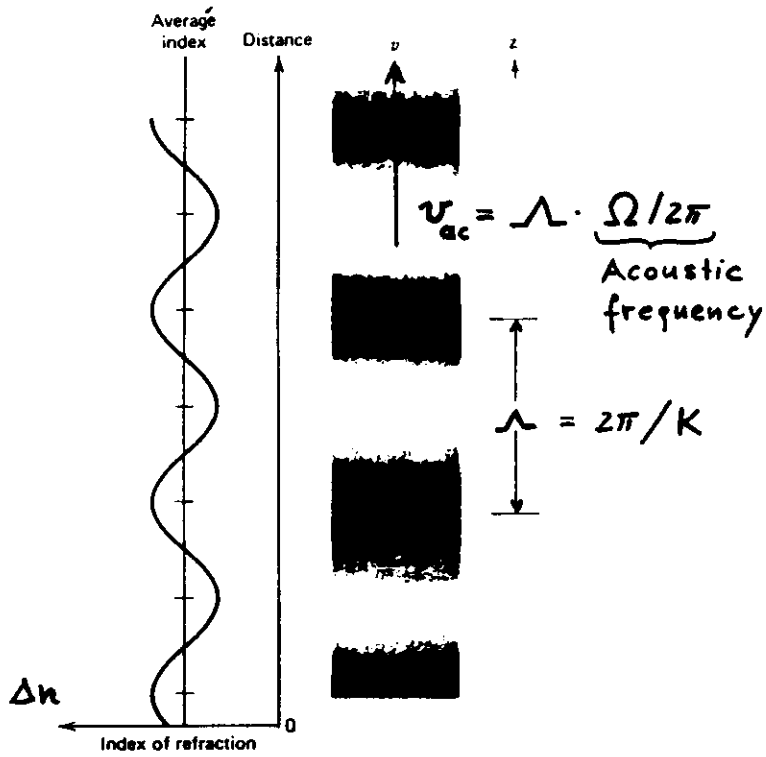

$$\Delta\eta_{ij} = \Delta\left(\frac{1}{n^2}\right)_{ij} = \sum_{kl} p_{ijkl}\, S_{kl}$$

S_{kl} : Strain tensor

p_{ijkl} : Strain-optic tensor $(\sim \chi^{(3)})$

BRAGG REFLECTION

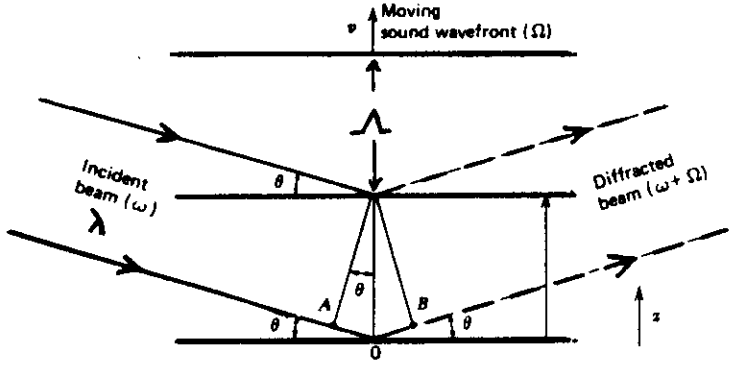

Constructive interference for:

Optical path A-O-B = λ or $m \cdot \lambda$

$$2 \cdot \Lambda \cdot \sin\vartheta \cdot n = \lambda$$

⇒ BRAGG CONDITION:

$$\boxed{\sin\vartheta_B = \lambda / 2\Lambda n}$$

ACOUSTOOPTIC LIGHT MODULATOR

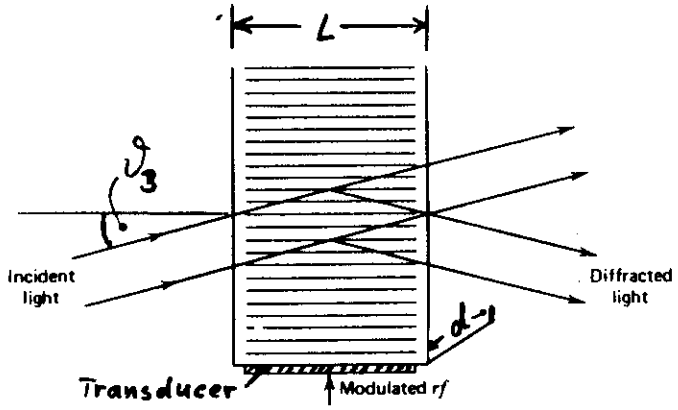

- DIFFRACTION EFFICIENCY: $\eta = \dfrac{P_{diff.}}{P_{inc.}}$

$$\boxed{\eta = \frac{\pi^2}{2\lambda^2 \cos^2\vartheta_3} \left(\frac{L}{h}\right) M P_{ac.}}$$

$M = n^6 p^2 / \rho v^3$: Diffr. Figure of Merit

$\eta_{typ.} \approx 50\%$ for $P_{ac} = 0.5 - 1$ Watt

- BANDWIDTH: Δf_m is limited by beam dir.

$$\boxed{\Delta f_m / f_0 \simeq 1/2}$$ f_0^{typ}: 80 MHz

DOPPLER FREQUENCY SHIFT

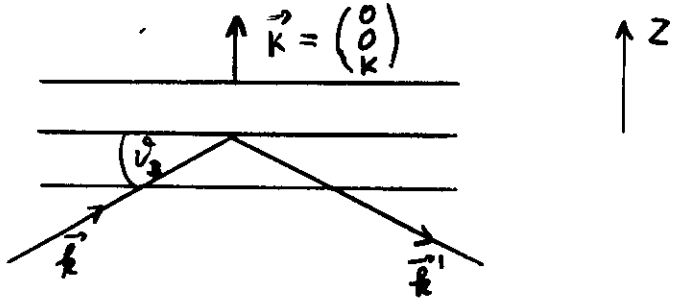

Collision of photons and phonons:

- Conservation of momentum

$$\vec{k}' = \vec{k} + \vec{K} \rightarrow \underbrace{2k \sin\vartheta_B = K}_{\text{(Bragg Condition)}}$$

- Conservation of energy

$$\omega' = \omega - \Omega$$

$$\boxed{\Delta\omega = \Omega = \frac{2\pi v}{\lambda}}$$

Doppler Frequency Shift

THERMOOPTIC EFFECT

Change of the density of a medium and therefore change of the refractive index of a medium by HEAT.

- $\chi^{(3)}$ - Effect (e.g. in glass)
- slow response (ms)

EFFECTS IN SEMICONDUCTORS FOR MODULATION AND SWITCHING

$$\bar{n} = n - i\varkappa$$

n and $\varkappa$ are related by the Kramers-Kronig-R

MODULATION and SWITCHING requires a CHANGE OF $\bar{n}$

- Change of n
  - Electrooptic effect
  - Electrorefraction
- Change of $\varkappa$
  - Electroabsorption
  - Quantum confined Stark effect
  - Carrier injection

ELECTROABSORPTION:

The change of the fundamental absorption ($\alpha = \varkappa \cdot 4\pi/\lambda$) of a semiconductor under applied electric fields.
(FRANZ - KELDYSH - EFFECT)

- Under electrical fields the electron in the valence band has a probability to get into the conduction band by tuneling ($\sim E$)
- Absorption of photons enhances tuneling by reducing the energy barrier $d \to d'$

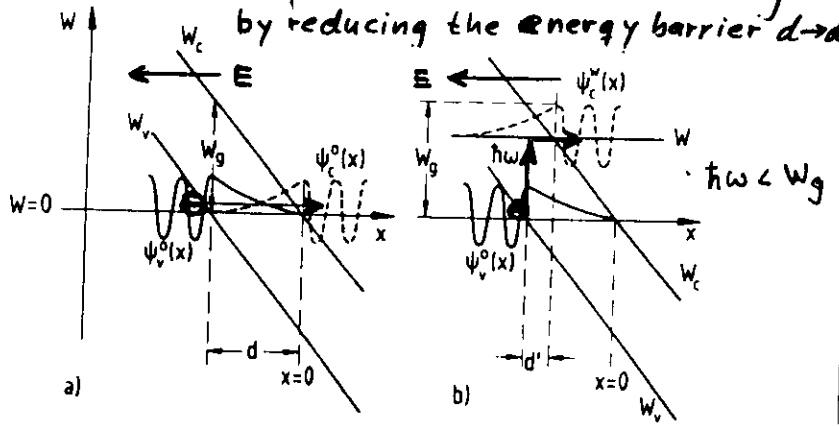

$$d = W_g/(qE) \longrightarrow d' = (W_g - \hbar\omega)/(qE) = f(E)$$

!

by photon absorption

ELECTROREFRACTION

Change of the refractive index Δn by the change of the electrabsorption $\Delta\alpha$ via the Kramers-Kronig-Relation.

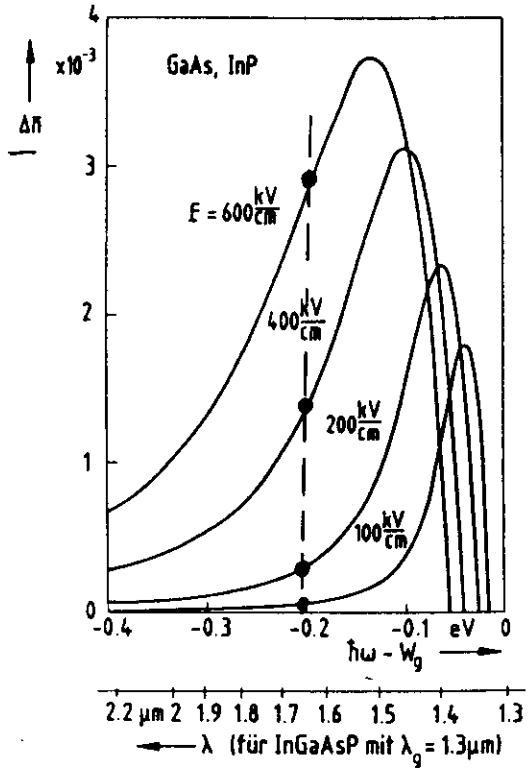

$\Delta n \sim E^2$
($\chi^{(3)}$-effect)

CARRIER INJECTION

Change of the refractive index and of the absorption by FREE CARRIERS (PLASMA EFFECT)

$$\Delta n = -\frac{\lambda^2 q^2 \Delta n^{\text{free carriers}}}{8\pi^2 \varepsilon_0 c^2 n m_e}$$

$$\Delta\alpha = \frac{\lambda^2 q^2 \Delta n^{fc}}{4\pi^2 \varepsilon_0 c^3 n \tau_{in} m_e}$$

- For short length (~ 100 µm) $\Delta\alpha$ may be neglected.
- Δn by the plasma effect is used for phase changes in Integrated Optic devices.

OPTICAL CONTROL

Control of absorption (transmission) by optical excitation. (BANDFILLING)

$$\alpha = f(n^{fc}) = f(P_{opt})$$

Free carriers are generated by OPTICAL EXCITATION

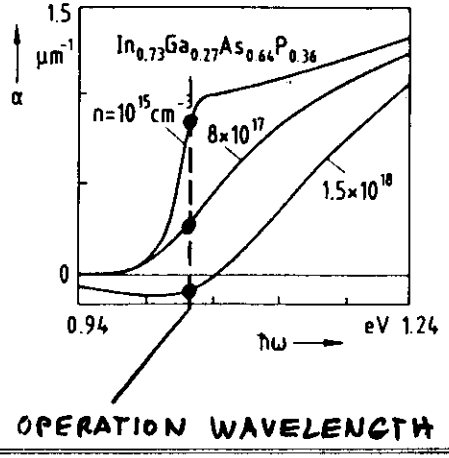

OPERATION WAVELENGTH

Application: OPTICAL BISTABILITY

QUANTUM CONFINED STARK EFFECT

Decrease of the difference of the energy levels between conduction and valence bands in quantum wells under electric fields.

⇒ Shift of the absorption edge to longer wavelengths.

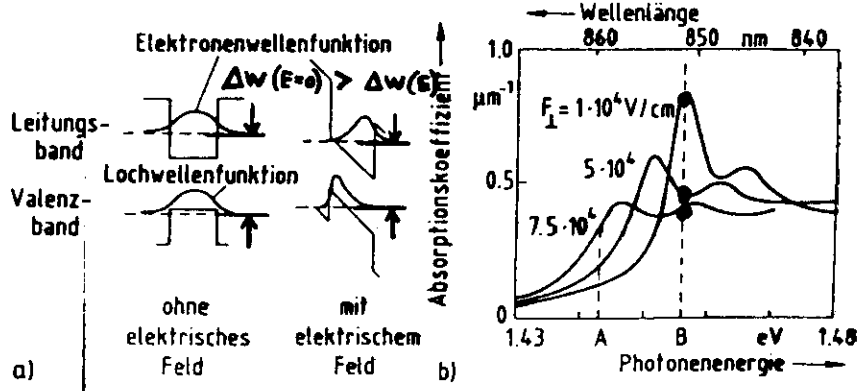

SELF ELECTRO-OPTIC EFFECT DEVICE (SEED)
Optical Bistability

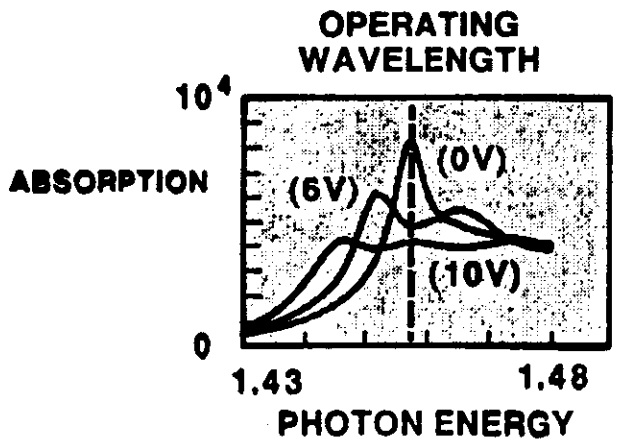

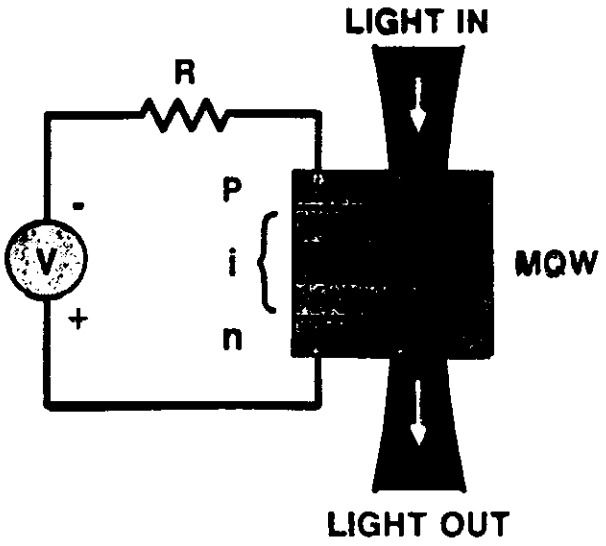

POSITIVE FEEDBACK:

- **INCREASING PHOTOCURRENT GIVES INCREASING ABSORPTION**
- **INCREASING ABSORPTION GIVES INCREASING PHOTOCURRENT**

HGA92565.016

41

GUIDED-WAVE DEVICES FOR MODULATION AND SWITCHING

- BASICS OF GUIDED WAVE OPTICS
- ELECTROOPTIC DEVICES
  - Phase modulator
  - Mach-Zehnder interferometric intensity modulator
  - Directional coupler switch
  - Two-mode-interference switch
  - "Digital" switch
- ACOUSTOOPTIC DEVICE
- THERMOOPTIC DEVICE
- SEMICONDUCTOR DEVICES
- APPLICATIONS
  - External modulation
  - Switch arrays
  - Coherent receiver
  - Fiber rotation sensor

42

GUIDED-WAVE DEVICES FOR MODULATION AND SWITCHING

BASICS OF GUIDED-WAVE OPTICS

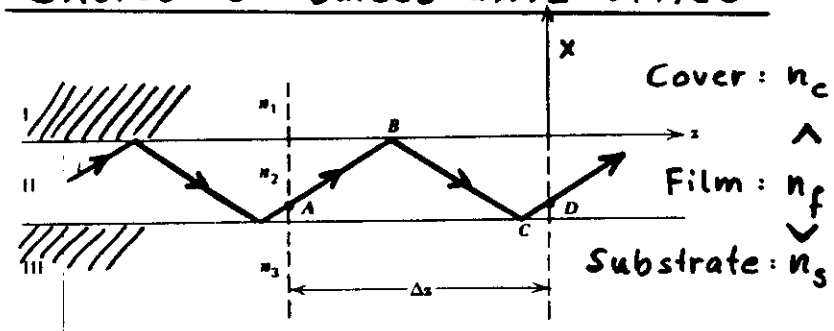

- Operation principle of a Wave guide:

  Total internal reflection at both boundaries and constructive interference after one zick-zack-path.

- PLANAR waveguide · (Film waveguide):
  Guiding in only one dimension
- STRIP or CHANNEL waveguide:
  Guiding in two dimensions

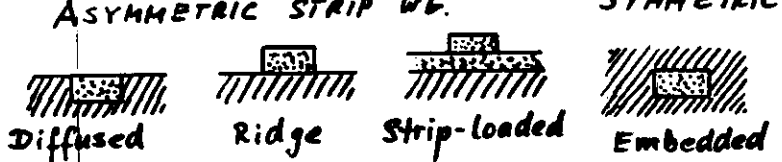

MOTIVATION FOR USING GUIDED-WAVE-OPTICS

- Diffraction free propagation of light at extremly small cross sections over long distances.

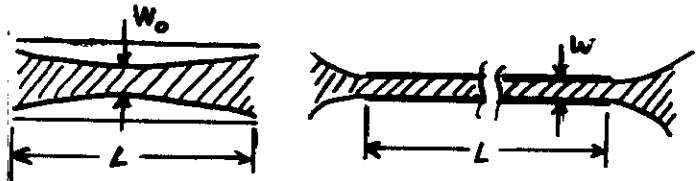

→ Small interaction volume ($\mu m^2 \cdot L$)

→ – Low modulation voltages
– Low electrode capacitance
→ High modulation frequencies

- Realization of complex integrated photonic networks.
- Compatibility to optical fibres (in the case of glass and $LiNbO_3$ substrates)

INTEGRATED OPTICS TECHNOLOGIES

III-V SEMICONDUCTOR (GaAs, InP)

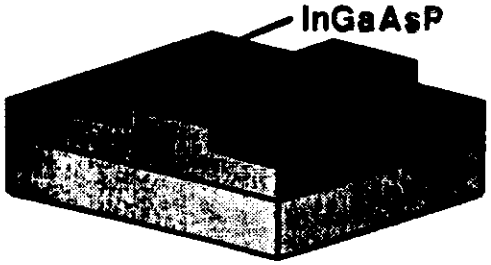

- ELECTRO-ABSORPTIVE AND ELECTRO-OPTIC DEVICES
- MONOLITHIC OPTO AND OPTO-ELECTRONIC INTEGRATION
- VELOCITY-MATCHED MODULATORS
- IMPROVED GROWTH HAS REDUCED LOSSES

HGA71224.022

ELECTRO-OPTIC INSULATORS ($LiNbO_3$)

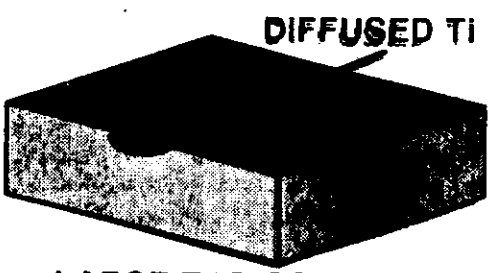

- LARGE E/O COEFFICIENT
- FAMILIY OF DEVICES
- MATURING TECHNOLOGY
- FULLY PACKAGED, LOW LOSS DEVICES
- READY FOR APPLICATION

45

ELECTROOPTIC PHASE MODULATOR

in $LiNbO_3$

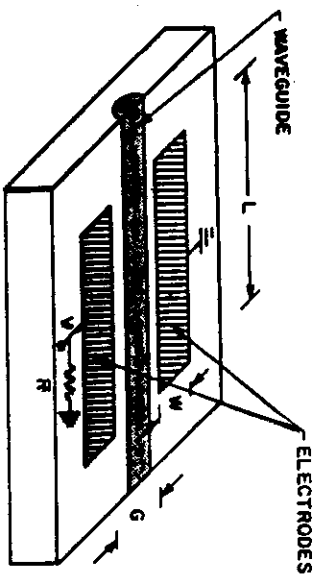

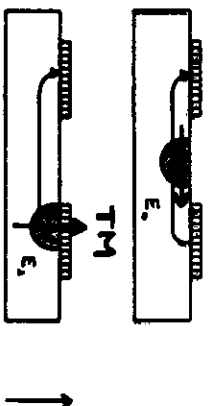

Electrooptically induced index change:

$$\Delta n(V) = -\frac{n_e^3 r_{33}}{2}\,\frac{V}{G}\,\Gamma$$

Γ is the overlap of modulating electric field and optical intensity distribution:

$$\Gamma = \iint E_{ex} \cdot I_{opt}\, dA$$

46

Phase shift over the length L:

$$\Delta\varphi = \Delta\beta \cdot L = k_0 \, \Delta n \, L = -\pi n_e^3 r_{33} \Gamma \frac{V}{G} \cdot \frac{L}{\lambda}$$

Condition for a phase shift of π:

$$V_\pi \cdot L = \frac{\lambda G}{n_e^3 r_{33} \Gamma}$$

VOLTAGE - LENGTH - PRODUCT [Vmm]

Typical values at $\lambda = 1.3\,\mu m$: 70 Vmm

→ $L = 1\,cm$; $V_\pi = 7\,V$

BANDWIDTH

- Depends on the capacitance / length and the ratio electrode gap / width

BANDWIDTH - LENGTH - PRODUCT [GHz cm]

- Lumped type electrode : ~ 2 GHz cm
- Traveling wave electrode : ~ 6 GHz cm
- Periodic phase reversal
  - → Bandpass characteristic

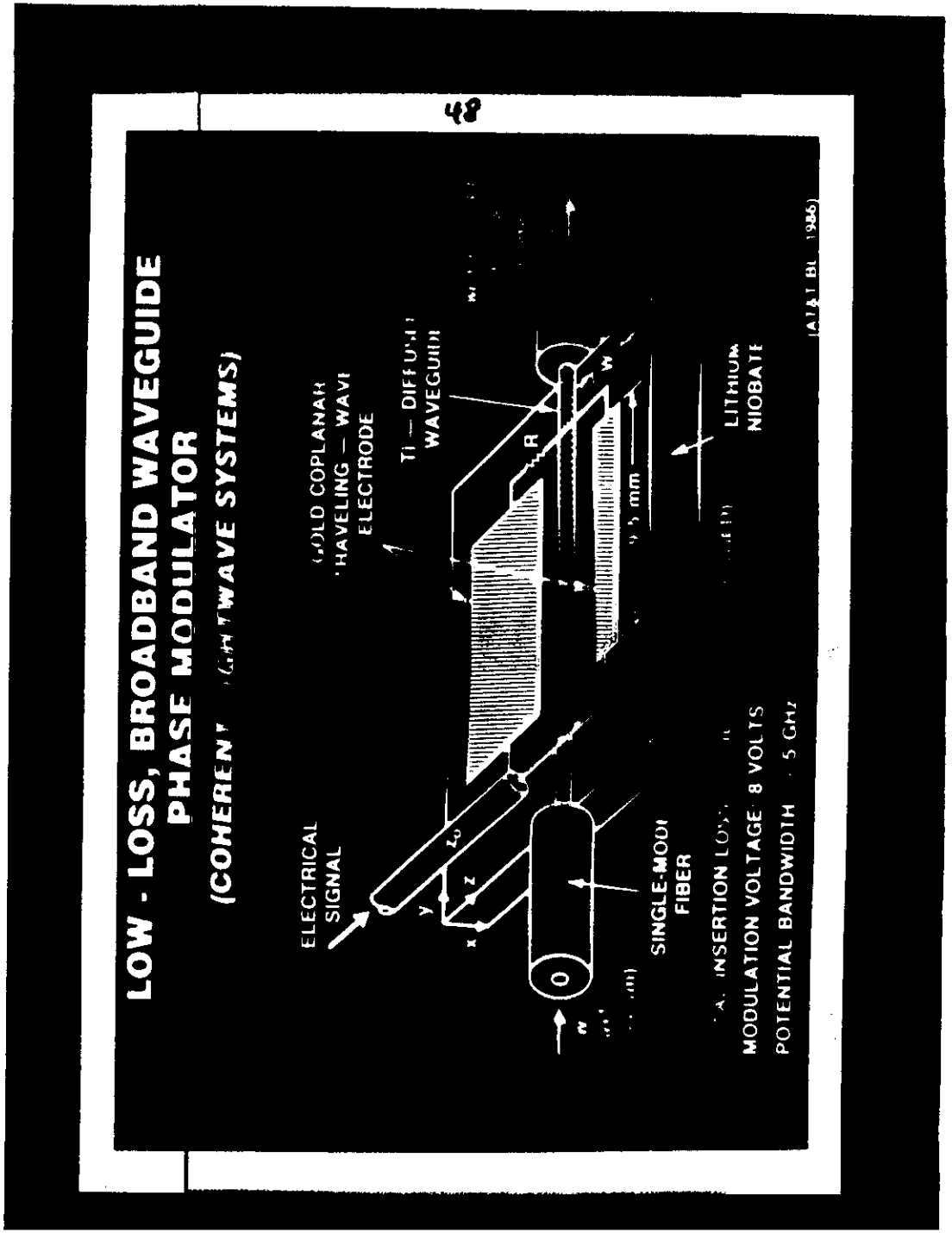

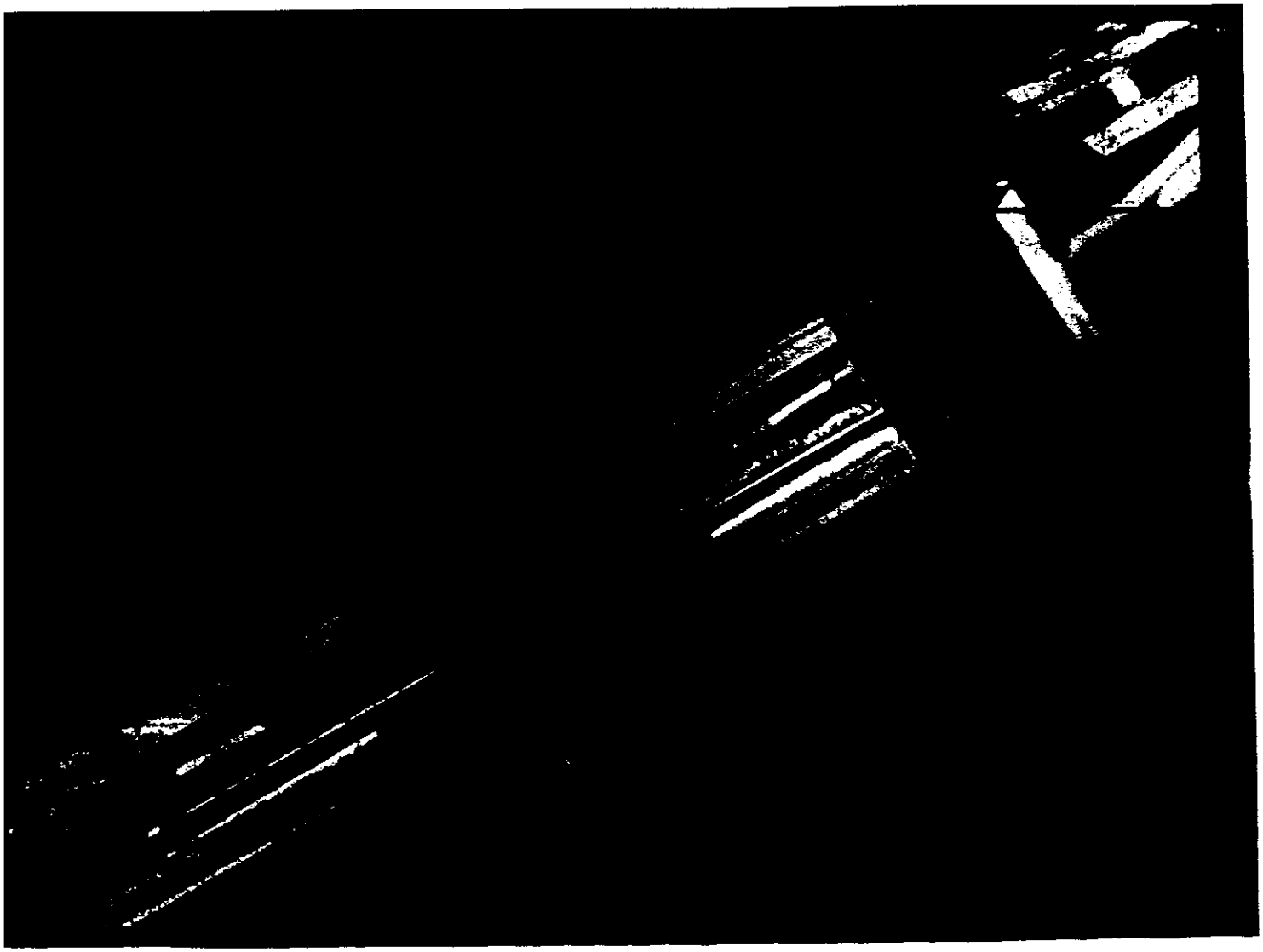

GaAs Traveling-Wave Phase Modulator

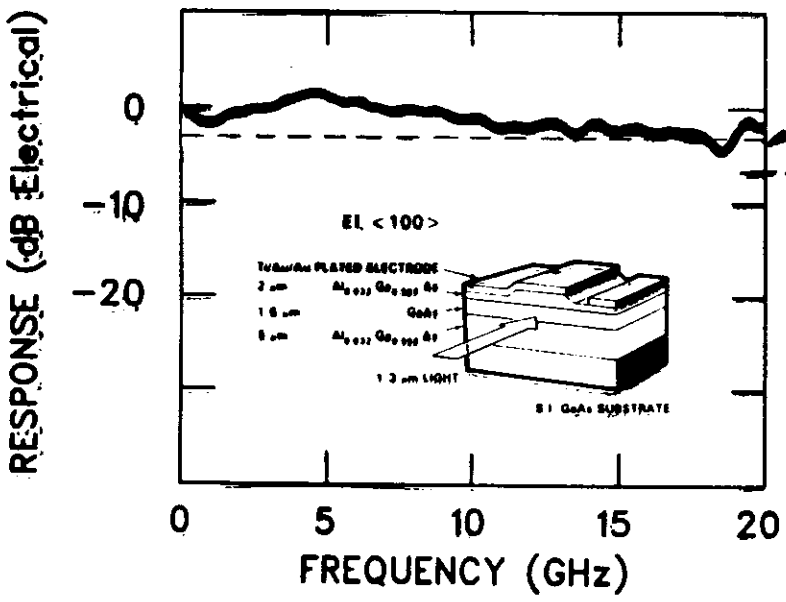

3dB (electrical)

3dB (optical) = 6dB el

Wang, et al., APL 51, 83(1987)

Y-BRANCH INTERFEROMETER

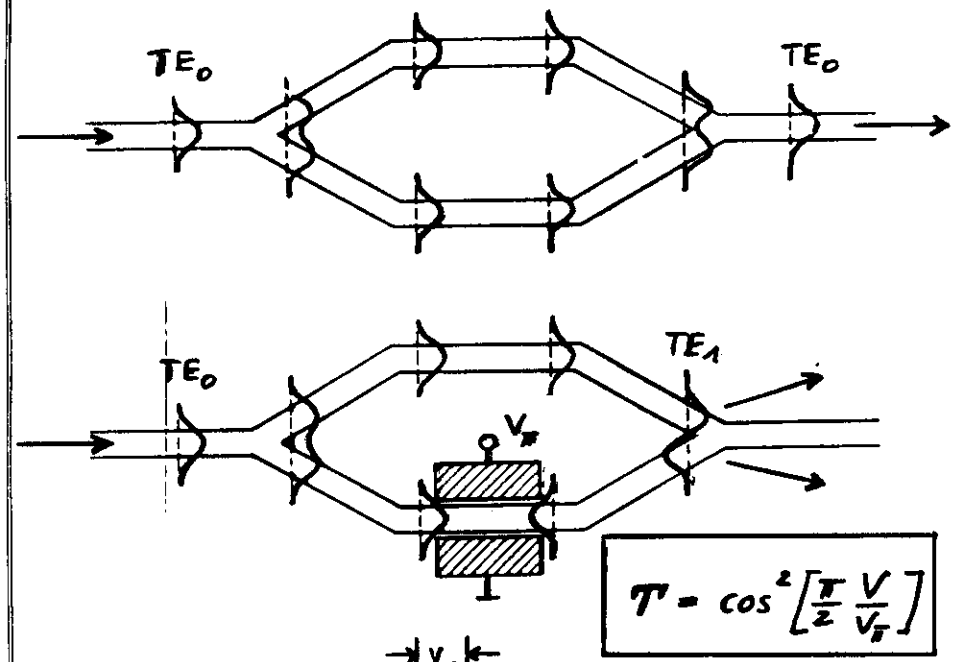

$$T = \cos^2\left[\frac{\pi}{2}\frac{V}{V_\pi}\right]$$

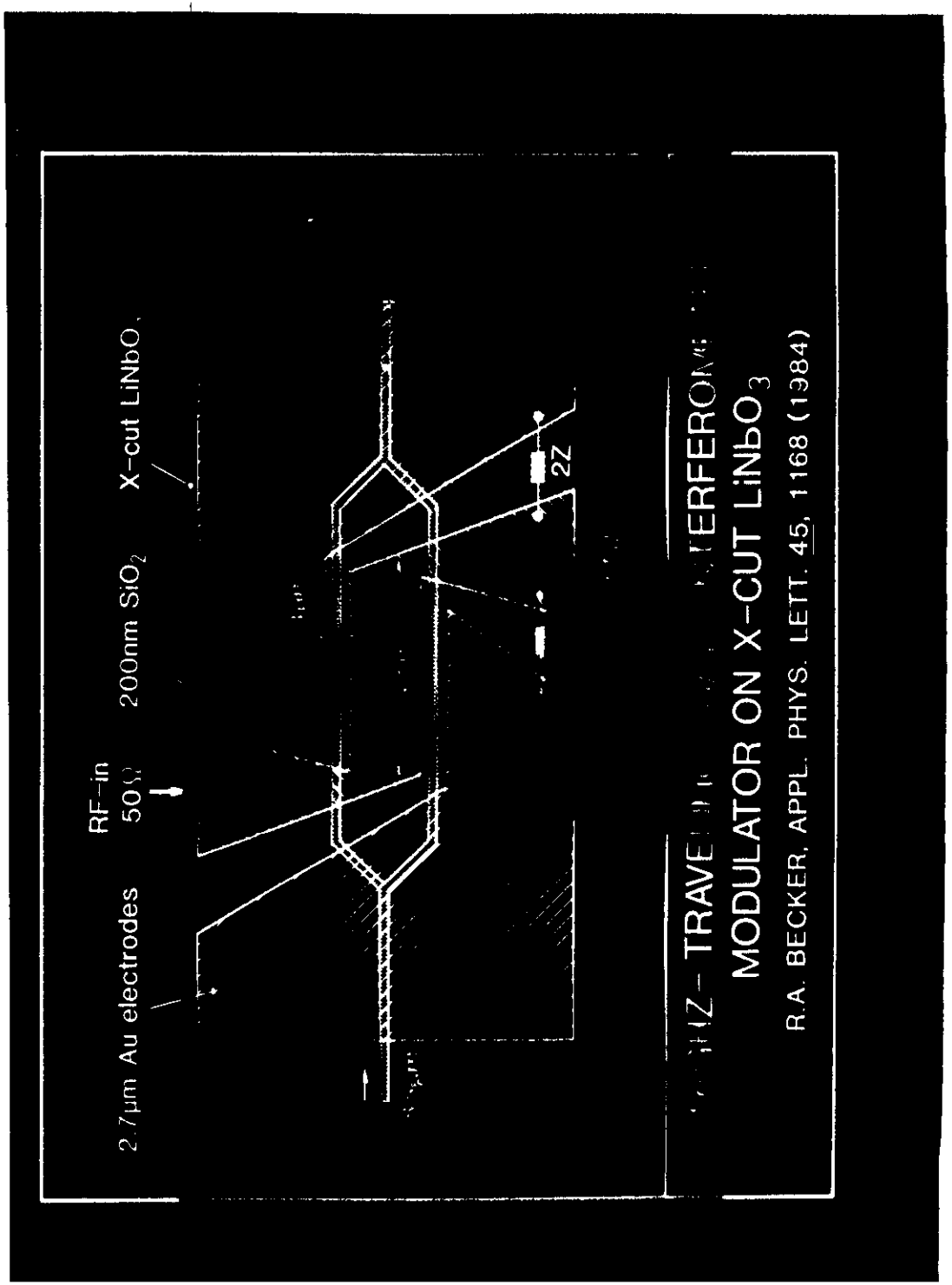

BALANCED-BRIDGE-INTERFEROMETER

2 x 2 Switch

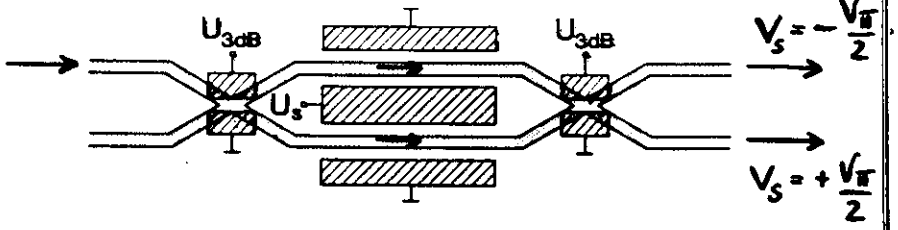

1 x 2 Switch

10 mm

$V_\pi = 7V$

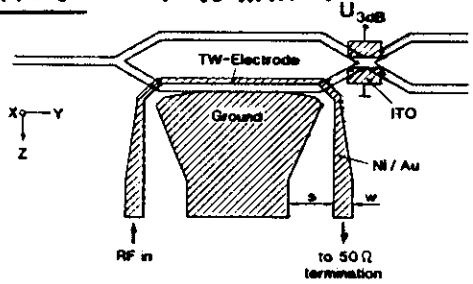

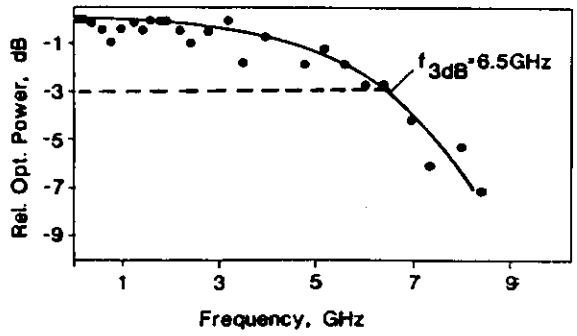

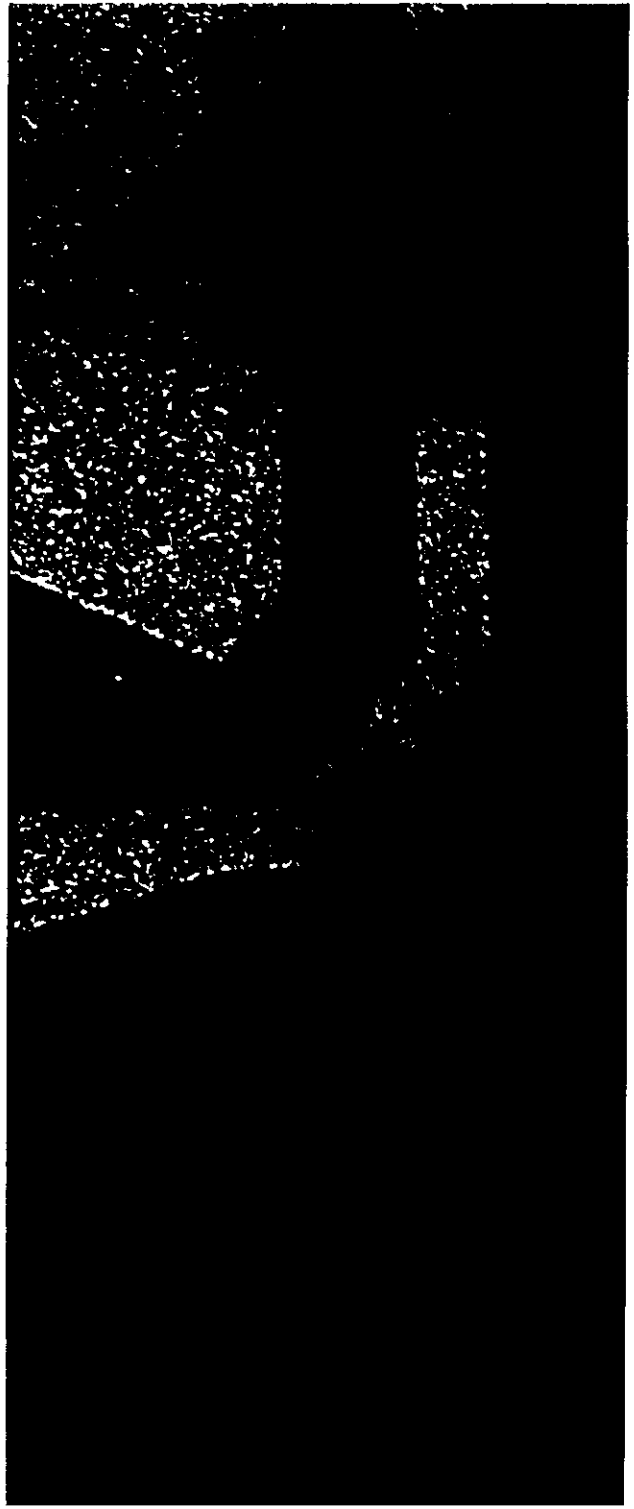

3M

THE DIRECTIONAL COUPLER SWITCH (UNIFORM ELECTRODES)

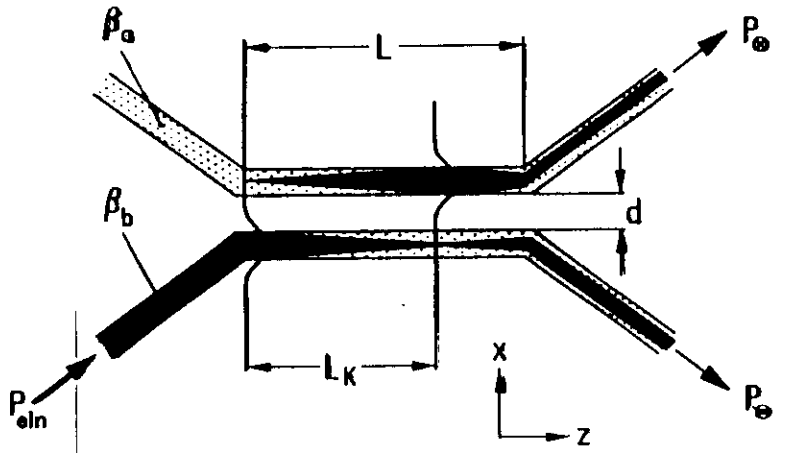

- Identical waveguides ($\beta_a = \beta_b$; $\Delta\beta = 0$)

$$P_\otimes / P_{in} = \sin^2\left[\frac{\pi}{2}\frac{L}{L_K}\right] = \sin^2[\varkappa L]$$

with the coupling length $L_K = \pi/2\varkappa$ and $\varkappa$ the coupling constant

Complete crossover condition:

$$L/L_K = n \qquad n : \text{odd integer}$$

DIRECTIONAL COUPLER SWITCH
UNIFORM ELECTRODES

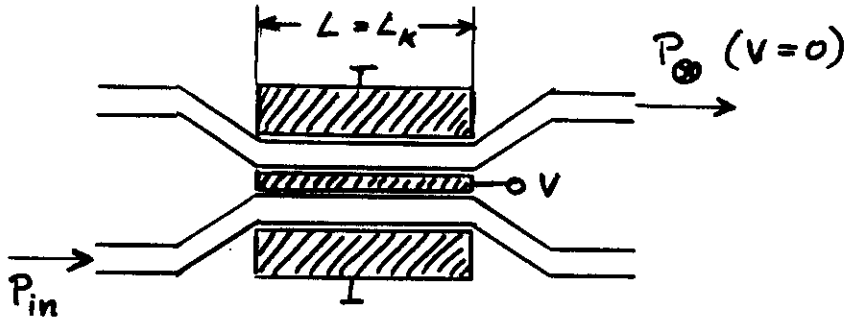

Switching from the cross state to the bar state is possible by detuning the synchroism of the DC.

Transmission (to the ⊗ state) of a DC detuned by $\Delta\beta = k_o \cdot \Delta n\,(V)$

$$P_\otimes / P_{in} = \frac{1}{1 + (\delta/\varkappa)^2} \sin^2\left[\varkappa L \left[1 + (\delta/\varkappa)^2\right]^{1/2}\right]$$

with $\delta = \Delta\beta/2$

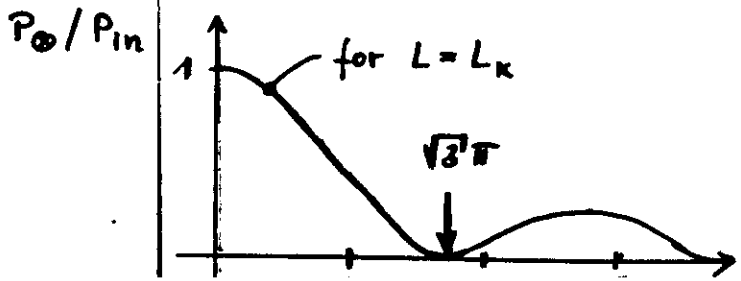

- What happens, if $L > L_K$?

Not all the light will go into the ⊗-state.

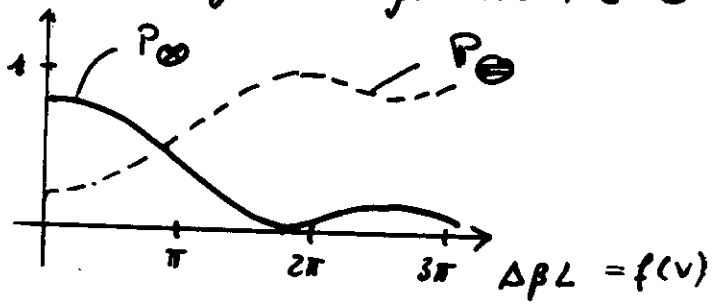

At switching into the ⊗-state there is crosstalk in the ⊖-arm.

By detuning all the light remains in the ⊖-arm.

→ No crosstalk in the ⊗-arm.

- What happens, if $\beta_a \neq \beta_b$; $\Delta\beta \neq 0$?

$P_{\otimes} / P_{in} < 1$

There will be always crosstalk in the ⊖-arm, if the switch is in the ⊗-state.

The ⊖-state is always achievable by detuning.

- How to get a perfect ⊗-state for $L \neq L_K$ and $\beta_a \neq \beta_b$?

THE DIRECTIONAL COUPLER SWITCH ($\Delta\beta$-REVERSAL ELECTRODES)

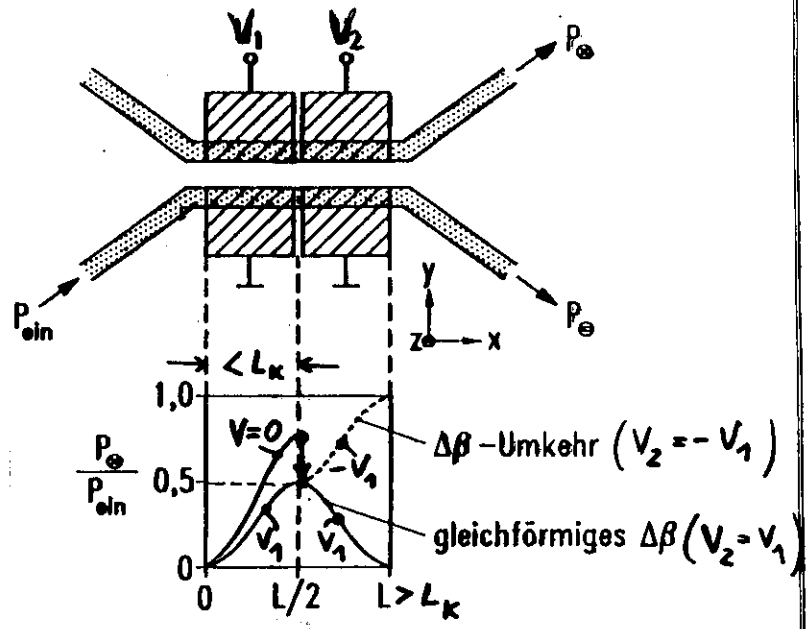

- The ⊖-state is achieved by sufficient and uniform detuning (as usual).
- The ⊗-state is achieved by reversing the sign of the detuning after $L/2$, with $L > L_K$.

TWO-MODE-INTERFERENCE SWITCH

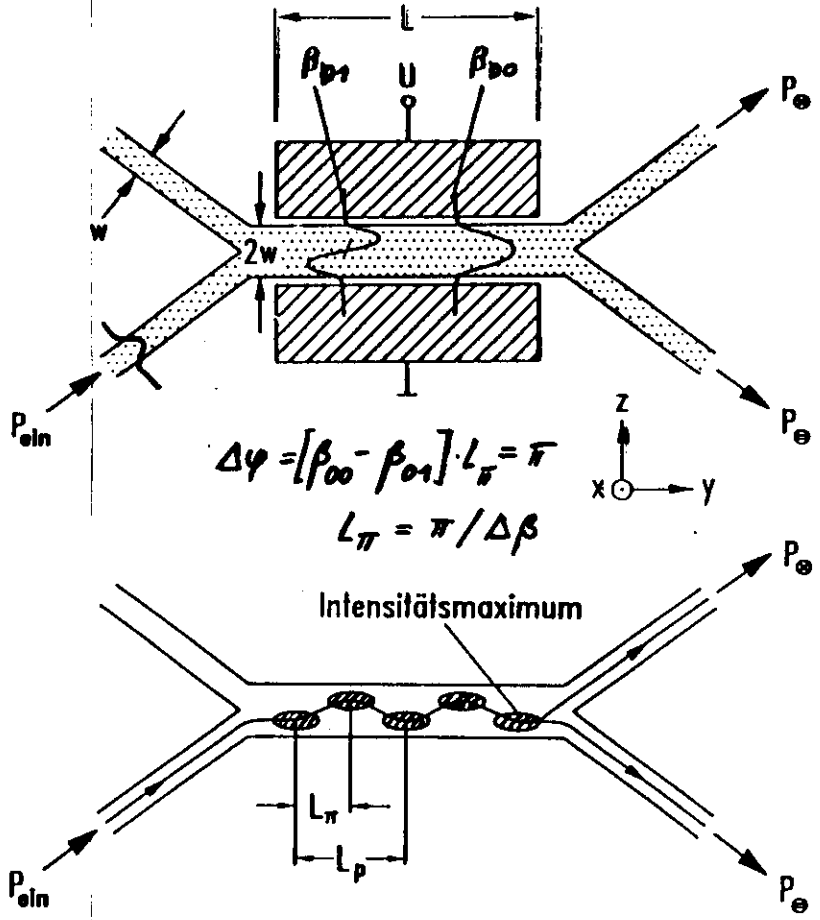

$P_\oplus / P_{in} = \sin^2\left[\frac{\pi}{2}\frac{L}{L_\pi}\right]$; $P_\ominus / P_{in} = \cos^2\left[\frac{\pi}{2}\frac{L}{L_\pi}\right]$

SWITCHING BY CHANGING $L_\pi(V)$

(NOT BY DETUNING)

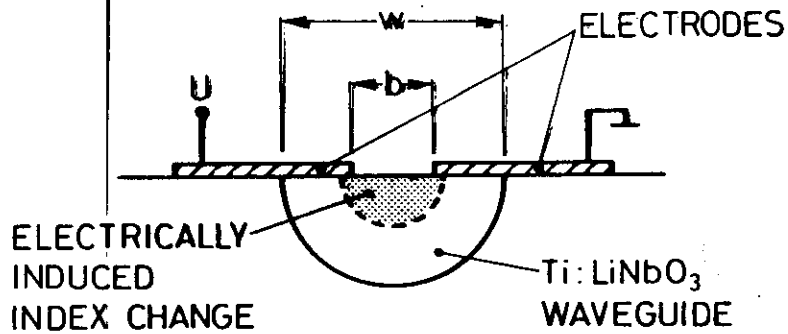

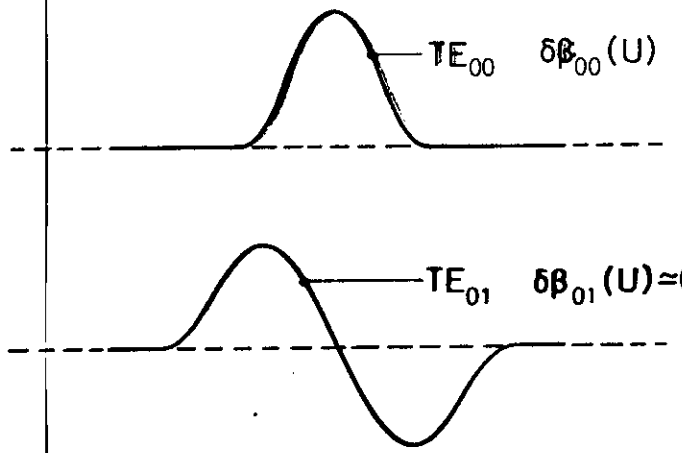

SWITCHING CONDITION: $\delta\beta_{00}(U_\pi) \cdot L = \pi$

$P_\oplus / P_{in} = \sin^2\left[\pi/2\, U/U_\pi\right]$; $P_\ominus / P_{in} = \cos^2\left[\pi/2\, U/U_\pi\right]$

PRINCIPLE OF ELECTROOPTIC SWITCHING

Advantages of THI-devices

- Both switch states can be achieved by a two-electrode structure independently of the L/L_π-ratio.

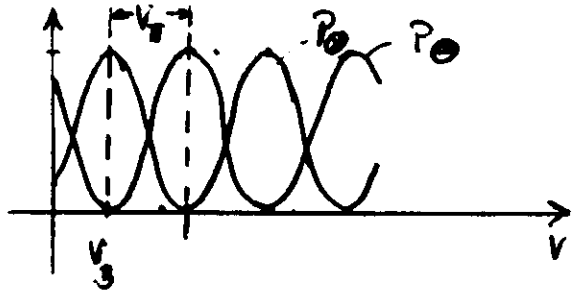

- Low fabrication tolerances with respect to symmetric input and output waveguides. → Low crosstalk

- Simple traveling wave electrode

Disadvantage

- Stronger wavelength dependence
  (However, may be utilized for wavelength multiplexing)

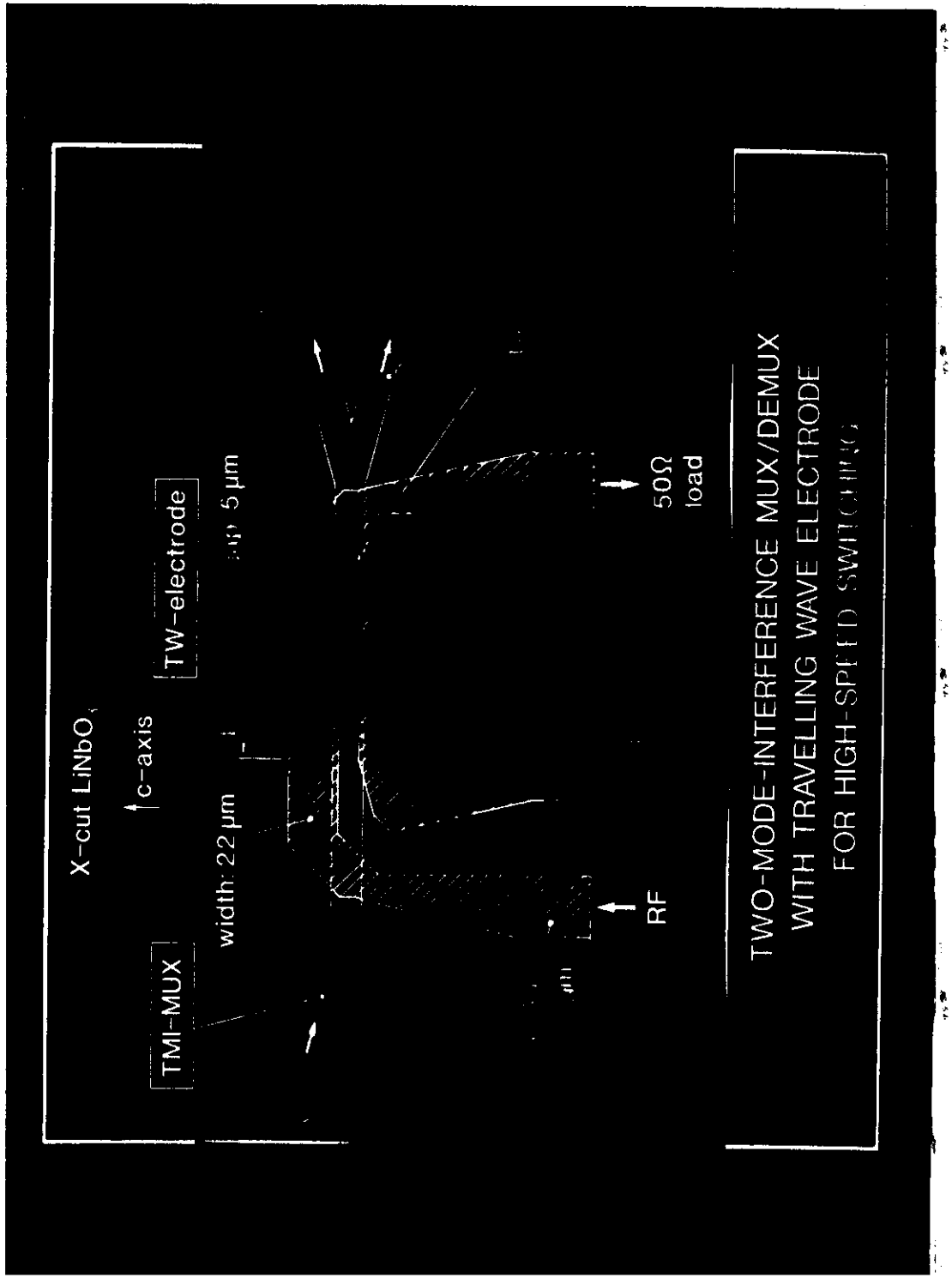

NONINTERFEROMETRIC "DIGITAL" SWITCH

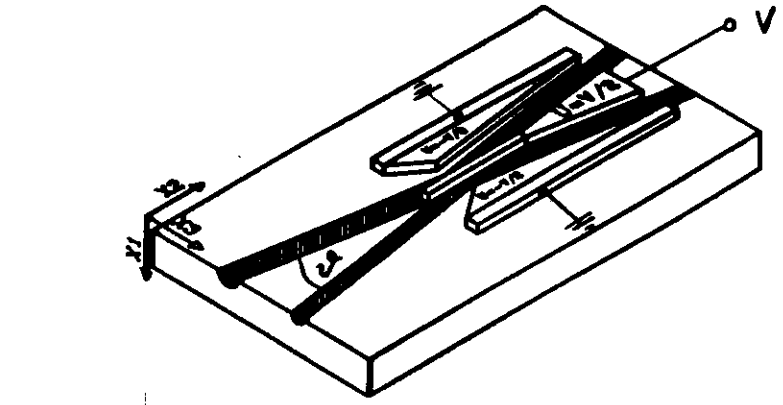

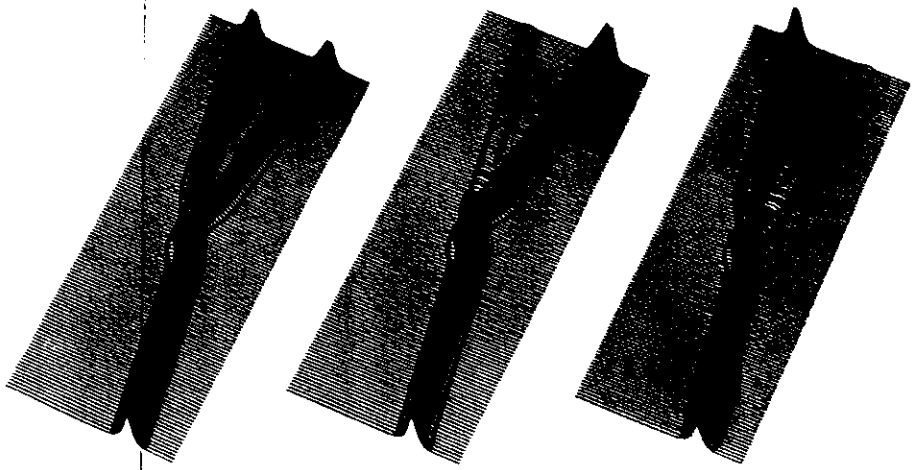

SWITCHING BY BREAKING THE SYMMETRY OF AN ADIABATIC WAVEGUIDE STRUCTURE.

NONINTERFEROMETRIC "DIGITAL" SWITCH

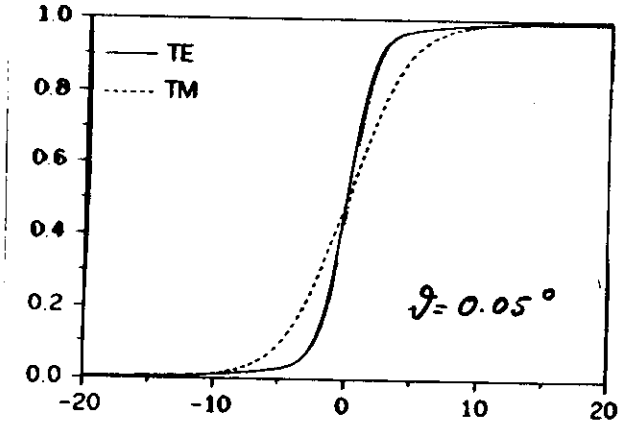

Advantages:

- Polarization independent
- Wavelength independent
- Switching voltage uncritical

Disadvantages:

- High switching voltage (typ. ± 40V)
- Fabrication difficult

SURFACE ACOUSTO-OPTIC BEAM DEFLECTOR

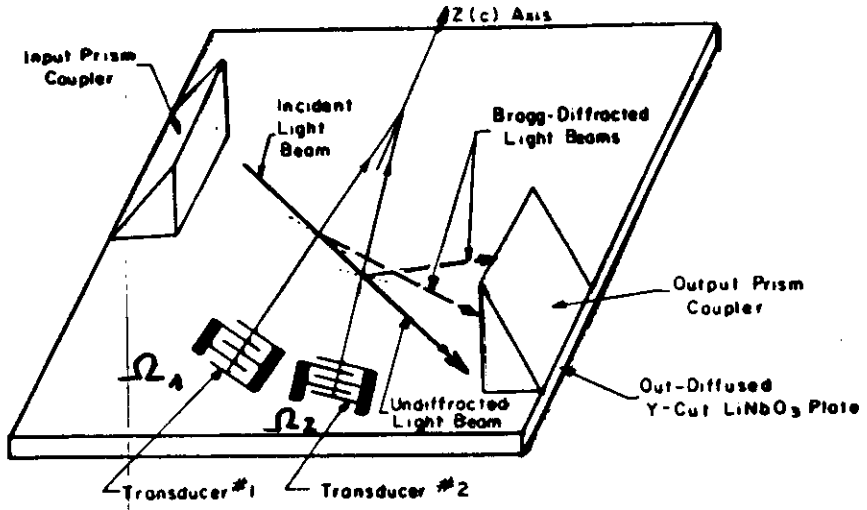

BRAGG CONDITION:

$$\sin \vartheta_3 = \frac{\lambda}{2 \Lambda n} = \frac{\lambda \Omega}{v_{ac} n 4\pi}$$

APPLICATIONS:

- Laser printer
- RF real time spectrum analyzer

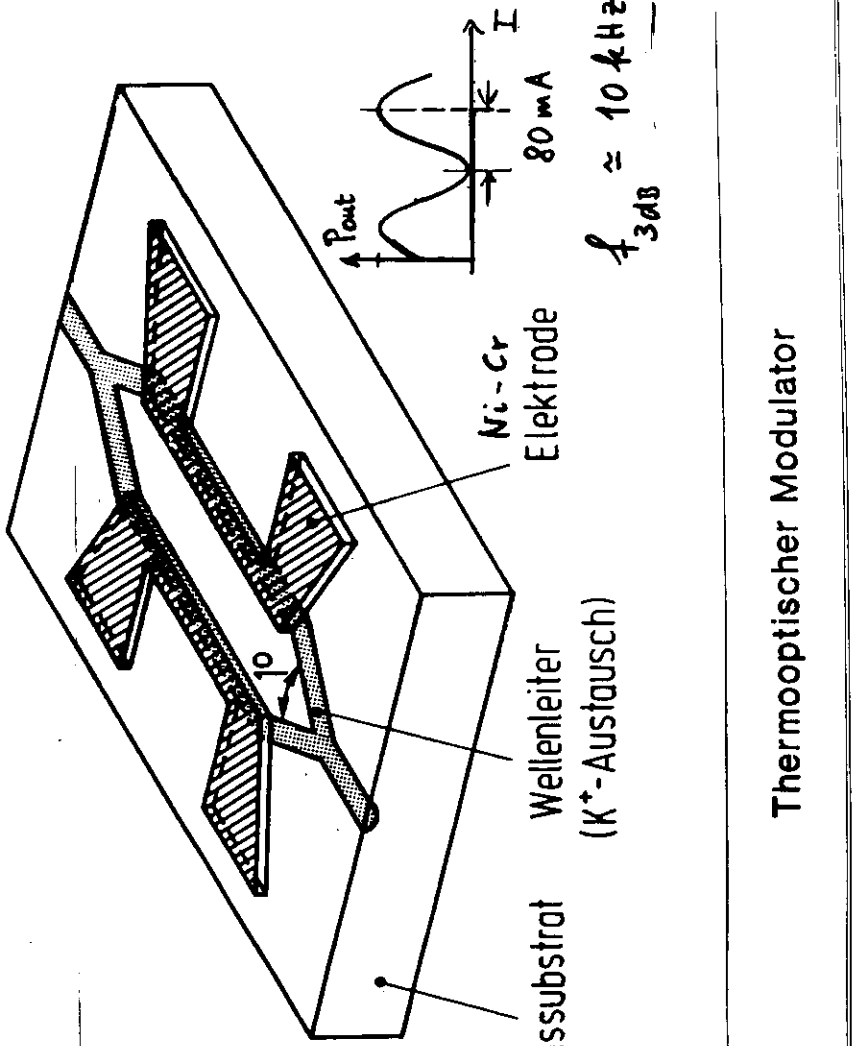

ELECTROABSORPTION MODULATOR

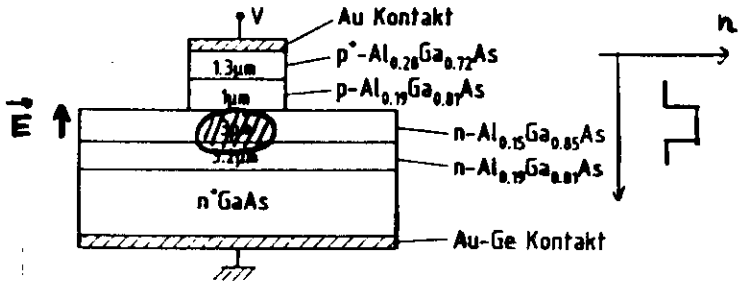

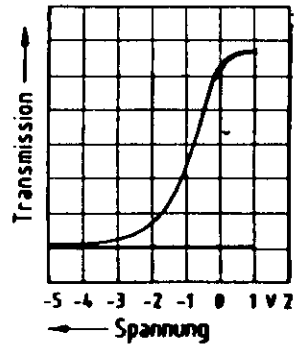

Ebeling

CARRIER INJECTION X-SWITCH

TOTAL INTERNAL REFLECTION (TIR)

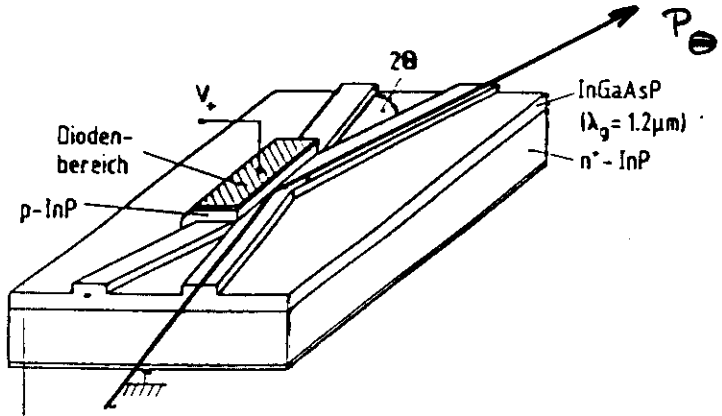

$\Delta N^{el} \sim 10^{18}\,cm^{-3}$

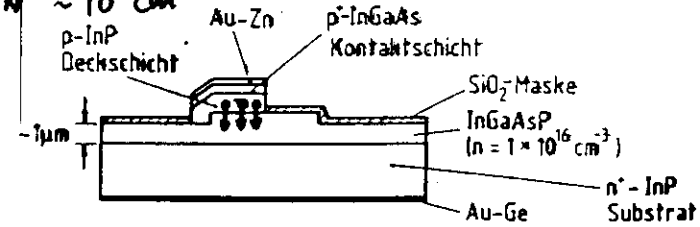

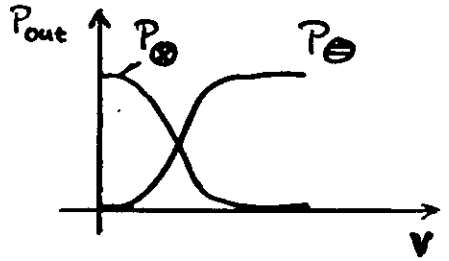

"DIGITAL" SWITCH

Ebeling

TYPICAL LINK
USING EXTERNAL MODULATION

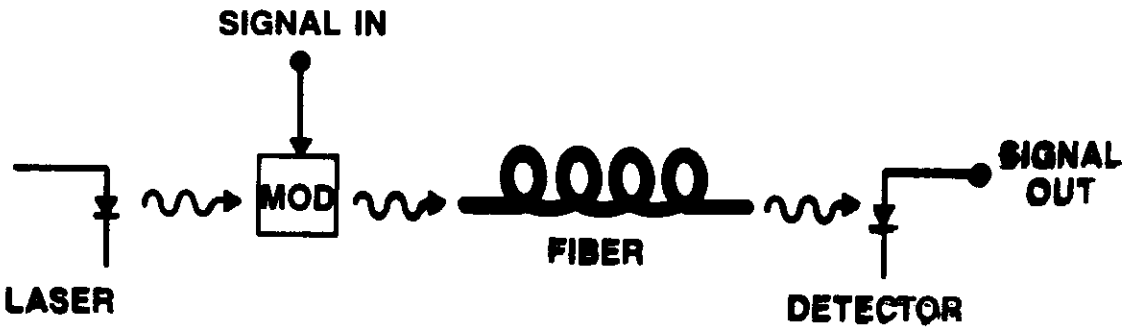

69

HIGH-SPEED EXTERNAL MODULATION

ADVANTAGES:

- MINIMUM SPECTRAL BROADENING
- LARGE EXTINCTION RATIO
- SOURCE FLEXIBILITY
- EXTENDABLE TO SWITCHING

70

Ti:$LiNbO_3$ Intensity Modulator

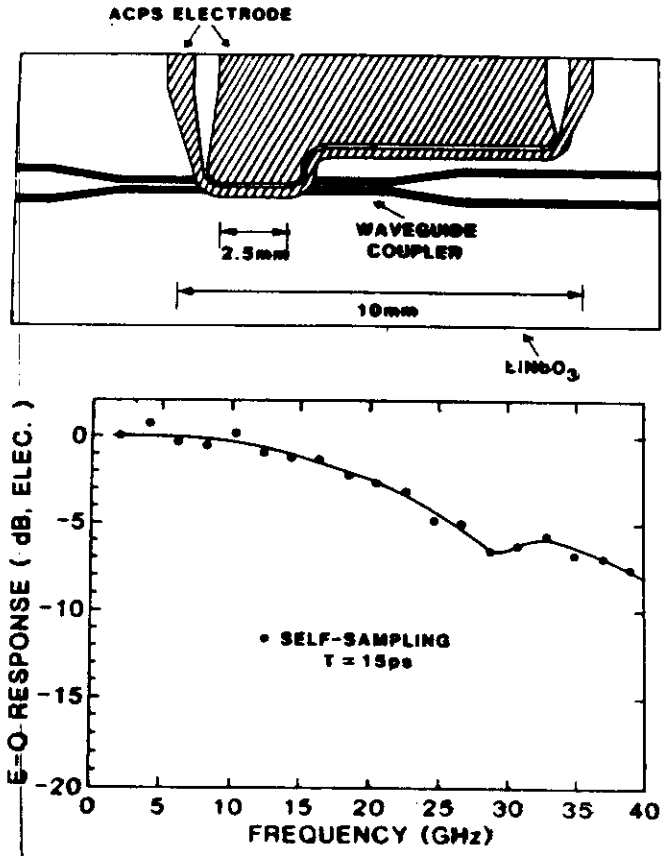

Korotky

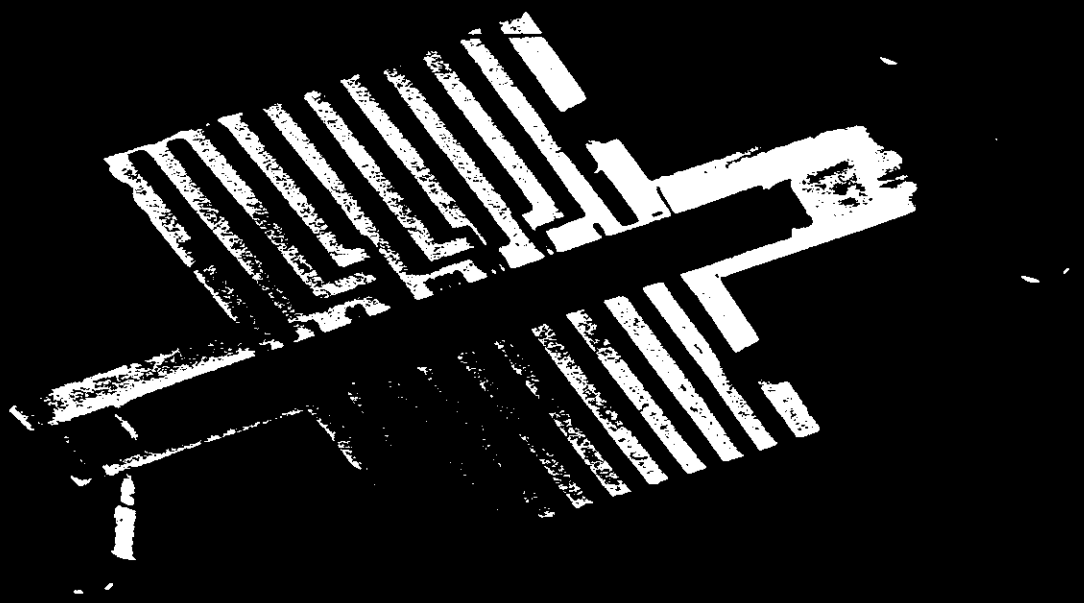

$LiNbO_3$ -SWITCH ARRAYS

	Crossbar	Dilated Benes	Tree
Total No. of Switches	N^2	$2N \log_2(N)$	$2N(N-1)$
N=4	16	8	24
Switches per Path	Max: $2N-1$ Min: 1	$2\log_2(N)$	$2\log_2(N)$
N=4	1-7	4	4
Total Crosstalk	$C_o + 10\log_{10}(N-1)$	$2C_o + 10\log_{10}(2\log_2(N))$	$2C_o + 10\log_{10}(2\log_2(N))$

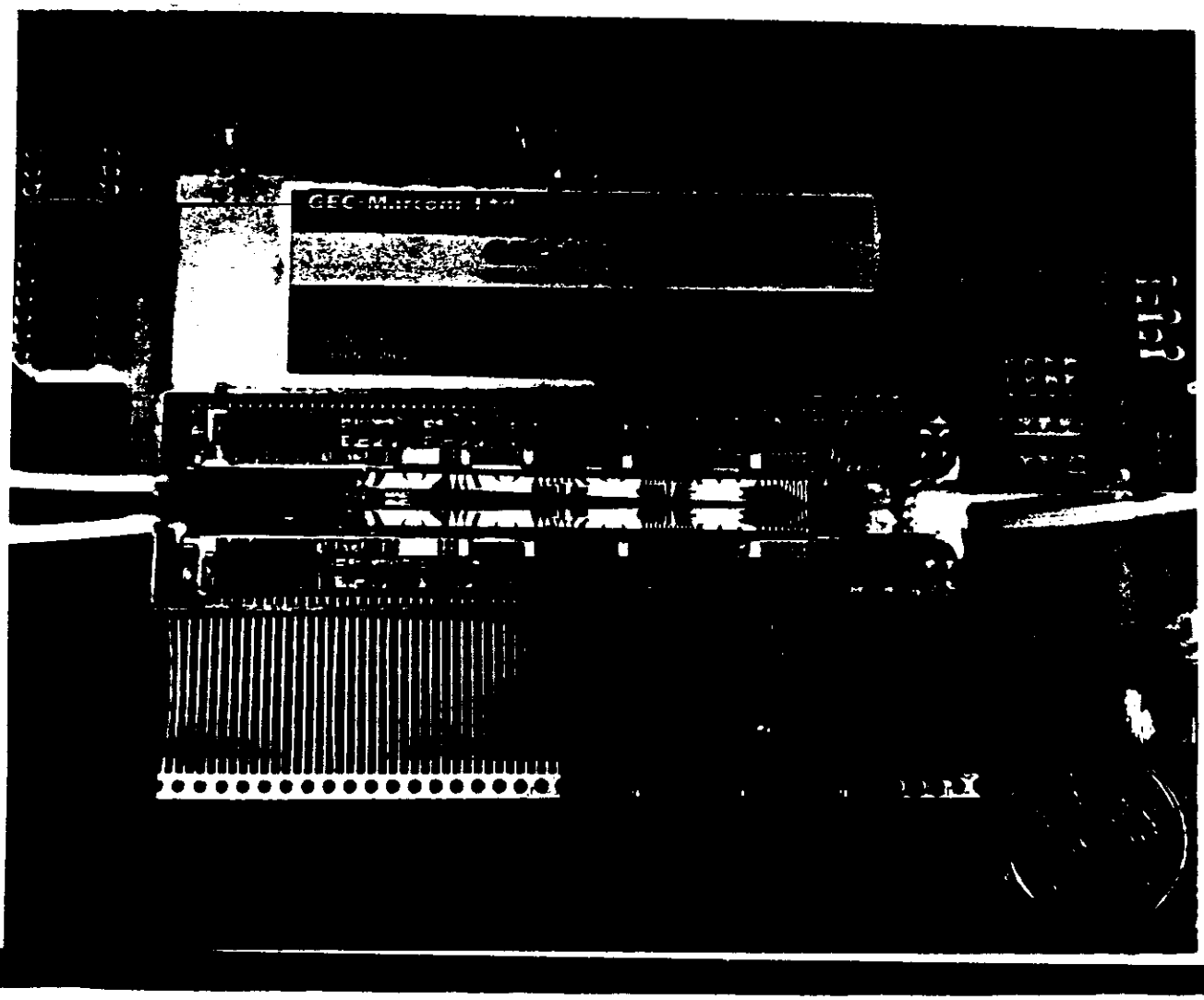

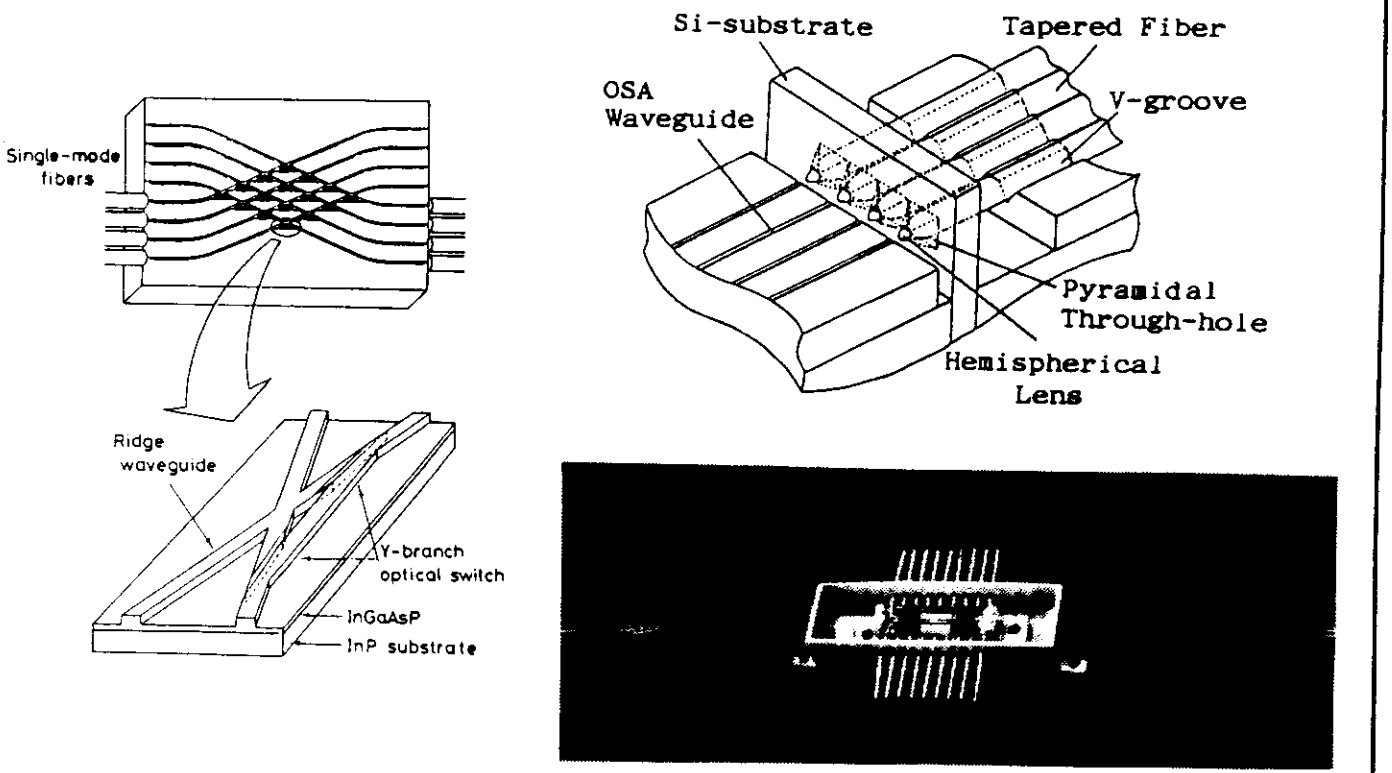

InGaAsP/InP 4x4-SCHALTMATRIX

(IOOC'89, Hitachi)

INTEGRATED-OPTIC COHERENT RECEIVER DEVICE

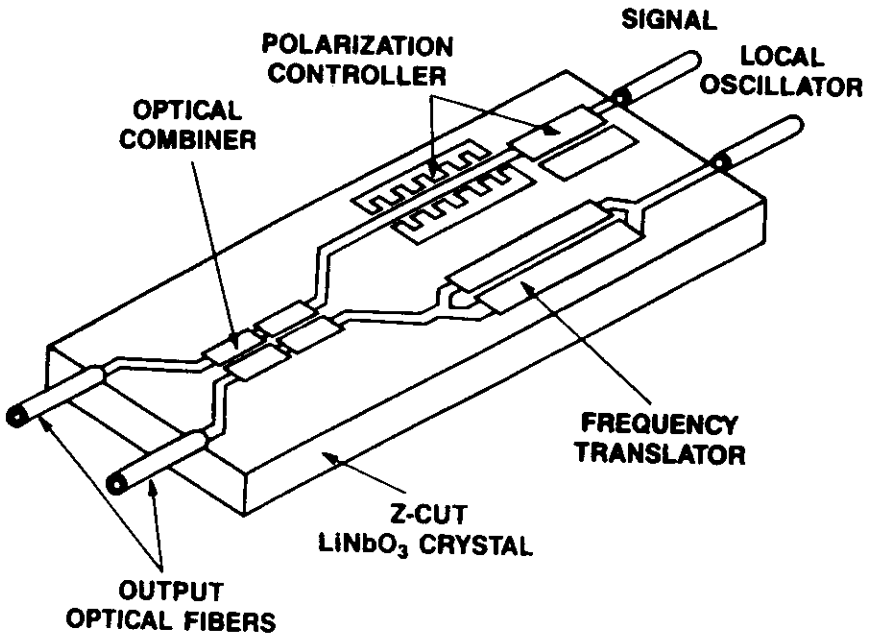

STALLARD, et al.,
EL 21, 1077 (1985)

R35

SEL ALCATEL

Gyro Optic

Defense and Aerospace

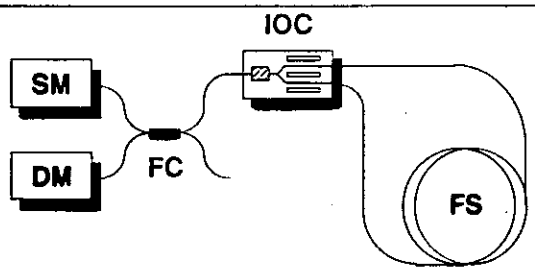

IOC-module ($Ti:LiNbO_3$)

polarizer			SM	:	source module
extinction ratio	:	>50 dB			
Y-junction			DM	:	detector module
splitting ratio	:	1.0 ± 0.2			
phase modulator			FC	:	fiber coupler
$V_{\pi/2}$	:	3 V			
bandwidth	:	1 GHz			
pigtails			FS	:	fiber spool
insertion loss	:	0.5 ...1 dB/interface			
pigtailed IOC					
insertion loss	:	3.5 ...5 dB			

SUMMARY

- Guided-wave-Optics is <u>the</u> technology of choice for optical modulation and switching:
  - Low modulation voltage
  - Broad bandwidth
  - Good coupling efficiency to fibres
  - Integratable

- $LiNbO_3$ devices are well developed:
  - Low loss, broad bandwidth phasemodulators for coherent systems and fibre sensors.
  - High-speed intensity modulators for long distance transmission systems.
  - Low crosstalk polarisation independent switches for switch arrays.

- Semiconductor devices are beeing developed for optoelectronic integration

- Biggest problem for guided wave optical modulaters and switches is not the device performance but the

SMALL MARKET

INTERNATIONAL ATOMIC ENERGY AGENCY
UNITED NATIONS EDUCATIONAL, SCIENTIFIC AND CULTURAL ORGANIZATION
INTERNATIONAL CENTRE FOR THEORETICAL PHYSICS
I.C.T.P., P.O. BOX 586, 34100 TRIESTE, ITALY, CABLE: CENTRATOM TRIESTE

UNITED NATIONS INDUSTRIAL DEVELOPMENT ORGANIZATION

INTERNATIONAL CENTRE FOR SCIENCE AND HIGH TECHNOLOGY

H4.SMR/540-30

Second Training College on Physics and Technology of Lasers and Optical Fibres

21 January - 15 February 1991

LIDAR Remote Sensing of the Environment

L. Pantani
IROE - CNR
Firenze, Italy

LIDAR REMOTE SENSING OF THE ENVIRONMENT

Authors

Giovanna Cecchi & Luca Pantani

IROE – CNR
Via Panciatichi, 64 – I 50127 FIRENZE (Italy)

LASER: irradiates the target

- generally pulsed
- wavelength depending on applications
- beam collimator optional

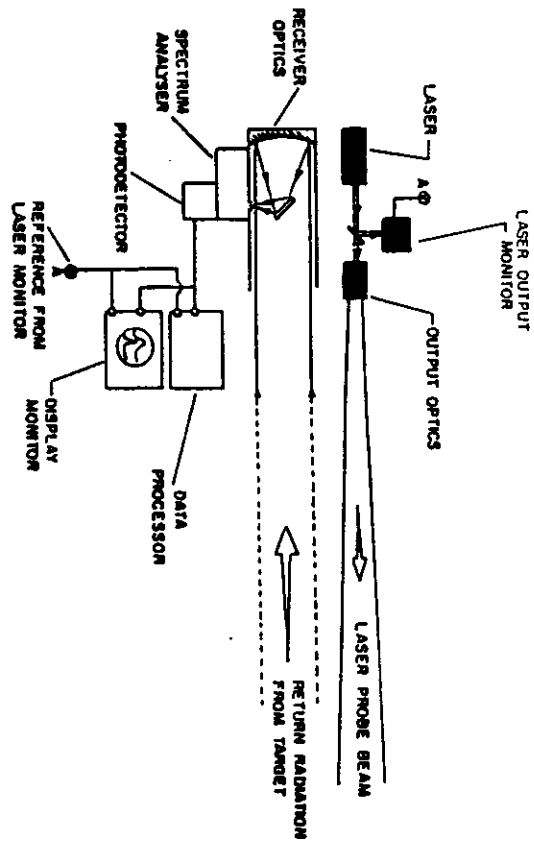

LIDAR – Light Detection And Ranging

* GIANT PULSE LASER (Mc. Clung & Hellwarth, 1962)
* LIDAR ANALYSIS OF THE UPPER ATMOSPHERE (Fiocco & Smullin, 1963)
* LIDAR ANALYSIS OF THE TROPOSPHERE (Ligda, 1963)
* DIFFERENTIAL ABSORPTION LIDAR (Schotland, 1966)
* RAMAN LIDAR (Inaba & Kobayasi, 1969)
* LIDAR BATHYMETRY (Hickman & Hogg, 1969)
* FLUORESCENCE LIDAR (Measures & Bristow, Fantasia et al., 1971)
* DIFFERENTIAL REFLECTANCE LIDAR (Wieseman et al., 1978)

IROE-CNR

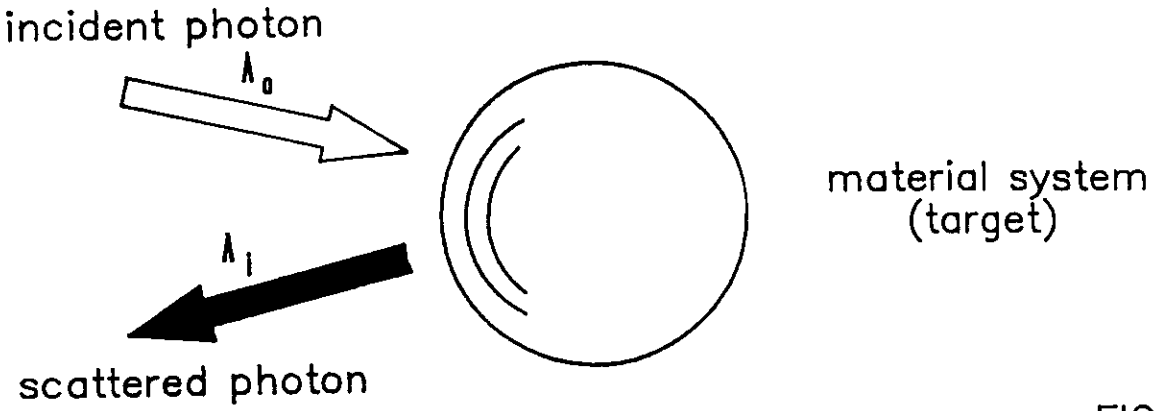
incident photon
λ_0
λ_1
scattered photon
material system
(target)

FIG. 2a

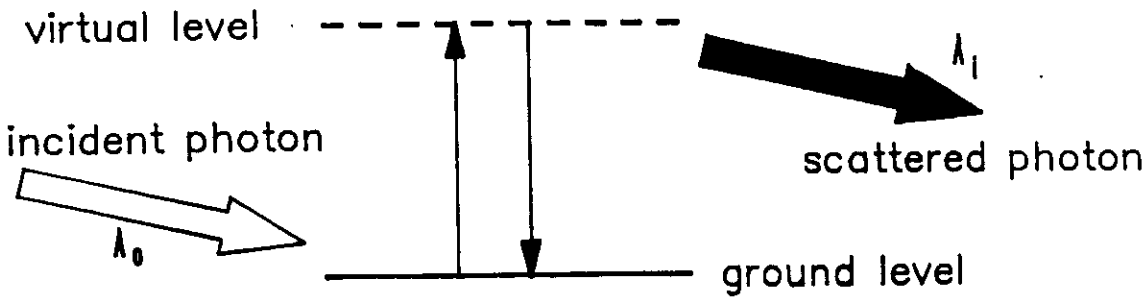
virtual level
incident photon
λ_0
λ_1
scattered photon
ground level

FIG. 2b

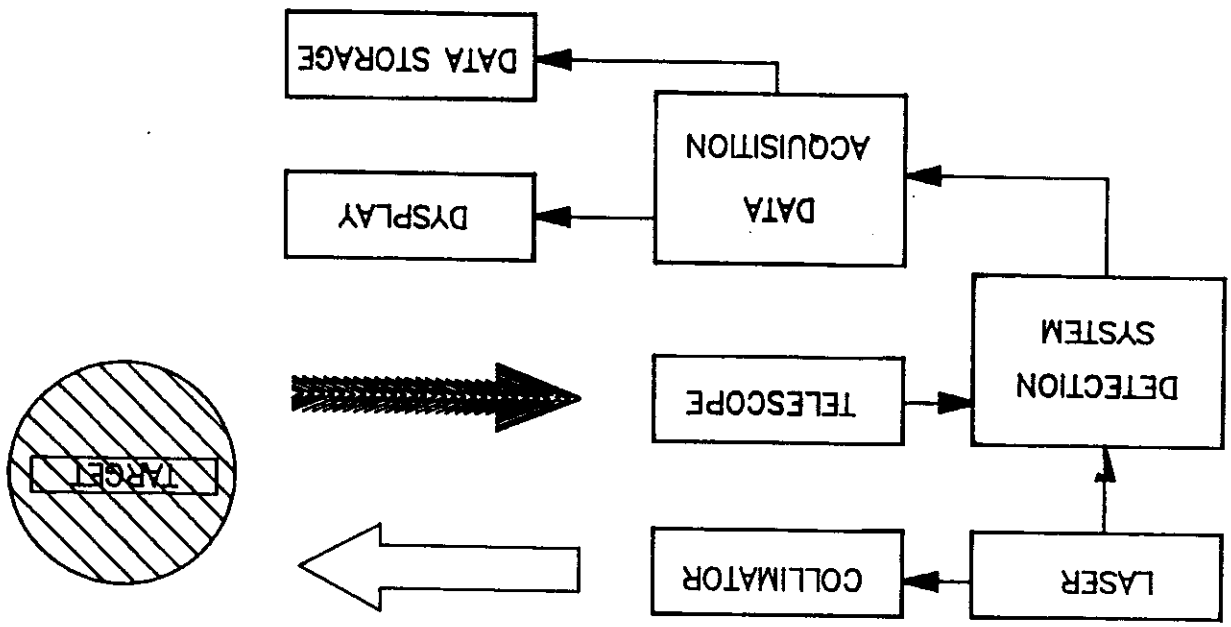
DATA STORAGE
DATA ACQUISITION
DISPLAY
DETECTION SYSTEM
TELESCOPE
TARGET
LASER
COLLIMATOR

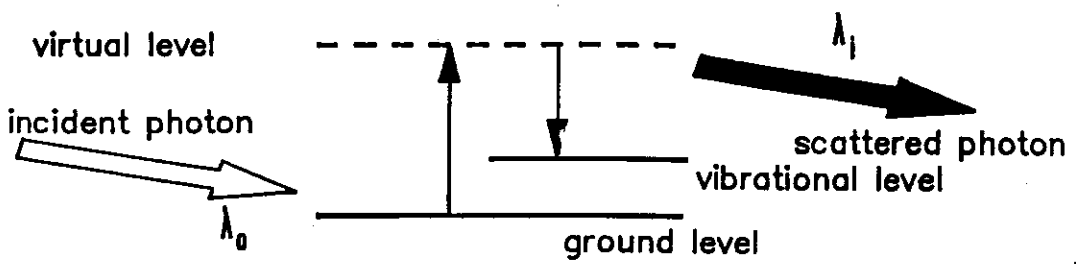

FIG. 3a

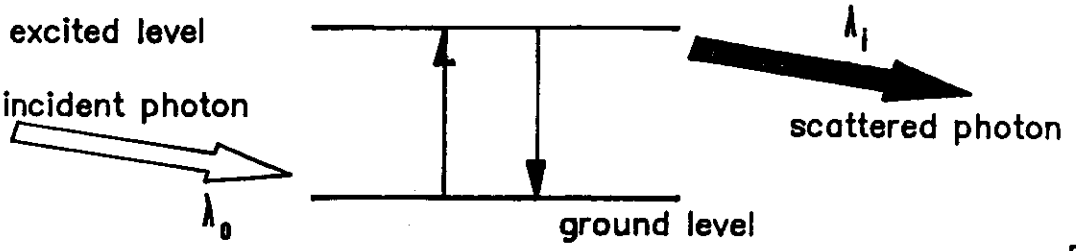

FIG. 3b

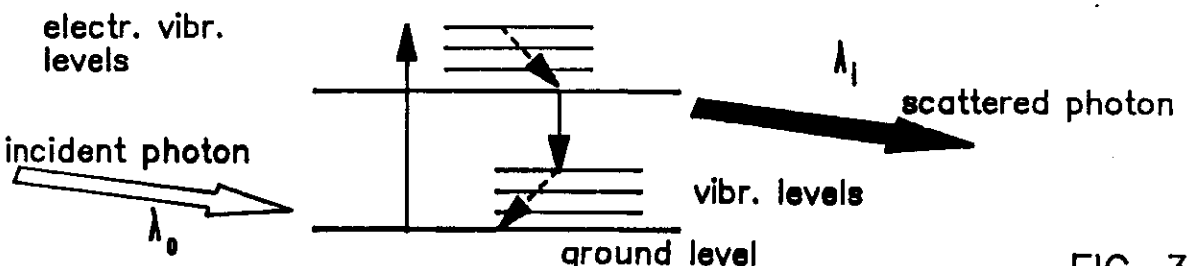

FIG. 3c

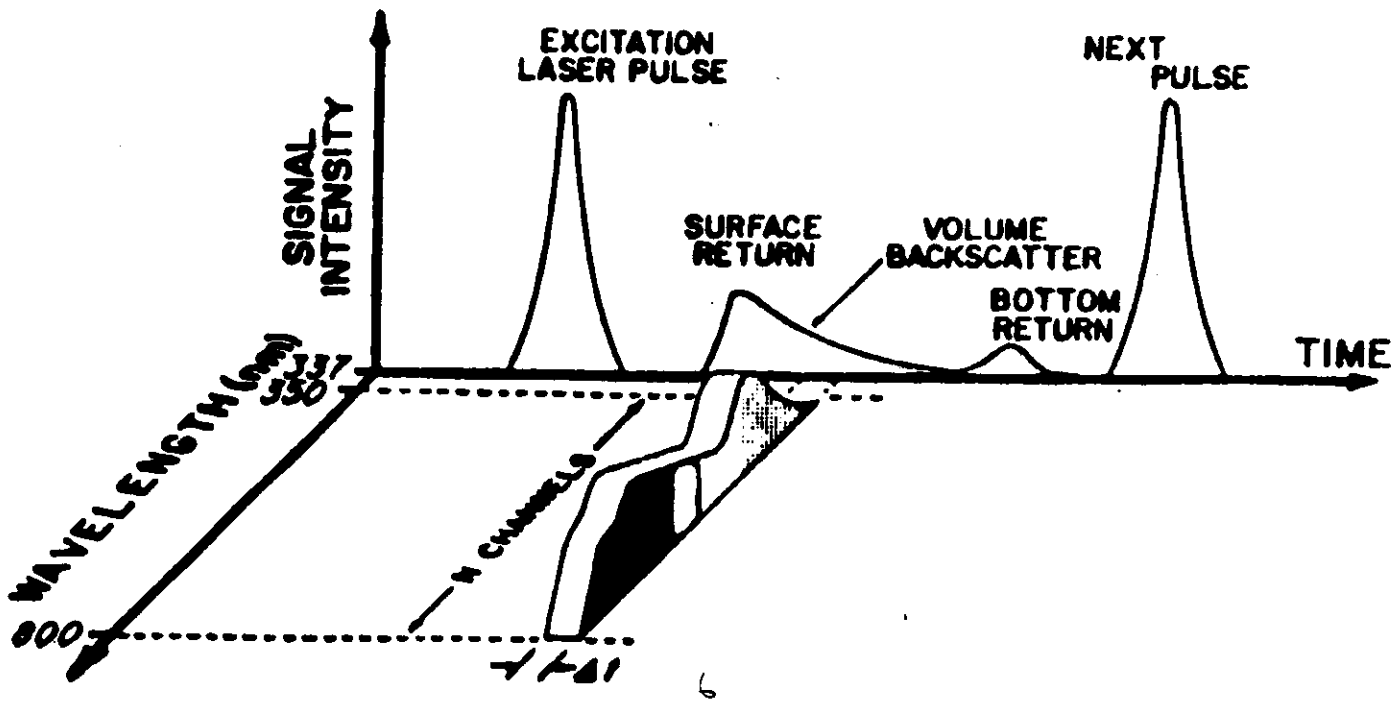

$$E_{o,i}(R) = K_{o,i} R^{-2} \beta_{o,i}(R) \exp\left[-\left(\int_R (\alpha_o(r) + \alpha_i(r))dr\right)\right]$$

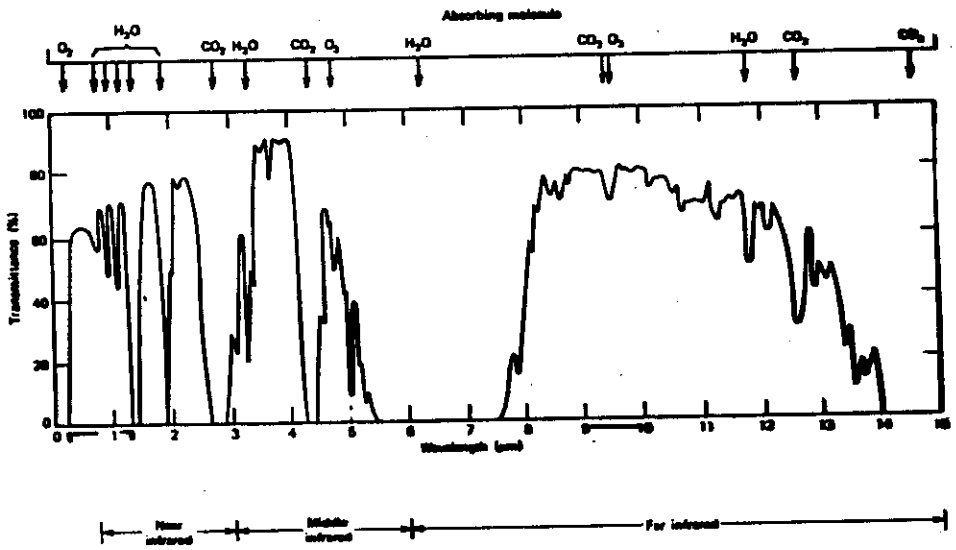

$$E_{o,i}(R) = K_{o,i} R^{-2} \beta_{o,i}(R) \exp\left[-\left(\int_R (\alpha_o(r) + \alpha_i(r))dr\right)\right]$$

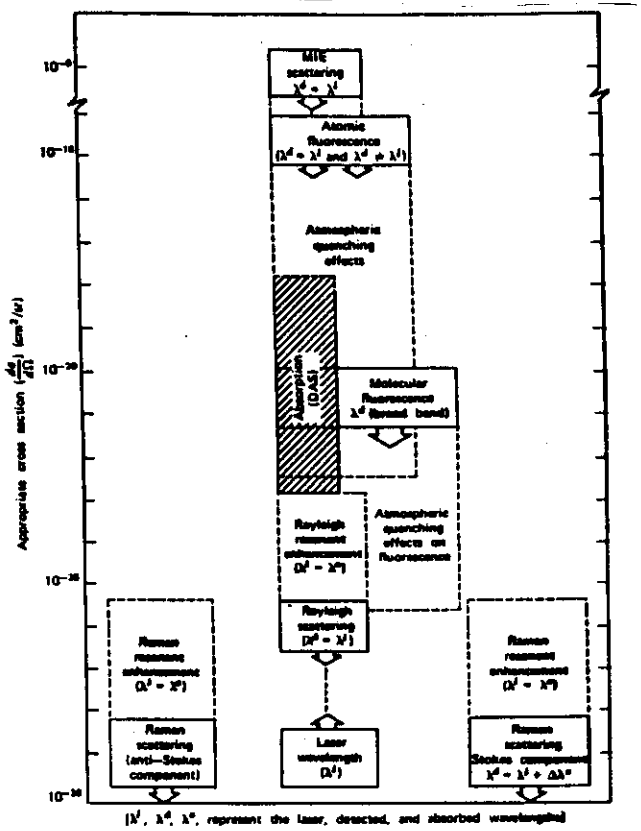

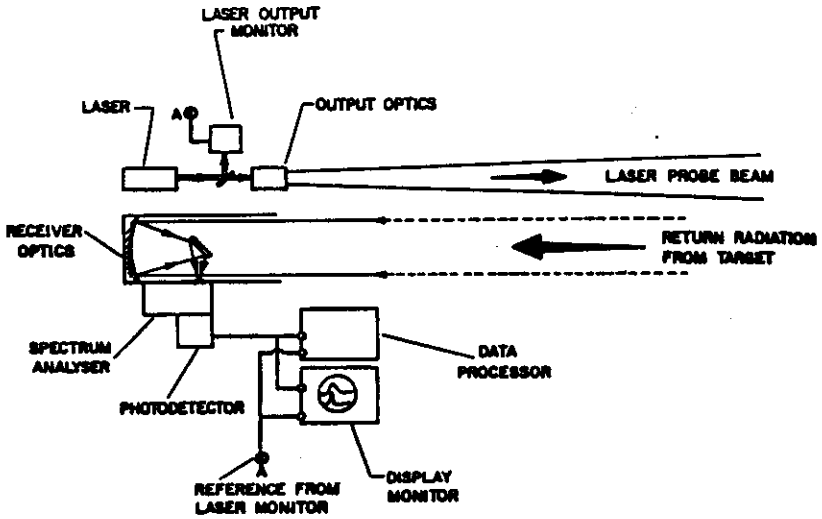

- LIDAR MONOSTATICO BIASSIALE

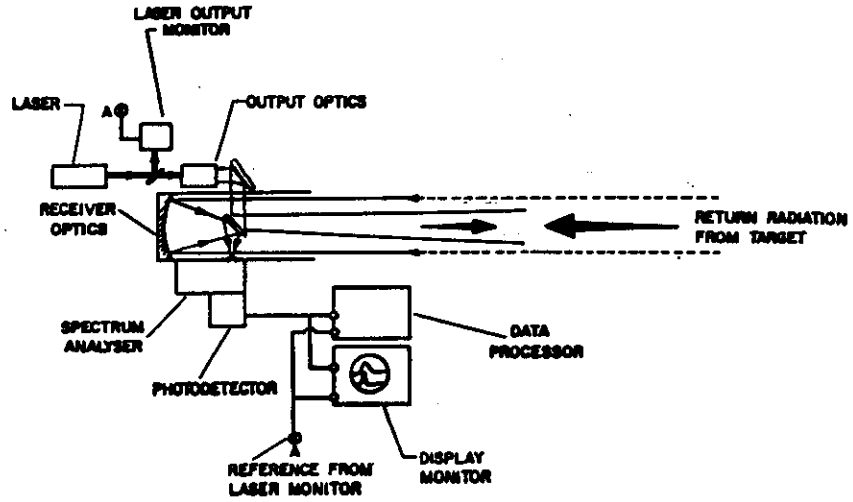

- LIDAR MONOSTATICO COASSIALE

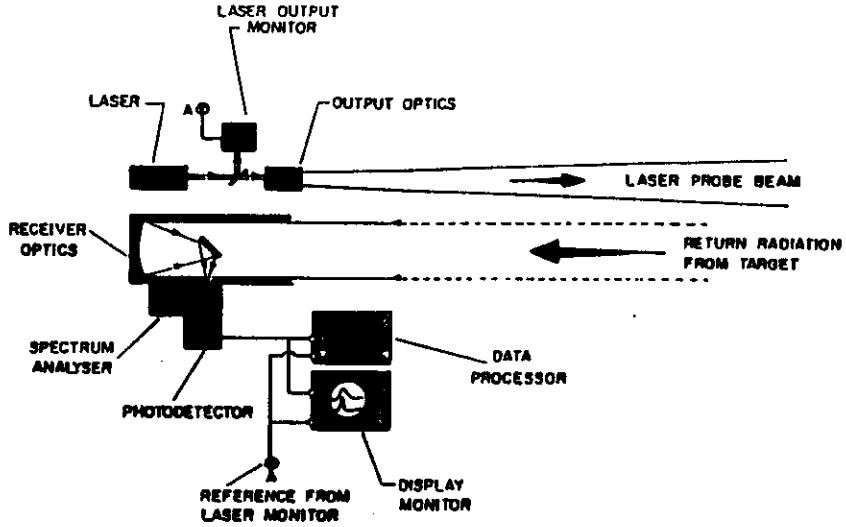

- LASER
- RECEIVER OPTICS
- OPTICAL SIGNAL ANALYSER
- PHOTODETECTOR
- DATA DISPLAY AND STORAGE

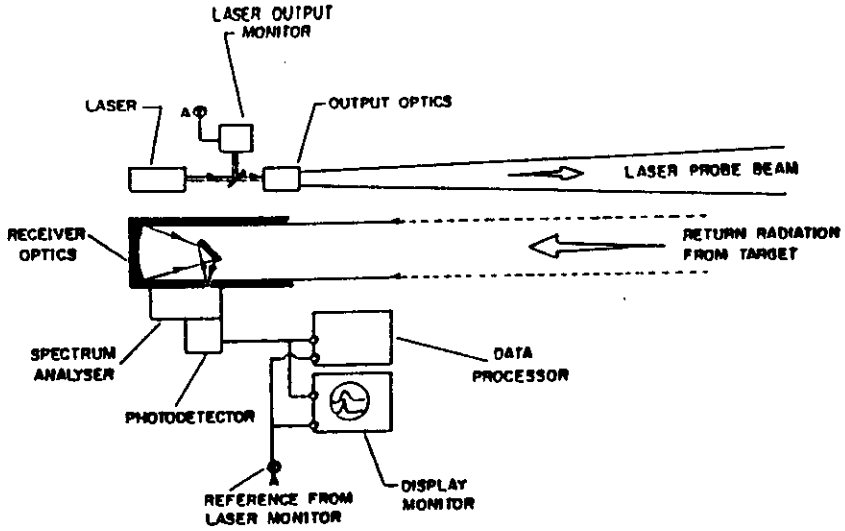

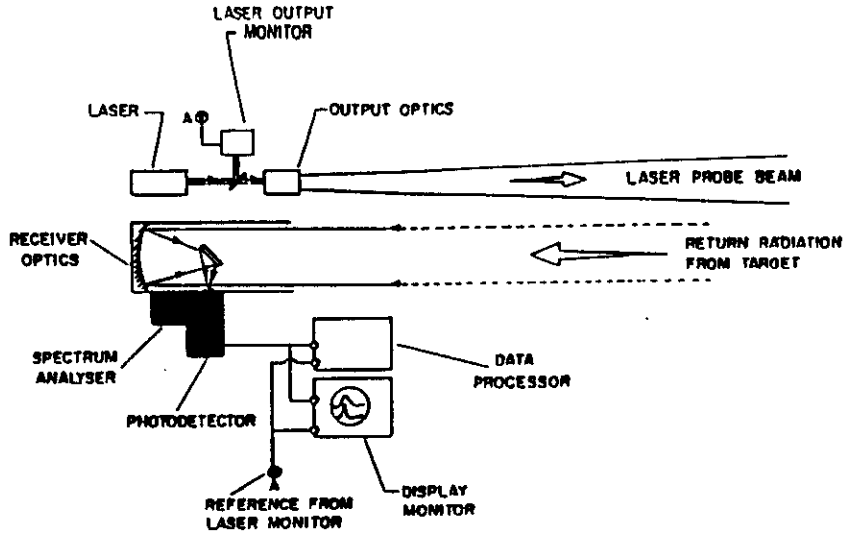

RECEIVER OPTICS: collects the backscattered radiation from the target

- Mirror telescopes are preferred

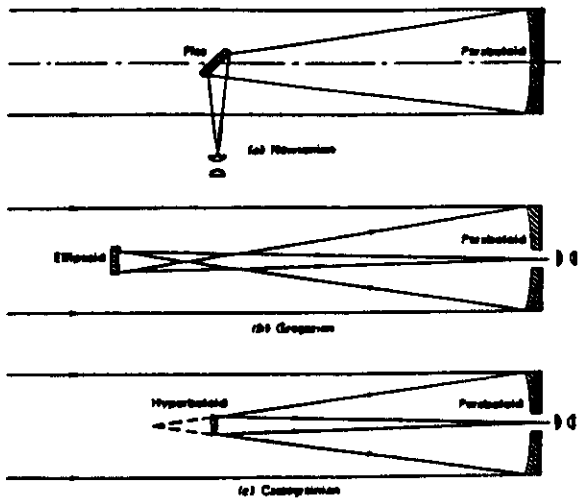

OPTICAL SIGNAL ANALYSER: discriminates the received wavelengths

- different channels with interferential filters
- grating spectrometer

PHOTODETECTOR: transforms the optical signal into an electrical one

- Photomultiplier
- Solid state detector
- Detector array

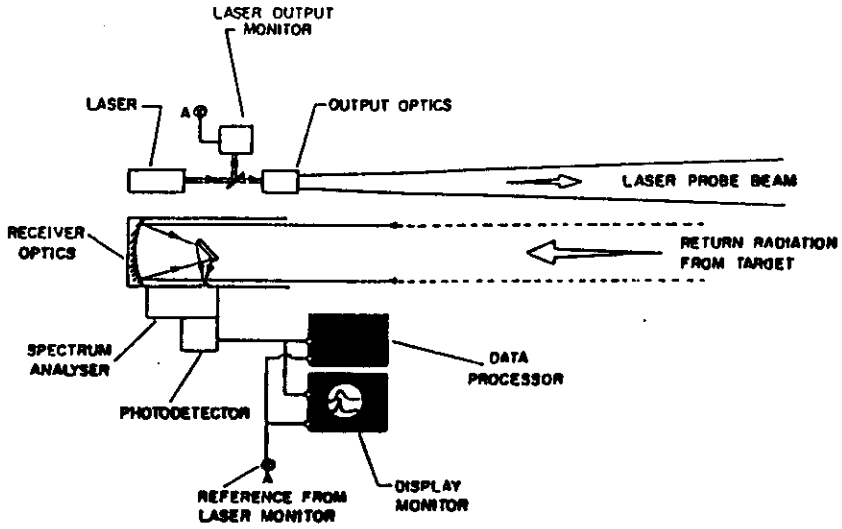

- DATA DISPLAY AND STORAGE
- Computer and peripherals

ATMOSPHERIC REMOTE SENSING

Elastic scattering:
- Turbidity
- Smoke plumes
- Cloud thickness
- Boundary layer altitude

Depolarization:
- Ice content of clouds

Differential absorption:
- Minor components
- Temperature and pressure

Doppler:
- Wind speed

IRDE-CNR

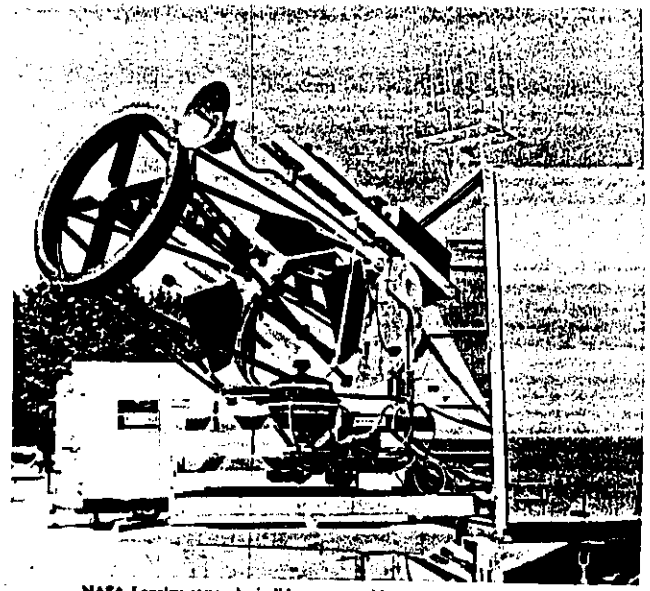

NASA Langley atmospheric lidar system with a receiver aperture of 1.22 m (Melfi et al., 1973).

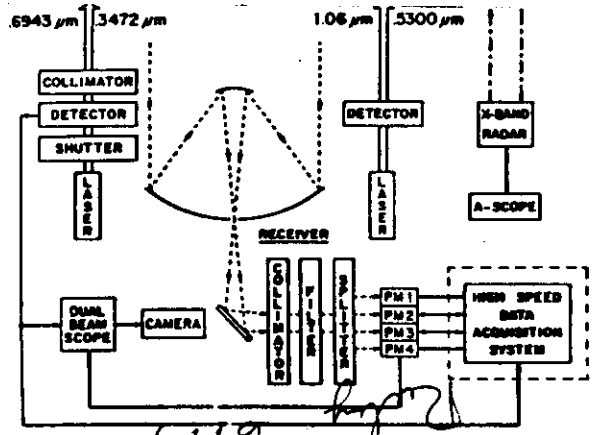

Schematic diagram of the 48-in. (1.22-m) NASA Langley lidar system (McCormick and Fuller, 1975).

NASTRO 2 FILE 26 DATA 17 : 2 : 83 ORE 18 : 50 : 9

NUM. TRACCE 1000 ELEV. 57 AZIM. 0

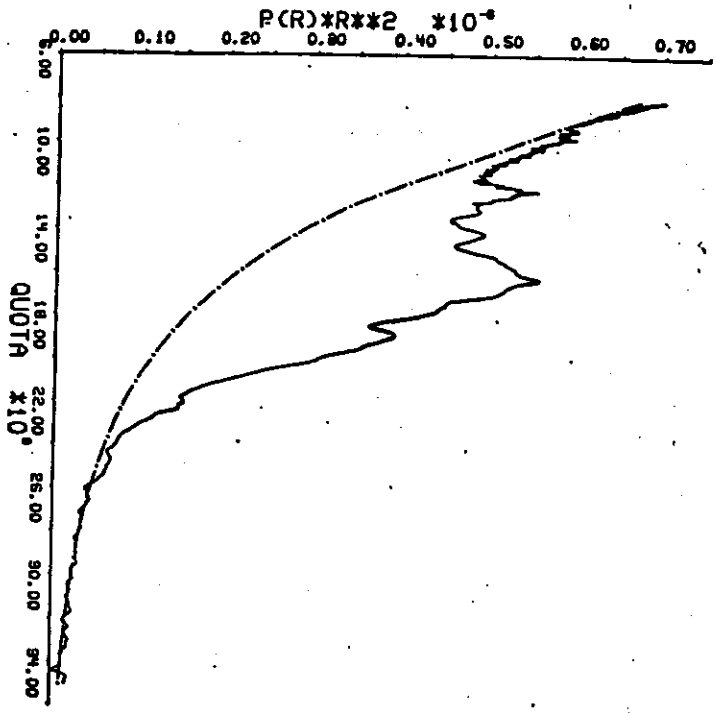

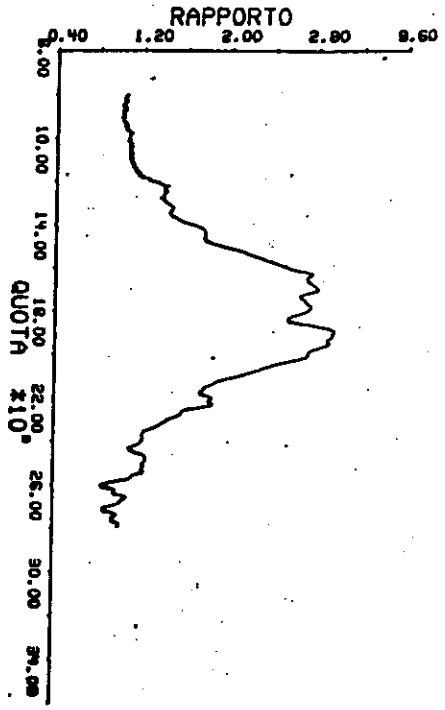

Programma Nazionale
di Ricerche in Antartide
CNR - IROE
Tethys Bay
74 deg. 41 min 55.8 sec S.
164 deg. 5 min 08.3 sec E.
date 8: 2:88 time 08: 9:26
int. backscatt. 2.84E-05

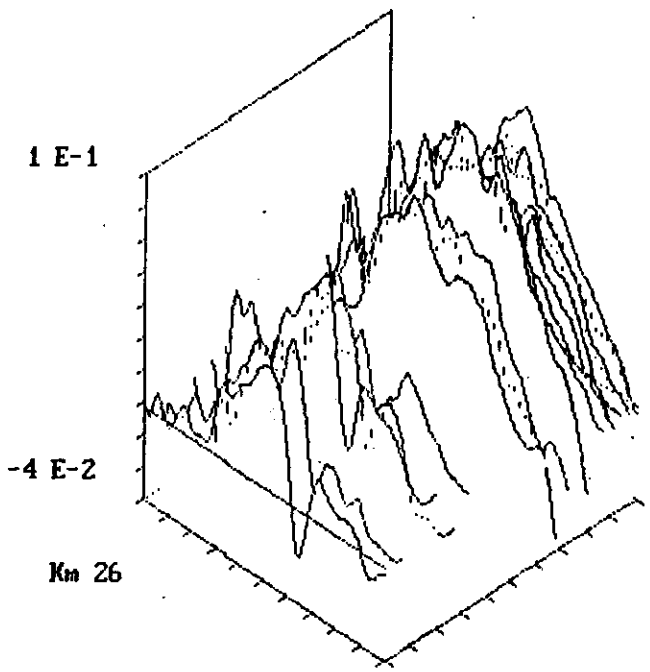

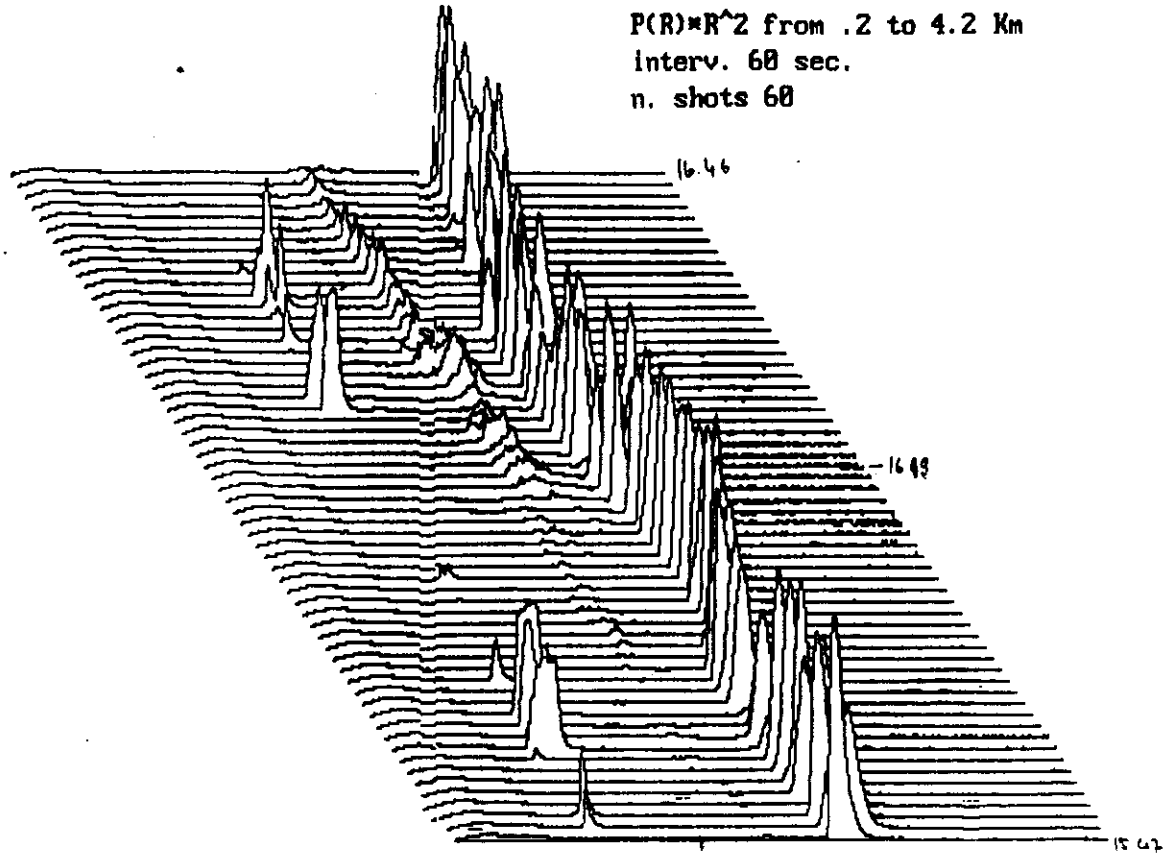

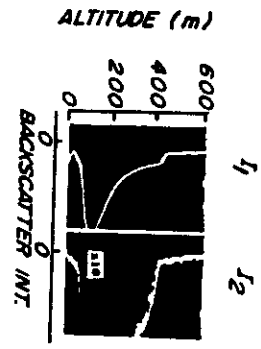

Example of 694-nm lidar returns at both polarizations, showing atmospheric features at the boundary of an urban mixing layer (McNeil and Carswell, 1975).

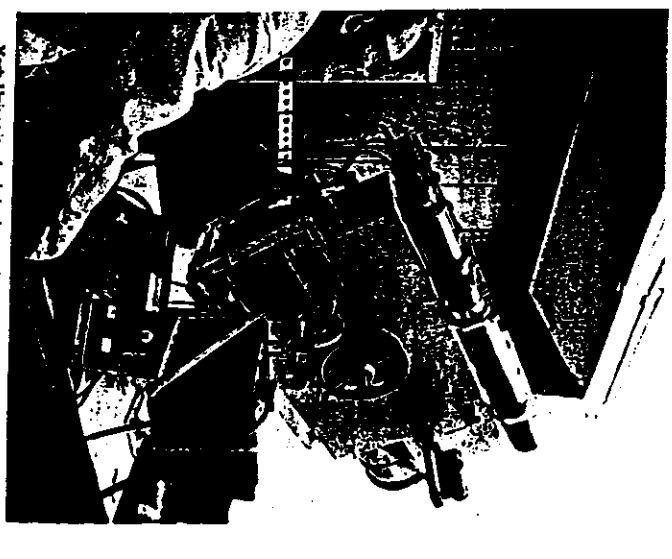

York University elastic backscattering lidar system (courtesy of A. I. Carswell).

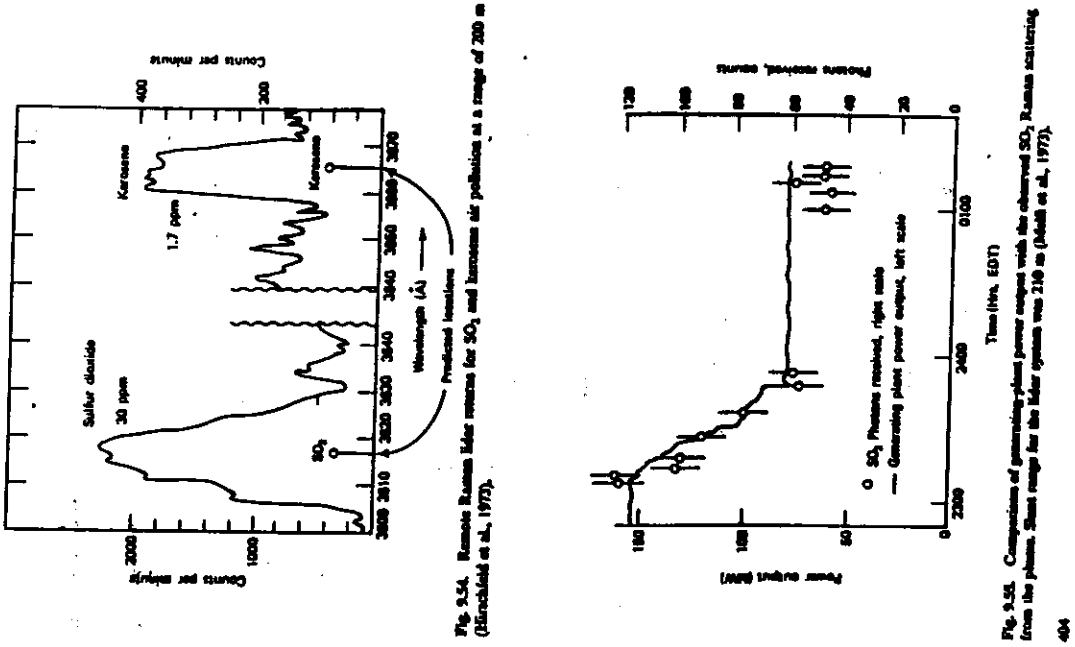

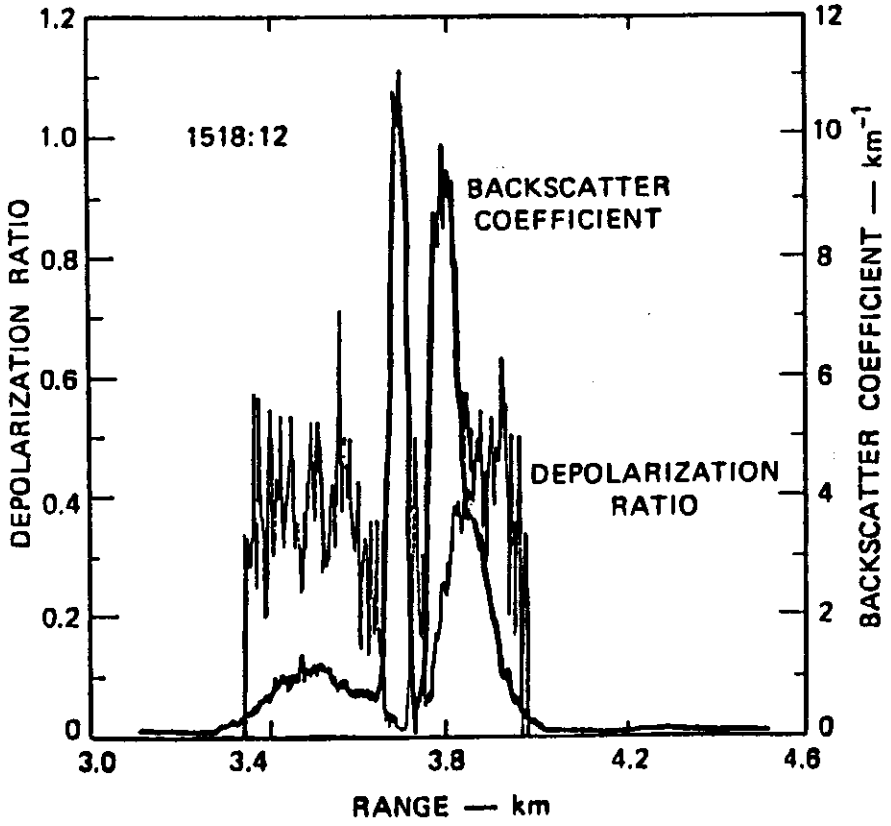

Fig. 9.22. Backscatter coefficient from mixed-phase (ice and water) altostratus clouds together with the depolarization ratio (Allen and Platt, 1977).

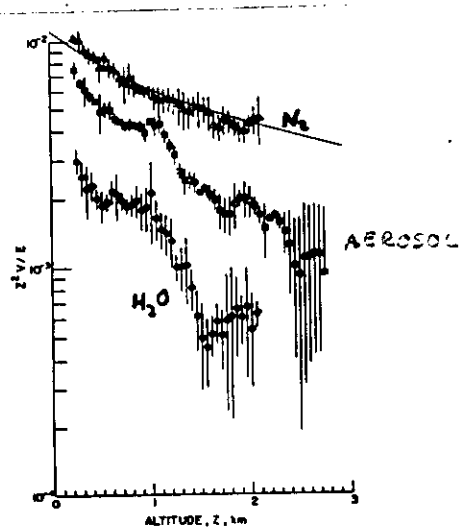

Typical backscattering profiles normalized for range Z and laser energy E (Z^2V/E) from the atmosphere: ▲, nitrogen, average of eight oscillograms; ●, water vapor, average of six oscillograms; ⊞, aerosol, average of six oscillograms, with two No. 1 n.d. filters; (solid curve), calculated return for nitrogen (Z^2V). V represents the voltage signal from the photomultiplier (Melfi, 1972).

– RAMAN MEASUREMENT OF WATER VAPOUR, AEROSOLS AND N_2 –

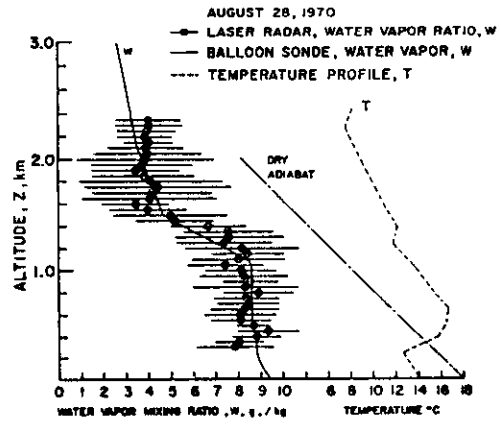

A

Lidar measurement of water-vapor mixing ratio compared with standard balloon-sonde data (Melfi, 1972).

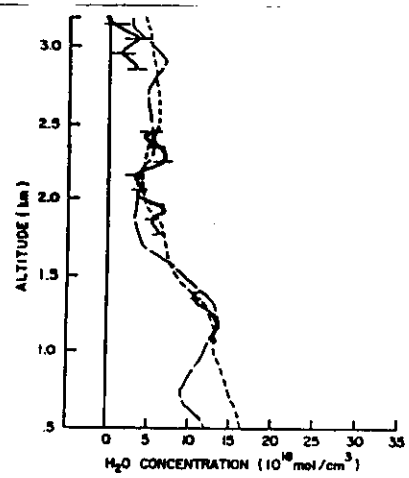

B

Vertical distribution of water vapor determined by a DIAL system (solid line), invol 100 laser firings, a 100-m-range cell, and a H_2O absorption cross section of 5.2×10^{-23} m^2. I from rawinsondes launched before (short dashes) and after (long dashes) DIAL measurements also displayed (Browell et al., 1979).

WATER VAPOUR PROFILES OBTAINED THROUGH RAMAN (A) AND DIAL (B) TECHNIQUES

MINOR CONSTITUENT DETECTION

Fluorescence (upper atmosphere)

Differential absorption (troposphere)

- O_3 (XeCl laser, CO_2 laser)
- SO_2 (Dye lasers)
- NO_2 (Dye lasers)
- H_2O (CO_2 laser)
- Ethylene (CO_2 laser)
- Combustion exhaust (CO_2 laser)

- The CO_2 laser can operate in coherent Lidars
- UV and VIS Lidars have more efficient detectors than CO_2 Lidars

IAOE-CNR

25

(4)

DIFFERENTIAL LIDAR:

■ DIFFERENTIAL ABSORPTION LIDAR:

TWO LASERS OF SLIGHTLY DIFFERENT WAVELENGTH.

λ_i - INSIDE AN ABSORPTION BAND

λ_o - OUTSIDE THE " "

$$\frac{P(\lambda_i,R)}{P(\lambda_o,R)} = \frac{\xi(\lambda_i)\,\beta(\lambda_i,R)}{\xi(\lambda_o)\,\beta(\lambda_o,R)} \exp\left\{-2\int_0^R [K(\lambda_i,R)-K(\lambda_o,R)]\,dR\right\}$$

■ DIFFERENTIAL RAMAN LIDAR:

TWO RAMAN WAVELENGTHS ONE OF WHICH CORRESPONDS TO A KNOWN COMPONENT OF THE ATMOSPHERE (NITROGEN):

λ_i - INVESTIGATED GAS

λ_o - KNOWN GAS

$$\frac{P(\lambda_i,R)}{P(\lambda_o,R)} = \frac{\xi(\lambda_i)\,\beta(\lambda_i,R)}{\xi(\lambda_o)\,\beta(\lambda_o,R)} \exp\left\{-\int_0^R [K(\lambda_i,R)-K(\lambda_o,R)]\,dR\right\}$$

TABLE 3.6. MEASURED ABSORPTION CROSS SECTIONS FOR GASEOUS SPECIES[a]

Molecule	$\tilde{\nu}$ (cm^{-1})	λ	$\sigma(\lambda_i)$ (10^{-18} cm^2)	$\varepsilon_A(\lambda)$ at STP ($(ppm\ cm)^{-1}$)
Acetylene, C_2H_2	719.9	13.89 μm	9.2	2.48×10^{-4}
Ammonia, NH_3	1084.6	9.220 μm	3.6	9.68×10^{-5}
Benzene, C_6H_6	1037.5	9.639 μm	0.09	2.42×10^{-6}
1,3-Butadiene, C_4H_6	1609.0	6.215 μm	0.27	7.26×10^{-6}
1-Butene, C_4H_8	927.0	10.787 μm	0.13	3.50×10^{-6}
Carbon monoxide, CO	2123.7	4.709 μm	2.8	7.53×10^{-5}
Carbon tetrachloride, CCl_4	793.0	12.610 μm	4.8	1.29×10^{-4}
Ethylene, C_2H_4	949.5	10.531 μm	1.34	3.60×10^{-5}
	950	10.526 μm	1.70	4.57×10^{-5}
Fluorocarbon-11, CCl_3F (Freon-11)	847	11.806 μm	4.4	1.18×10^{-4}
	1084.6	9.220 μm	1.24	3.34×10^{-5}
Fluorocarbon-12, CCl_2F_2 (Freon-12)	920.8	10.860 μm	11.0	2.96×10^{-4}
	923.0	10.834 μm	3.68	9.90×10^{-5}
Fluorocarbon-113, $C_2Cl_3F_3$	1041.2	9.604 μm	0.77	2.07×10^{-5}
Methane, CH_4	2948.7	3.391 μm	0.6	1.61×10^{-5}
	3057.7	3.270 μm	2.0	5.38×10^{-5}
Nitric oxide, NO	1908.1	5.265 μm	0.6	1.61×10^{-5}
	1917.5	5.215 μm	0.67	1.80×10^{-5}
Nitrogen dioxide, NO_2	1605.4	6.229 μm	2.68	7.21×10^{-5}
	22311.0	448.2 nm	0.2	5.38×10^{-6}
Ozone, O_3	1051.8	9.508 μm	0.9	2.42×10^{-5}
	1052.2	9.504 μm	0.56	1.51×10^{-5}
	39425.0	253.6 nm	12.0	3.23×10^{-4}
Perchloroethylene, C_2Cl_4	923.0	10.834 μm	1.14	3.07×10^{-5}
Propane, C_3H_8	2948.7	3.391 μm	0.8	2.15×10^{-5}
Propylene, C_3H_6	1647.7	6.069 μm	0.09	2.42×10^{-6}
Sulfur dioxide, SO_2	1108.2	9.024 μm	0.25	6.73×10^{-6}
	1126.0	8.880 μm	0.2	5.38×10^{-6}
	2499.1	4.001 μm	0.02[b]	5.38×10^{-7}
	33330.0	300.1 nm	1.0	2.69×10^{-5}
Trichloroethylene, C_2HCl_3	944.2	10.591 μm	0.56	1.51×10^{-5}
Vinyl chloride, C_2H_3Cl	948.0	10.638 μm	0.4	1.08×10^{-5}

[a] Based on the data presented by Hinkley et al. (1976).

[b] Recent measurements (Abramson and Pokrowsky, 1980) indicate an absorption cross section of 0.416×10^{-18} cm^2 for SO_2 at 3.9843 μm, corresponding to the $P_1(6)$ line of a DF laser.

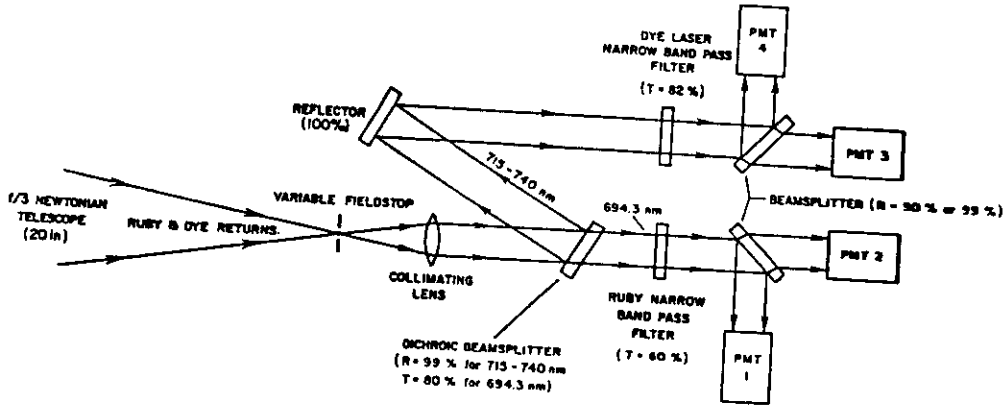

(a) (b)

(a) Schematic diagram and (b) photograph of the NASA water-vapor DIAL detection system (Browell et al., 1979).

— OFF LINE RUBY LASER 694.3 nm

— ON LINE RUBY PUMPED DYE LASER 724.37 nm

(a)

(a) The NASA DIAL system aboard the Wallops Flight Centre Electra aircraft; (b) schematic of the system (Bunsell, 1982b).

(a)

(a) Mobile lidar system of the National Swedish Environmental Protection Board; (b) schematic view of the system (Frederiksson et al., 1981).

Balloon-borne lidar facility: (a) artist's representation of the layout, (b) schematic diagram of transmitter system. All wavelengths are in micrometers (Hoppe et al., 1982)

— LASER INDUCED FLUORESCENCE OF OH

— DIFFERENTIAL ABSORPTION OF O_3

Fig. 4. DIAL measurement of SO_2 in the ambient air at a local street in a sulphuric acid plant area. The direction for the laser beam is given by the horizontal axis.

Fig. 5. Charting of SO_2 concentrations in a paper-mill area. Each level represents 100 $\mu g/m^3$. DIAL measurements in 36 directions were made for the charting.

Comparison of airborne DIAL and in situ O_3 data obtained in the vicinity of Salisbury, Maryland, during EPA field experiments (Browell, 1982a).

Comparison of DIAL and ozonesonde measurements of ozone layers in the vicinity of the tropopause (Browell, 1982b).

DIAL return signals from the atmospheric aerosols at the P(14) O_3 on-line (dashed curve) and P(24) off-line (solid curve) wavelengths of the CO_2 laser (Azzai et al., 1979).

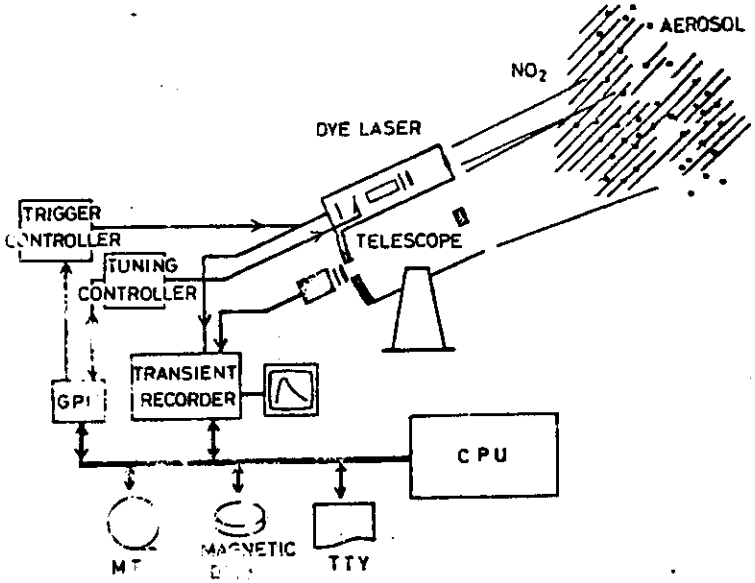

Fig. 1 Schematic diagram of the System

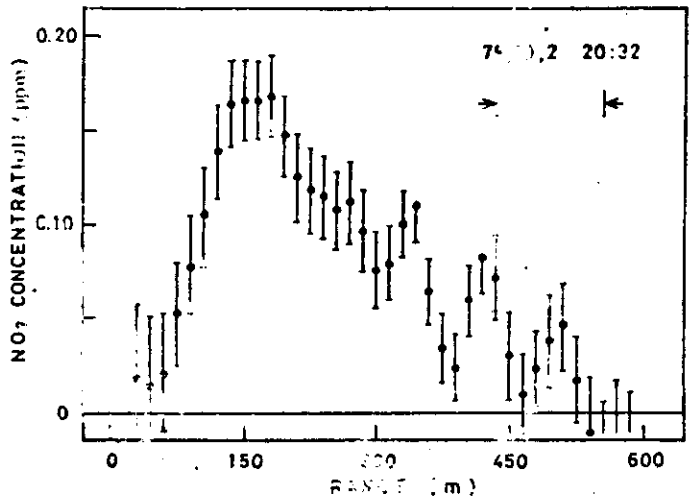

Fig. 2 NO_2 concentration profile obtained from 50 pulse-pair averages

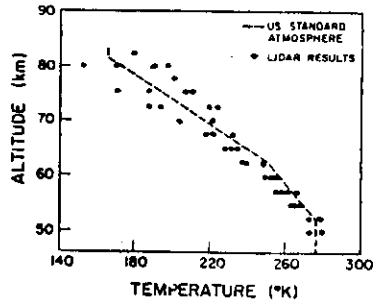

Upper-atmospheric temperature profile deduced from lidar elastic-backscattering measurements at Wakefield, England, by Sandford (1967).

$$T(z) = \frac{N(z_i)kT(z_i) + \int_{z_i}^{z} W_a(z)\,dz}{N(z)k}$$

$W(z)$ WEIGHT OF AIR PER cm^3
z_i : MAX. ALTITUDE
$T(z_i)$ ESTIMATED

TEMPERATURE MEASUREMENTS

- SANFORD — BASED ON THE CHANGEMENT IN DENSITY, AND THEREFORE IN RAYLEIGH SCATTERING, DUE TO TEMPERATURE
- STRAUCH — USE OF THE N_2 RAMAN
- COONEY — DIFFERENTIAL RAMAN TECHNIQUE BASED ON THE CHANGEMENTS OF THE ROTATIONAL RAMAN-BACK-SCATTERING. (ACCURACY ± 3 °C)
- MASON — DIFFERENTIAL ABSORPTION LIDAR BASED ON THE DEPENDENCE OF THE ABSORBANCE OF A KNOWN COMPONENT FROM TEMPERATURE (ACCURACY ± 1.5 °C)

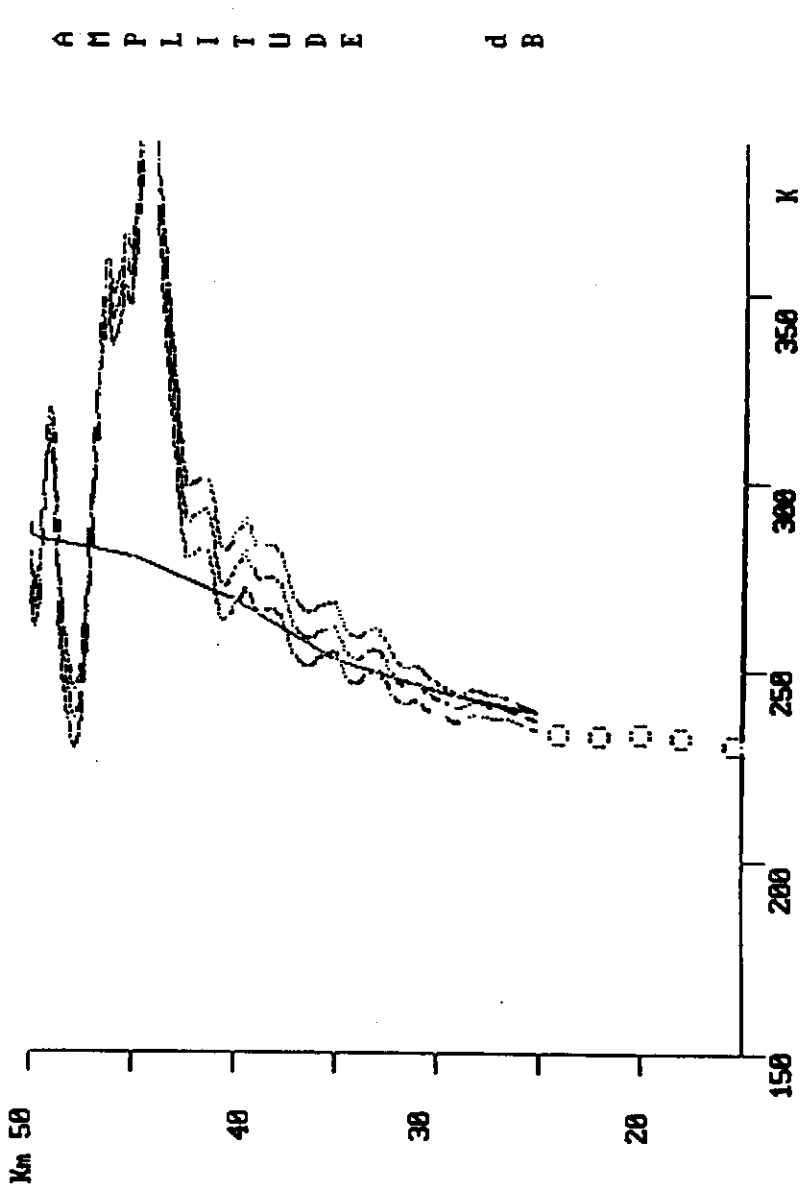

TEMPERATURA STRATOSFERICA DA DATI LIDAR
NOME DEL FILE :d:s0702040.257
FINESTRA DI FILTRAGGIO (m) ;(sotto,sopra 45 Km) : 1000 1000
quota di apodizzazione : 70000
data del radiosondaggio: 2/7/88 , Italian Base

WIND MEASUREMENTS

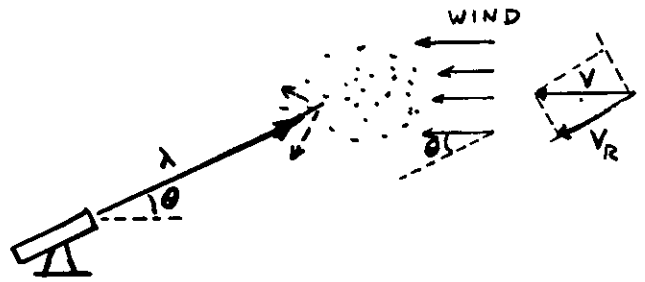

$$\Delta f = \frac{2V_R}{\lambda}$$

DOPPLER SHIFT

- HIGH COHERENCE LASERS
  COHERENCE LENGTH MUCH GREATHER THAN THE PROPAGATION PATH
- CO_2 LASER WITH ETERODYNE RECEIVER

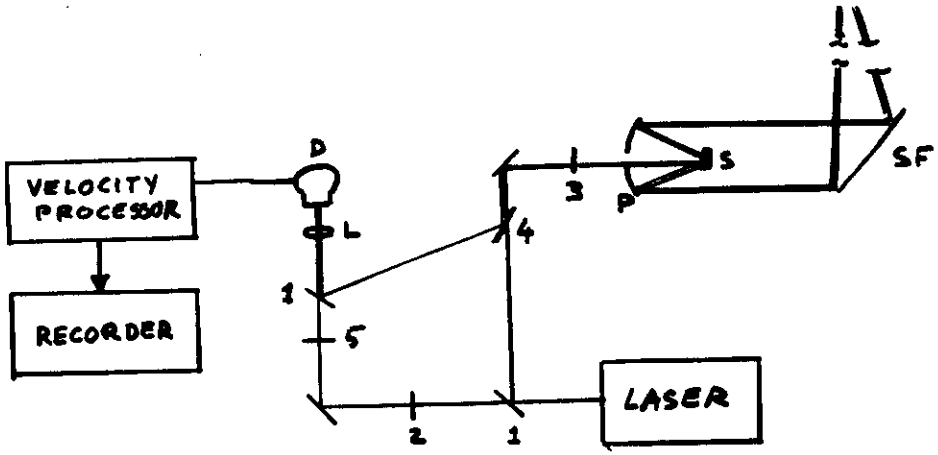

—— TRANSMITTED BEAM

—— RECEIVED BEAM

1 BEAM SPLITTER

2 ATTENUATOR

3 QUARTER WAVE PLATE

4 BREWSTER PLATE

5 HALF WAVE PLATE

D DETECTOR

L LENS

P PRIMARY MIRROR

S SECONDARY MIRROR

SF SCANNING FLAT

CW DOPPLER VELOCIMETER

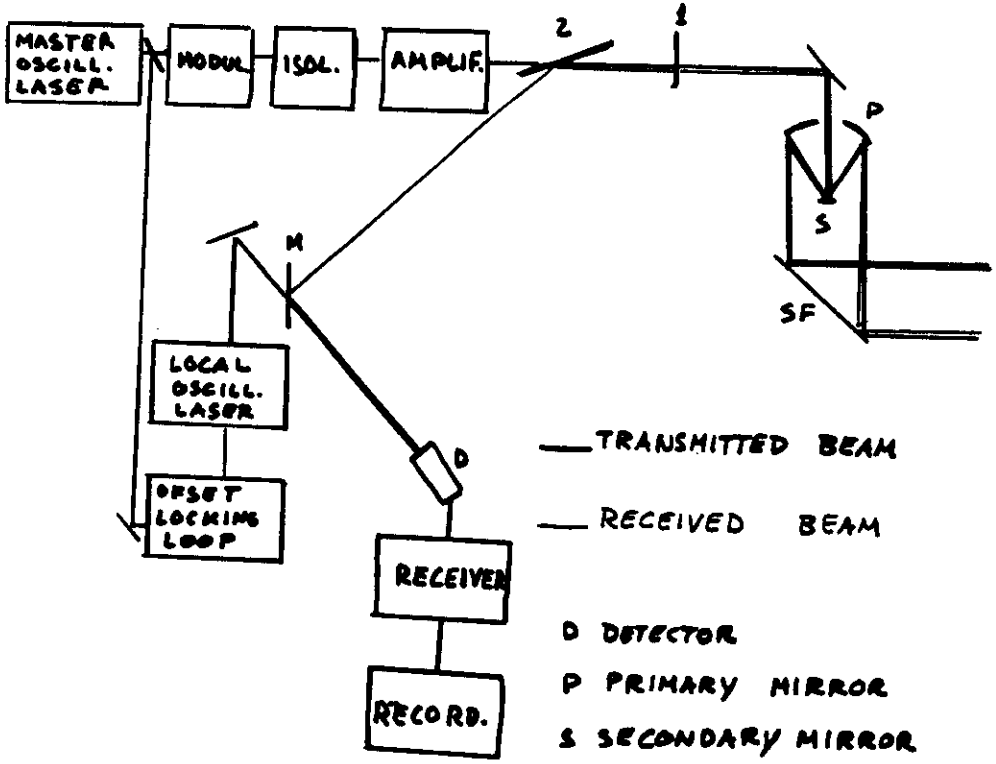

—— TRANSMITTED BEAM

—— RECEIVED BEAM

D DETECTOR

P PRIMARY MIRROR

S SECONDARY MIRROR

SF SCANNING FLAT

1 QUARTER WAVE PLATE

2 BREWSTER PLATE

M MIXING SPLITTER

PULSED LASER VELOCIMETER

BACKSCATTERING VELOCIMETER

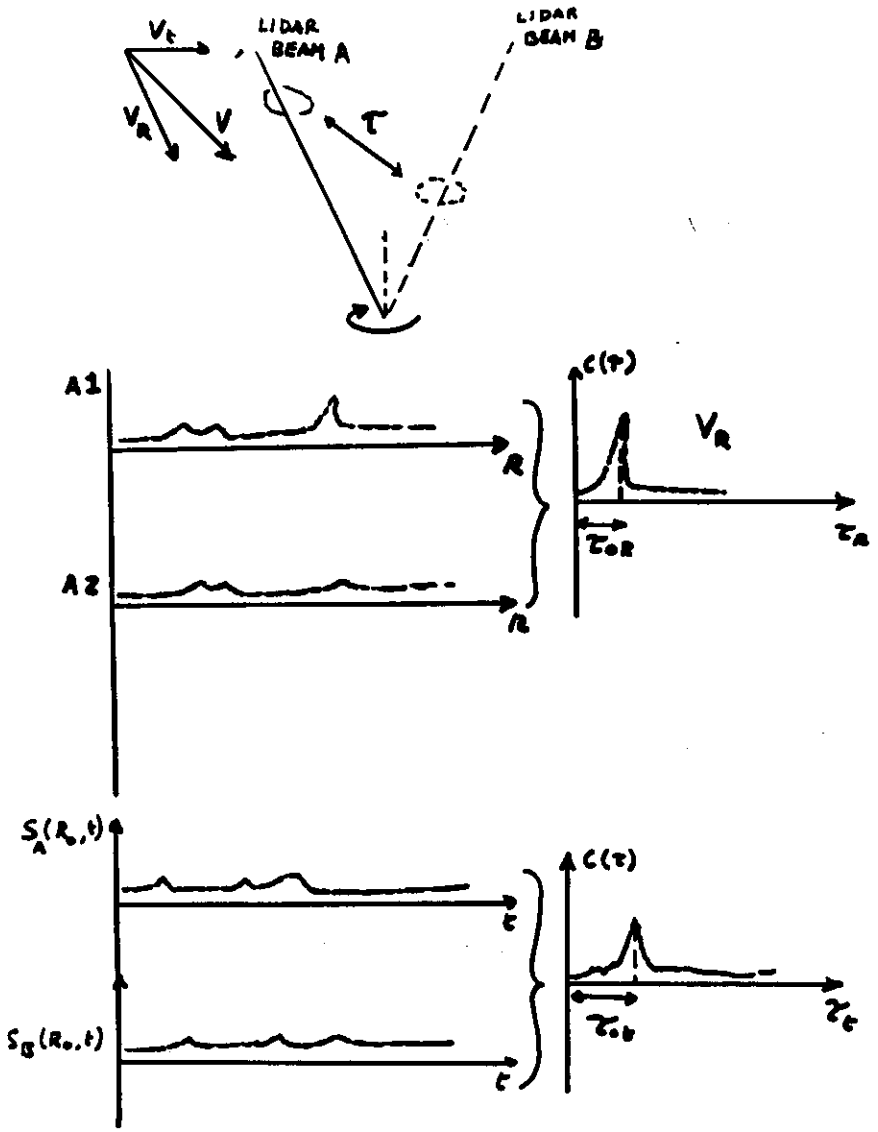

DOPPLER VELOCIMETER

- CORRELATION OF 0.97 – 0.98 WITH COUP ANEMOMETER
- 4 ÷ 6 Km RANGE
- APPLICATIONS:
  - WIND SHEAR AND GUST FRONTS
  - DUST DEVILS
  - TORNADOES
  - CAT
  - PLUME VELOCITY PROFILES

BACKSCATTERING VELOCIMETER

- FEW DATA AVAILLABLE

Lidar Technique	parameter	Altitude range	resolution	Accuracy
Elastic Backscatt. Lidar	Trop. Aerosols	0 - Tropopause	0.1	10 %
	Strat.Aerosols	Tropopause-40	1	20 %
	Trop. Cloud Base	0 - 7	0.1	100 m
	Cloud Base & Top & Opt. Depth for thin clouds	0 - 15	0.1	100 m
	Cirrus Clouds ice/water	5 - 15	0.1	-
	Temperature Profile	30 - 70	2	2°K
DIAL Lidar	Vertical Pres. Profile	0 - 10	1	.1-.5%
	Vertical Temp. Profile	0 - 10	2	1°K
	Water Vapor	0 - 20	2	10 %
	Ozone Vert. Distribution	10 - 20 20 - 50	1 1	2 % 2 %
	Species Dist.	0 - 15	1	10-20%
Raman Lidar	Temperature Water Vapor Species Dist.	0 - 5 0 - 10 0 - 1	0.2 0.1 - 0.2 0.1	1°K 10 % -
Fluorescent Lidar	Sodium Layer	80 - 100	1 - 2	-
Doppler Lidar	Winds(aerosols)	0 - 25	1	1 m/s

LAND AND WATER REMOTE SENSING

Elastic scattering:
- Bathymetry
- Water turbidity
- Vegetation thickness
- Ground profile

Fluorescence & Raman:
- Oils
- Phytoplankton
- Dissolved and suspended materials
- Water turbidity
- Temperature and salinity
- Vegetation stress

Differential reflectance:
- Vegetation stress and diseases
- Geological species identification
- Vegetation identification

IROE-CNR

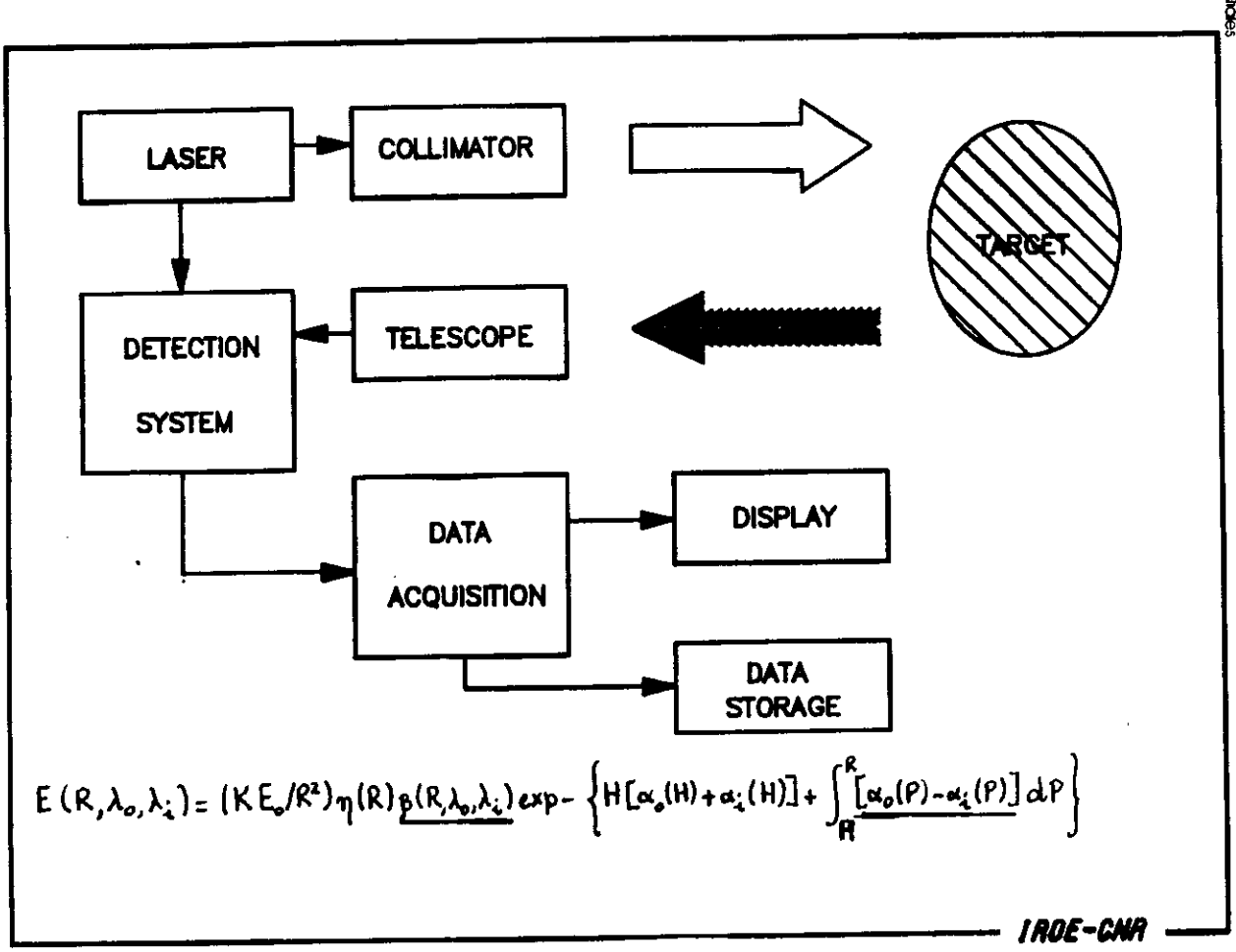
LASER
COLLIMATOR
TARGET
DETECTION SYSTEM
TELESCOPE
DATA ACQUISITION
DISPLAY
DATA STORAGE
$E(R,\lambda_o,\lambda_i) = (K E_o/R^2)\eta(R)\beta(R,\lambda_o,\lambda_i)\exp-\left\{H[\alpha_o(H)+\alpha_i(H)]+\int_R^R[\alpha_o(P)-\alpha_i(P)]\,dP\right\}$
IROE-CNR

45

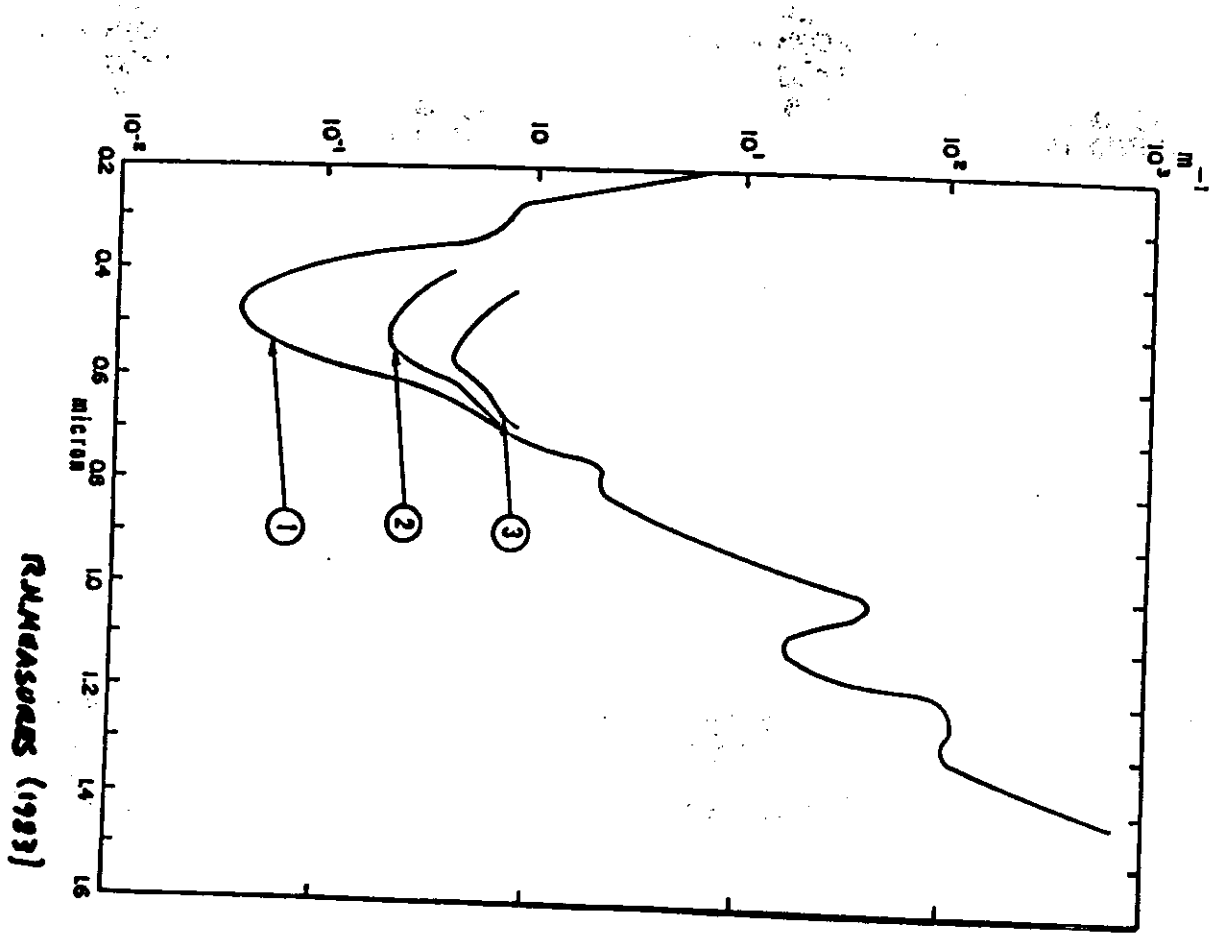
0.2
0.4
0.6
0.8
1.0
1.2
1.4
1.6
microns
1
2
3
R.M. MEASURES (1983)

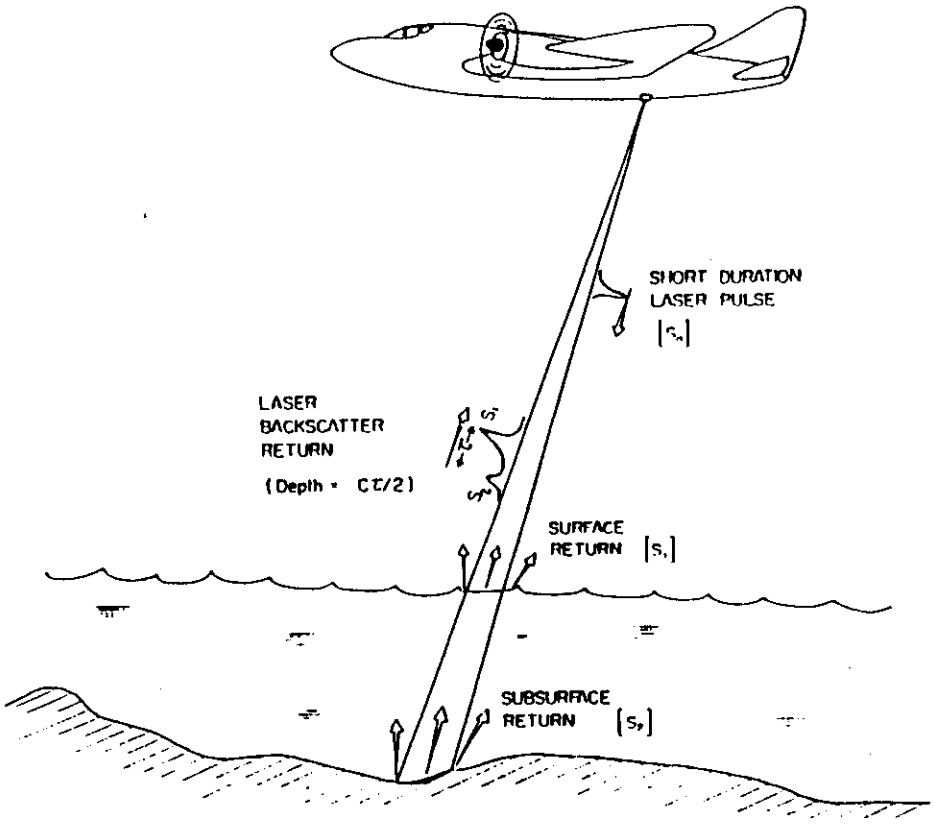

Fig. 10.2. Pictorial representation of airborne laser bathymetry.

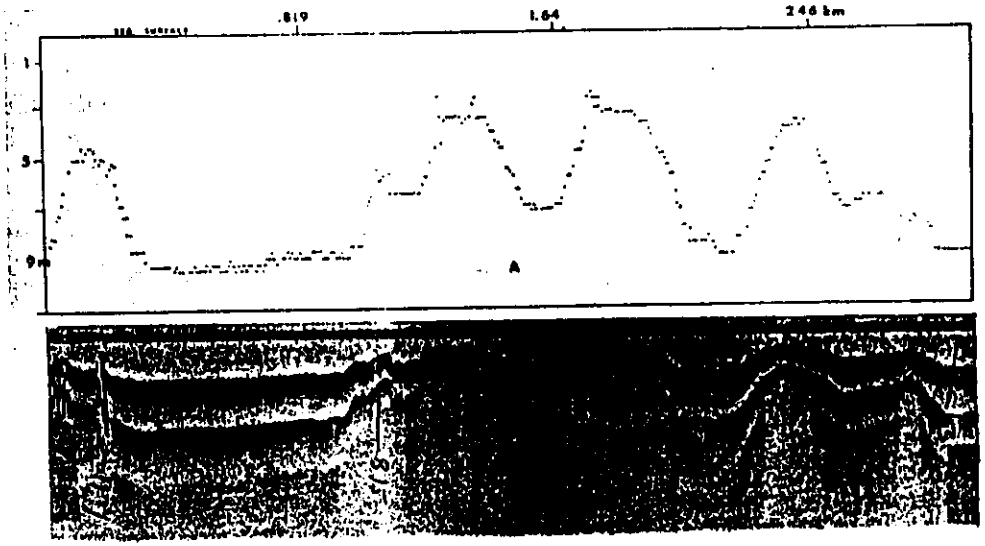

Fig. 10.5. Ocean floor profile: A, determined by an airborne bathymetric lidar; B, a matching sonar chart (Kim et al., 1975).

Depth profiles of the attenuation coefficient c = c(450nm) + c(533nm) averaged over half a kilometer flight distance. Depth resolution about 1 m. Realistic values only for water depths greater than 1 m.

Date : 31.8.84
Time : 18:22-18:48
Start point : 45°19'N 12°56'E
End point : 45°19'N 12°39'E

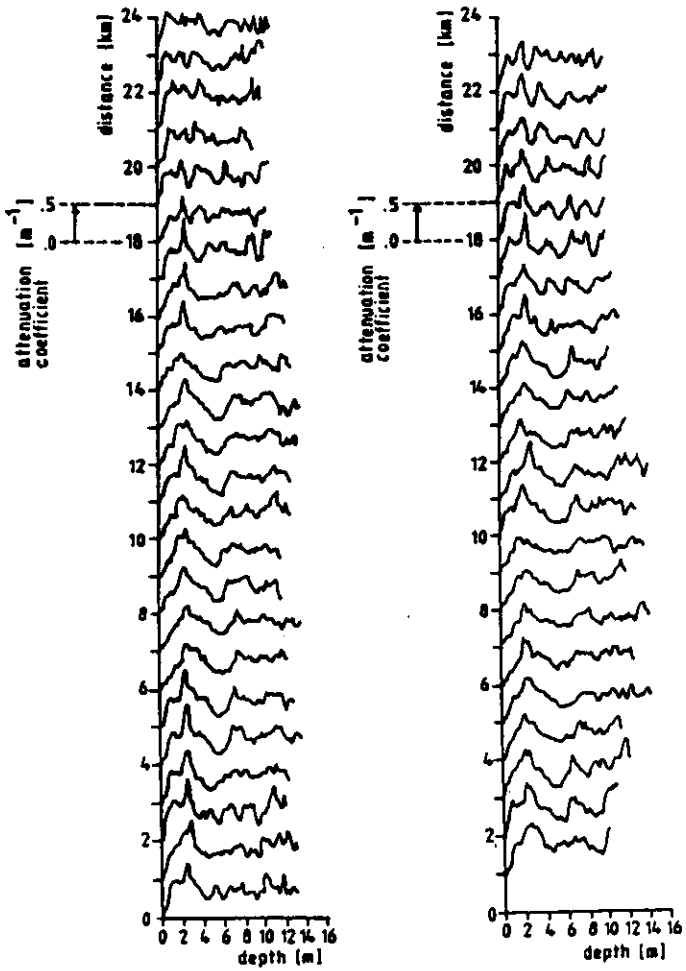

4.2.14

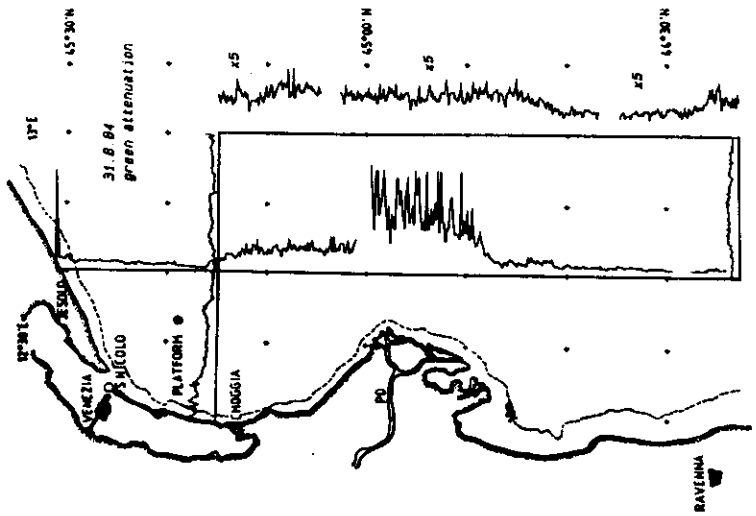

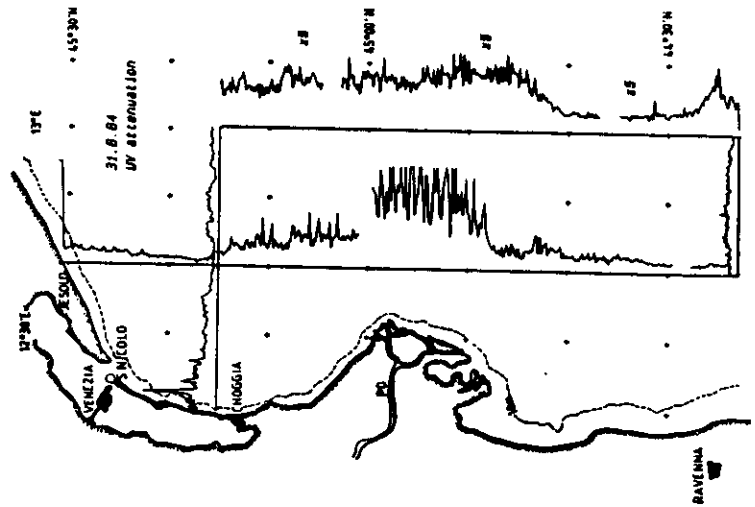

4.2.13

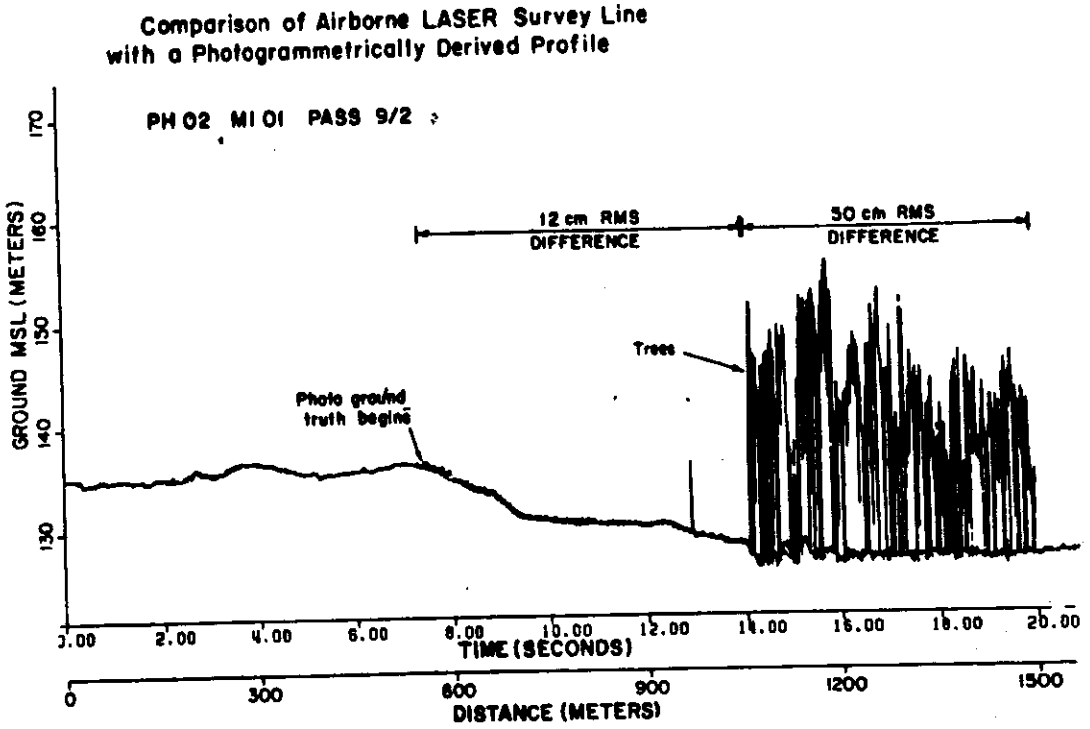

Figure 9. Comparison of AOL data with ground truth.

51

APPLICATIONS

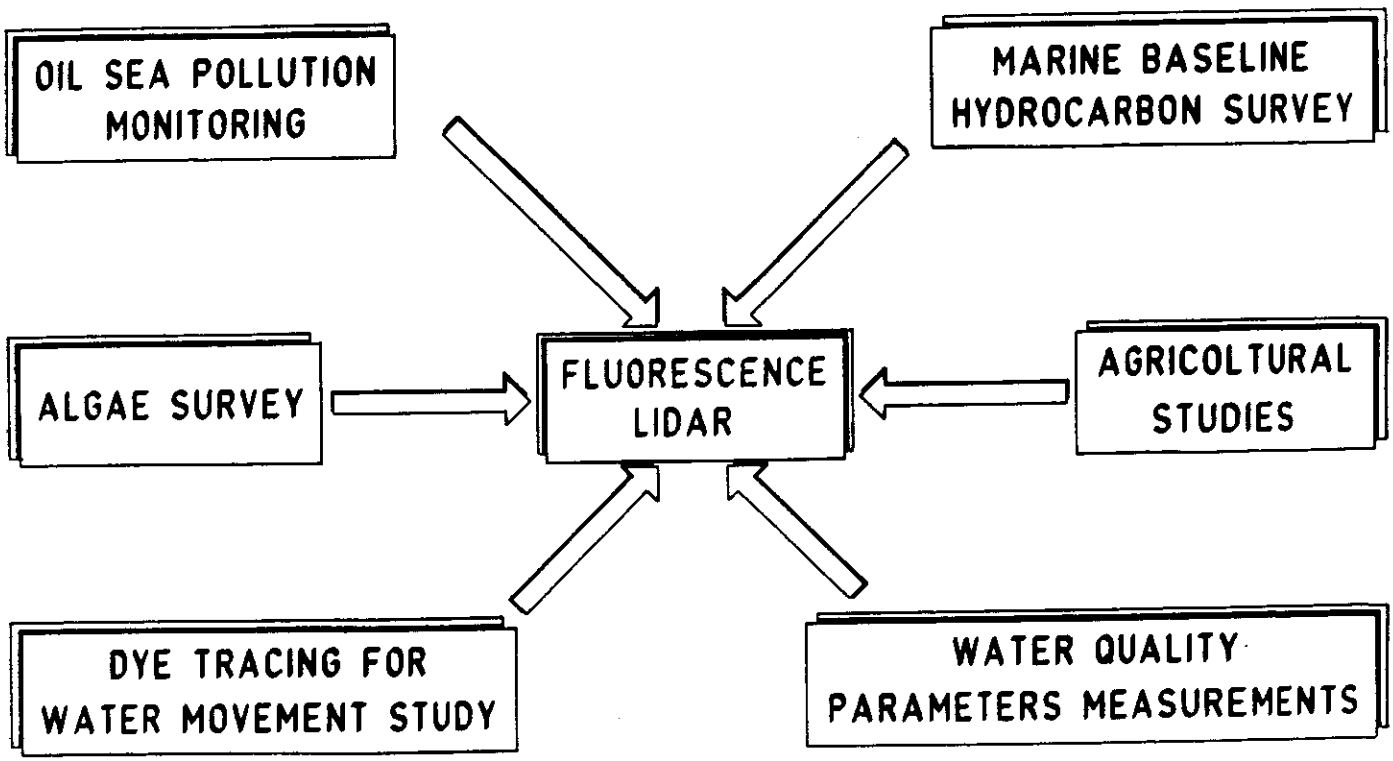

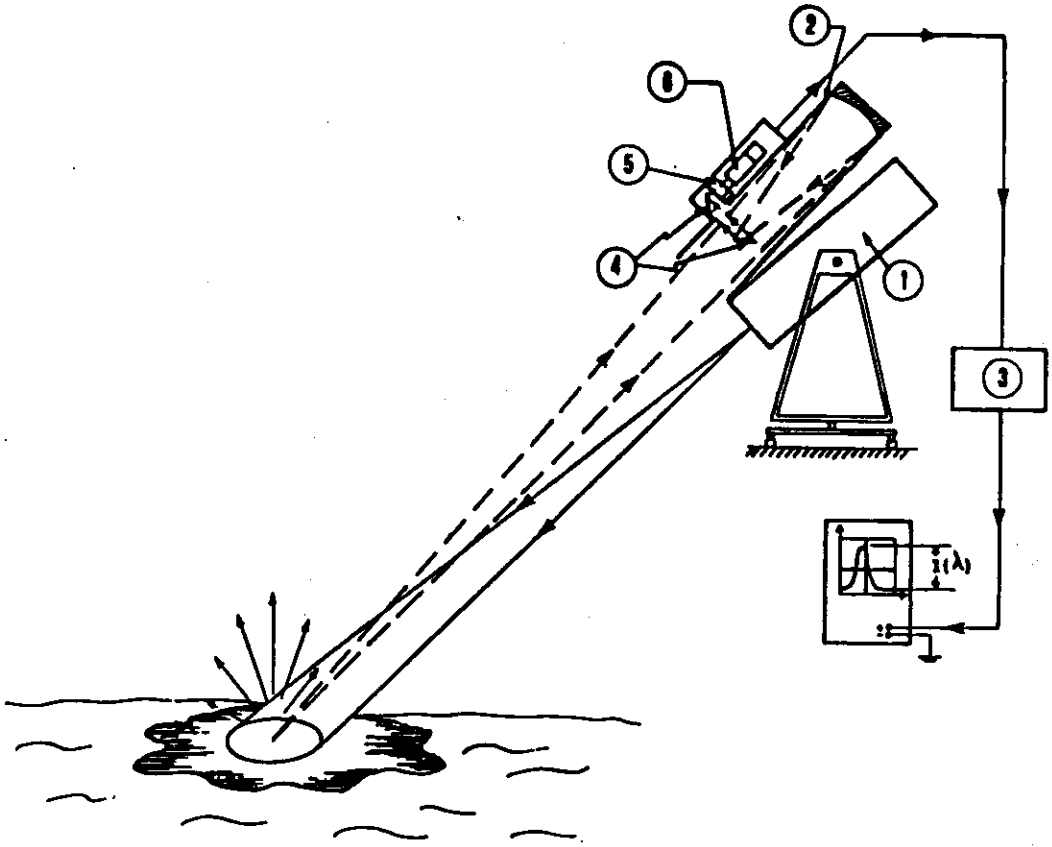
2
6
5
4
1
3
I(λ)

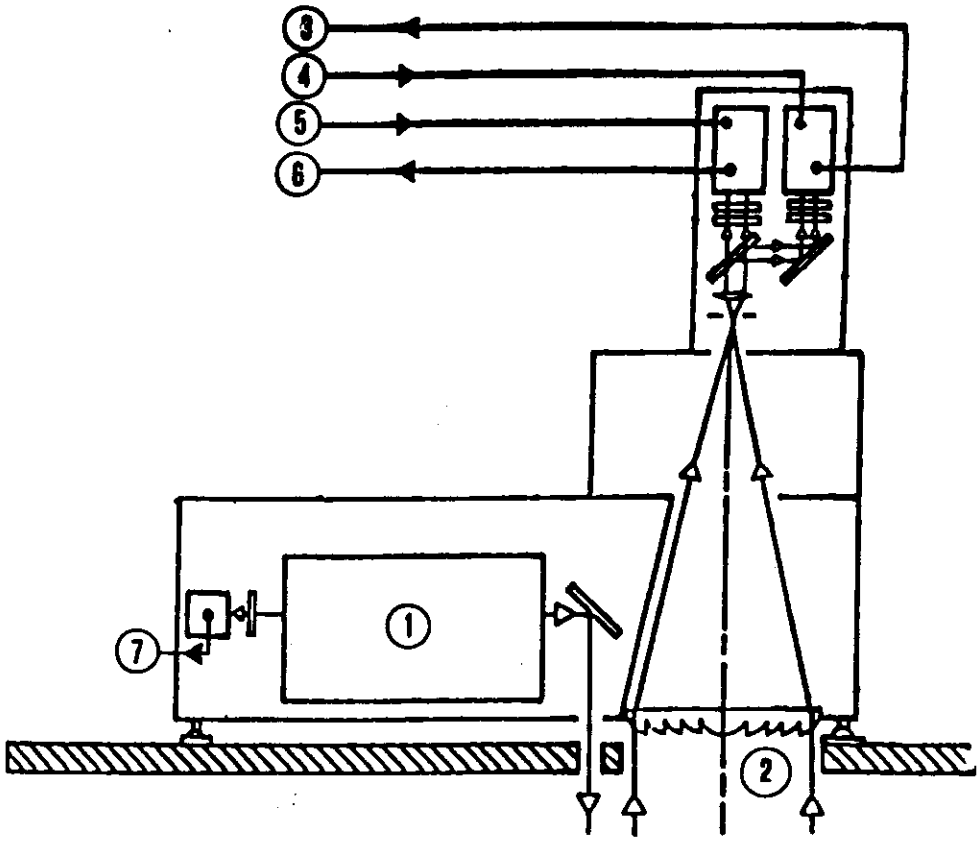
3
4
5
6
1
7
2

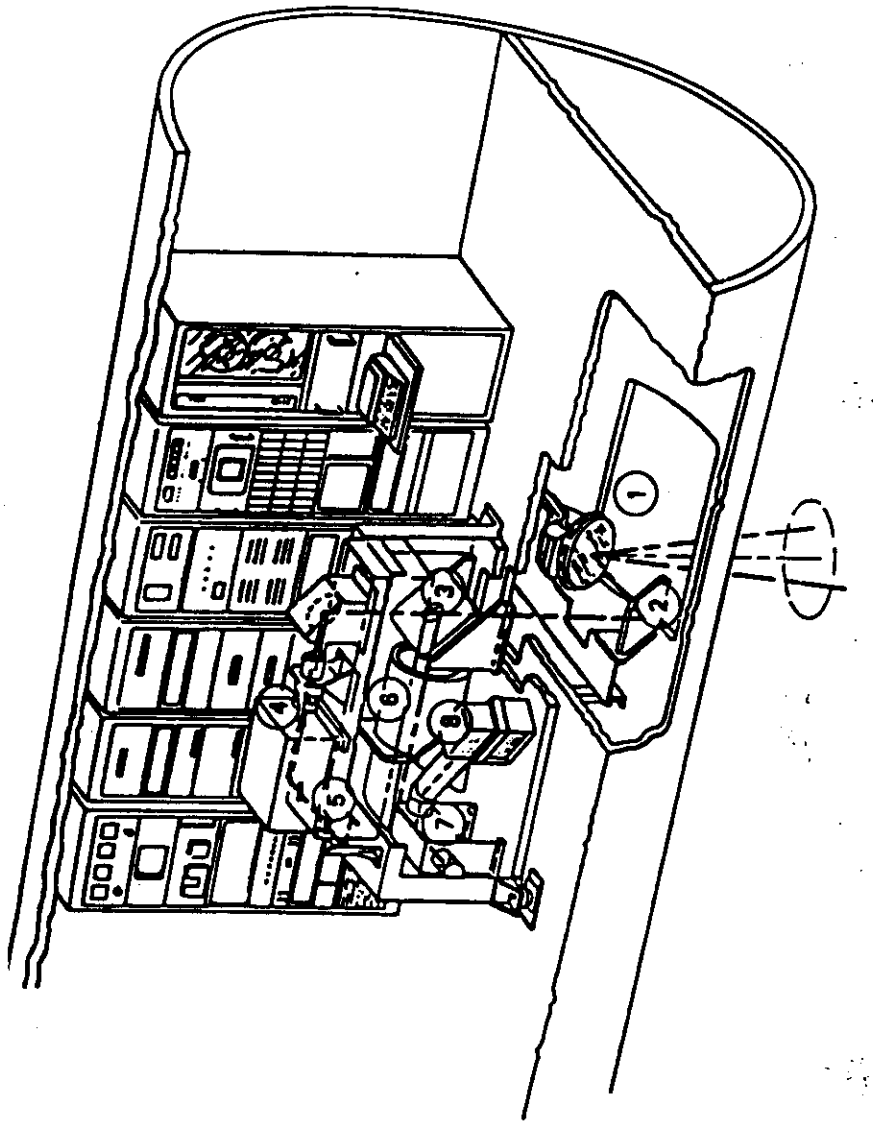

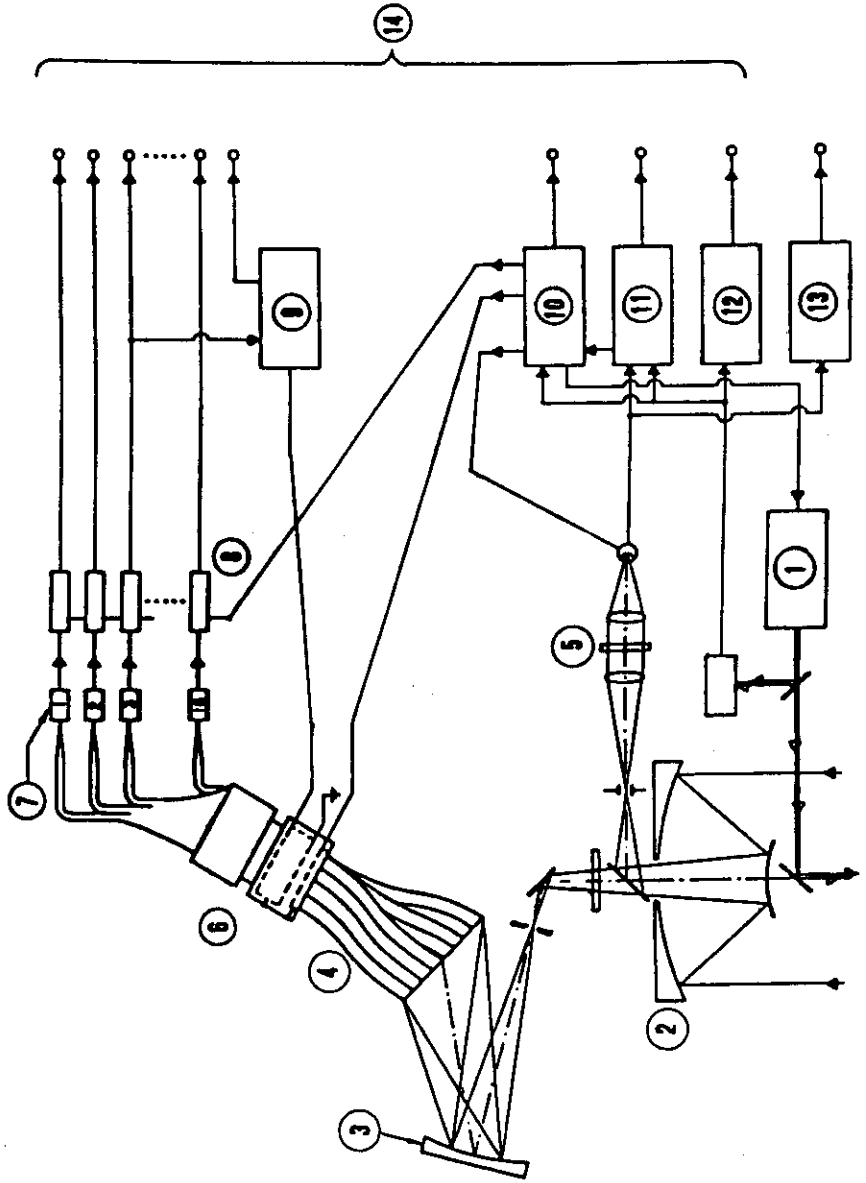
14
8
10
11
12
13
1
5
7
6
4
2
3

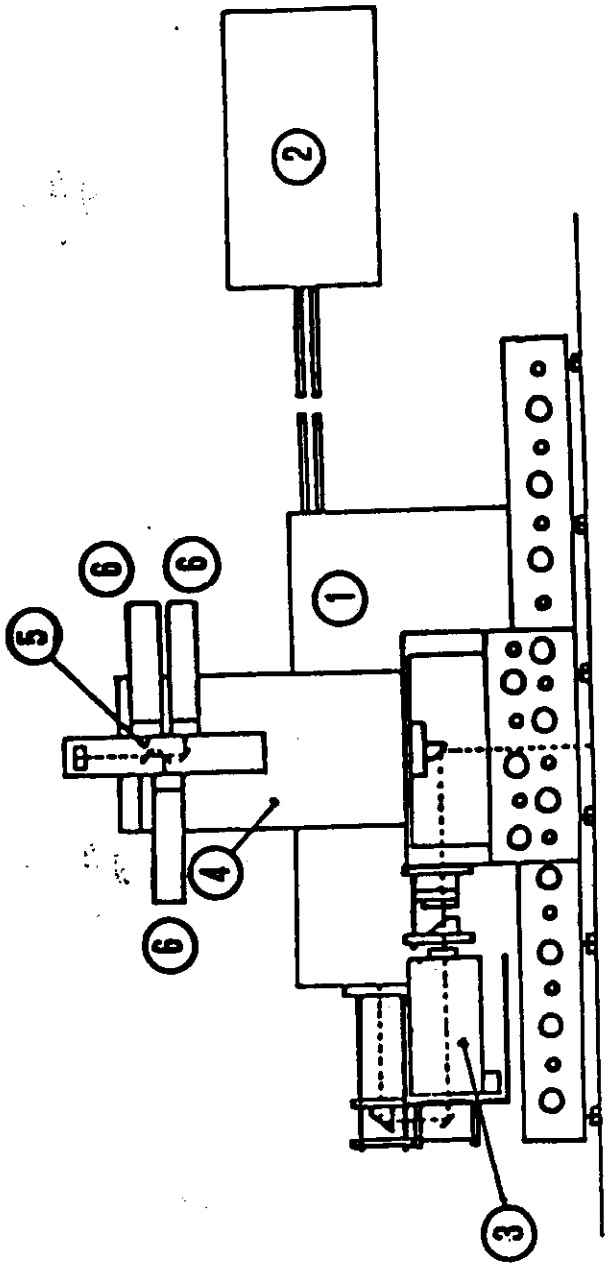

CONCEPTUAL LAYOUT OF THE LASER FLUOROSENSOR

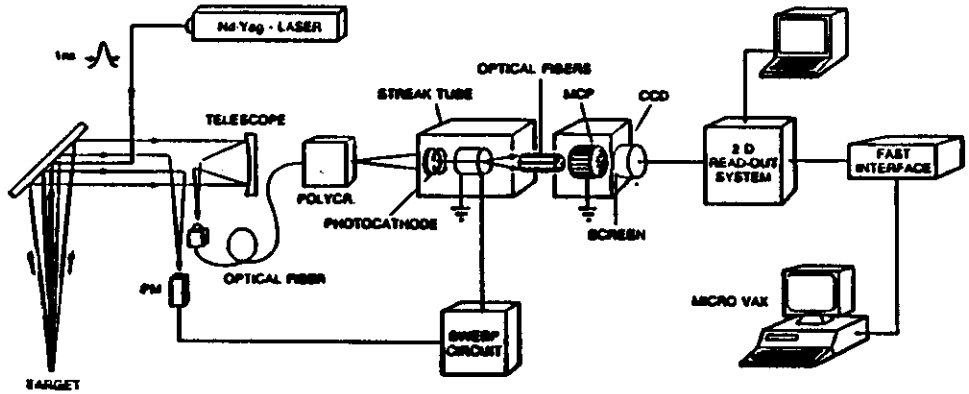

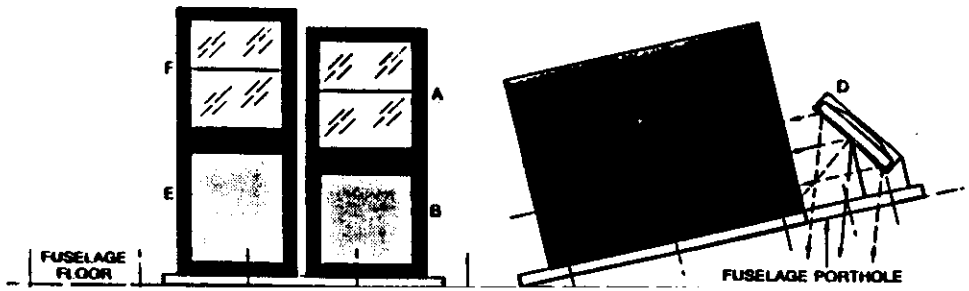

FLIDAR PROJECT

Development of a high resolution fluorescence Lidar for airborne, shipborne, and landbased detection of the largest possible set of environmental parameters.

System requirements

compactness – low power consumption – low weight
simultaneous detection of passive and active spectra

excitation wavelengths in the UV and in the VIS
multichannel detection

IROE-CNR

FLIDAR 2

LASER SOURCE	**Excimer (proprietary)** **Dye (proprietary)**	80 mJ @ 308 nm 7 mJ @ 480 nm
RECEIVER	**Telescope (SILO)**	Newton, 250 mm dia 1 m f.l., f/4
DISPERSIVE SYSTEM	**Spectrometer (Jarrell Ash)**	3 gratings, f/4
DETECTOR	**CCD array (EG&G PAR)**	512 channels, intensified, gateable
ACQUISITION & CONTROL	**OMA III (EG&G PAR)**	VME bus, 68000 up, 20 Mb HD

IROE-CNR

1
2
3
4
5
6

IROE FLIDAR 3

Designed and built for mobile–station remote sensing of sea and vegetation.

* Modular system
* Fiber optics coupling between the receiver and the detection system
* Lowered weight of the laser system
* Computer control of the whole measurement procedure
* Suitable software for interpreting data during measurement

IROE-CNR

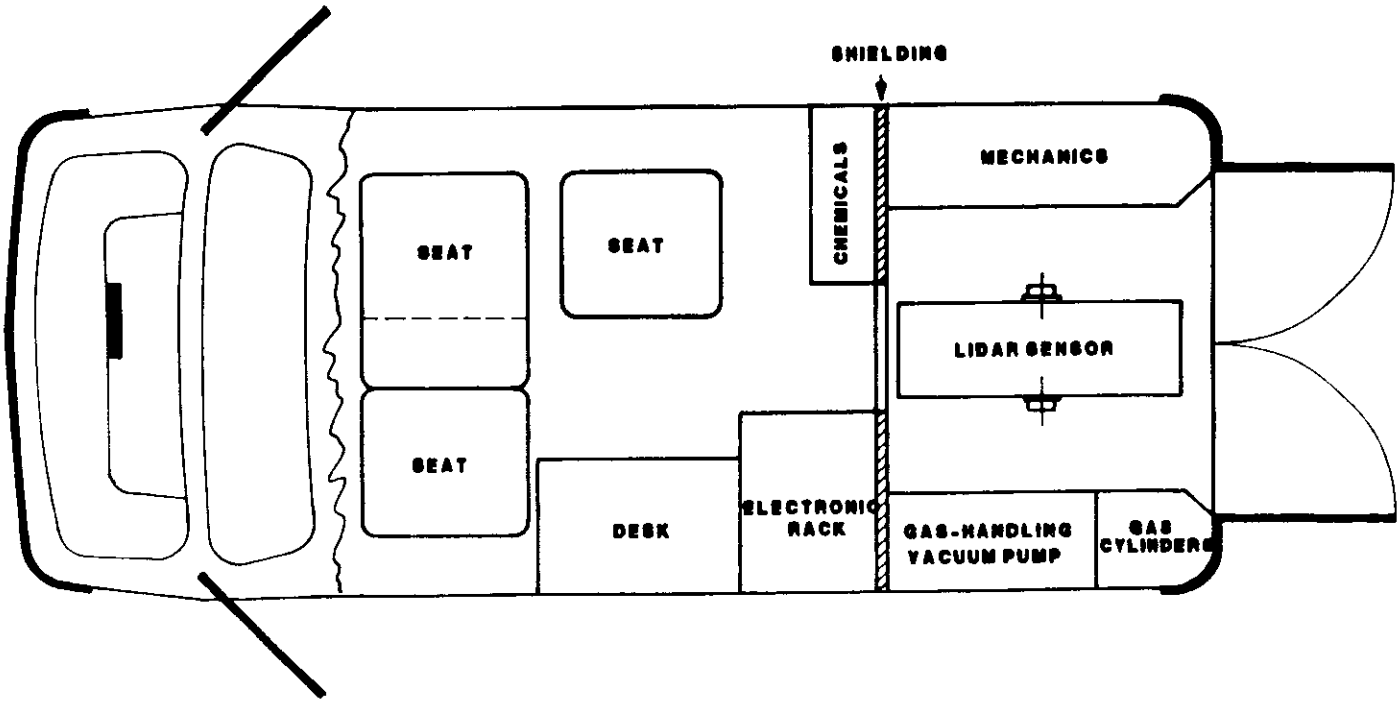

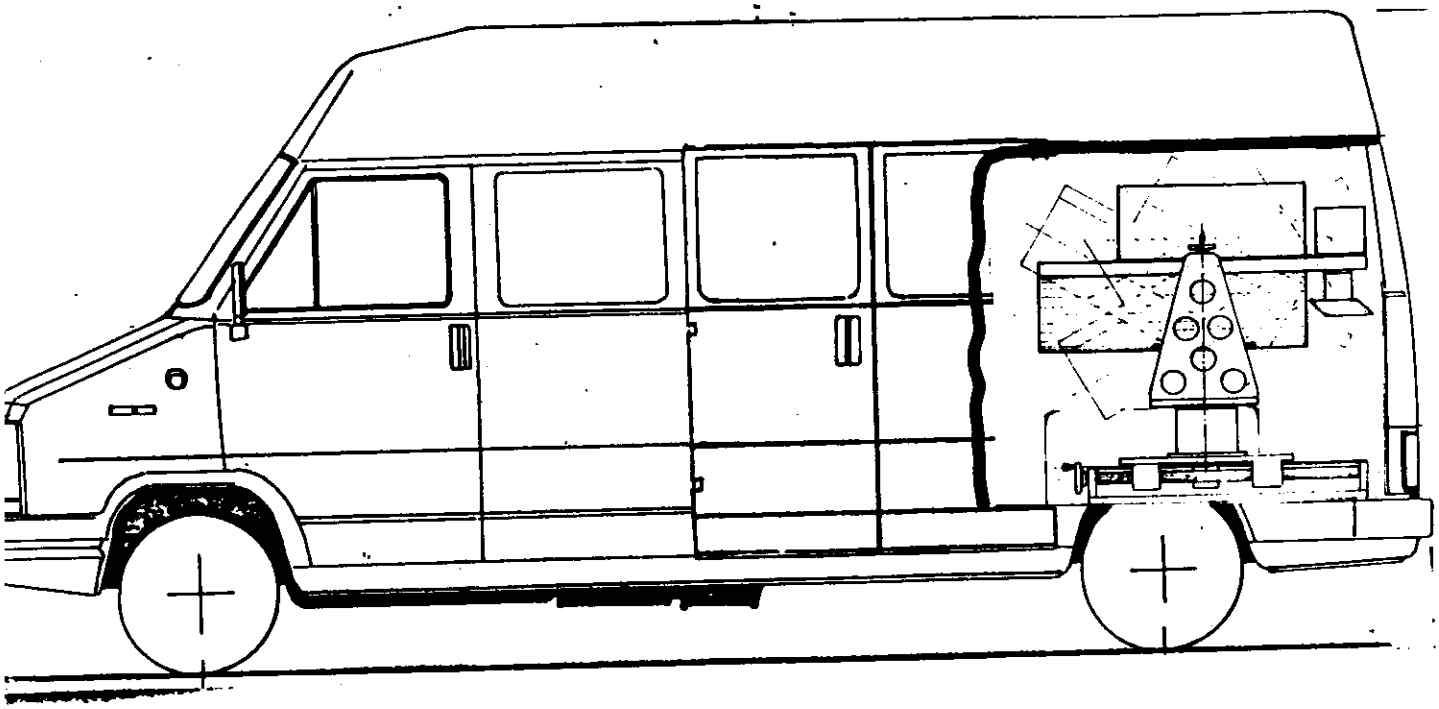

INSTITUTION	LASER	TELESCOPE	DETECTION	USE
Uni Toronto	N_2	unknown	PMT (1 chnl)	water pollution
NASA/WFC	N_2	30 cm	PMT (40 chnls)	water pollution vegetation
CCRS/Ottawa	N_2	20 cm	PD+int (16 chnls)	water pollution
OLS/Uni Oldenburg	XeCl+Dye	40 cm	PMT (7 chnls)	water pollution vegetation
IROE-CNR/Firenze	XeCl+Dye	25 cm	CCD-Array+inj. gate (512 chnls)	water pollution vegetation
CCR-ISPRA	Nd:Yag dupl.-tripl.	30 cm	Streak camera+ CCD (30 chnls)	water pollution vegetation

IROE-CNR

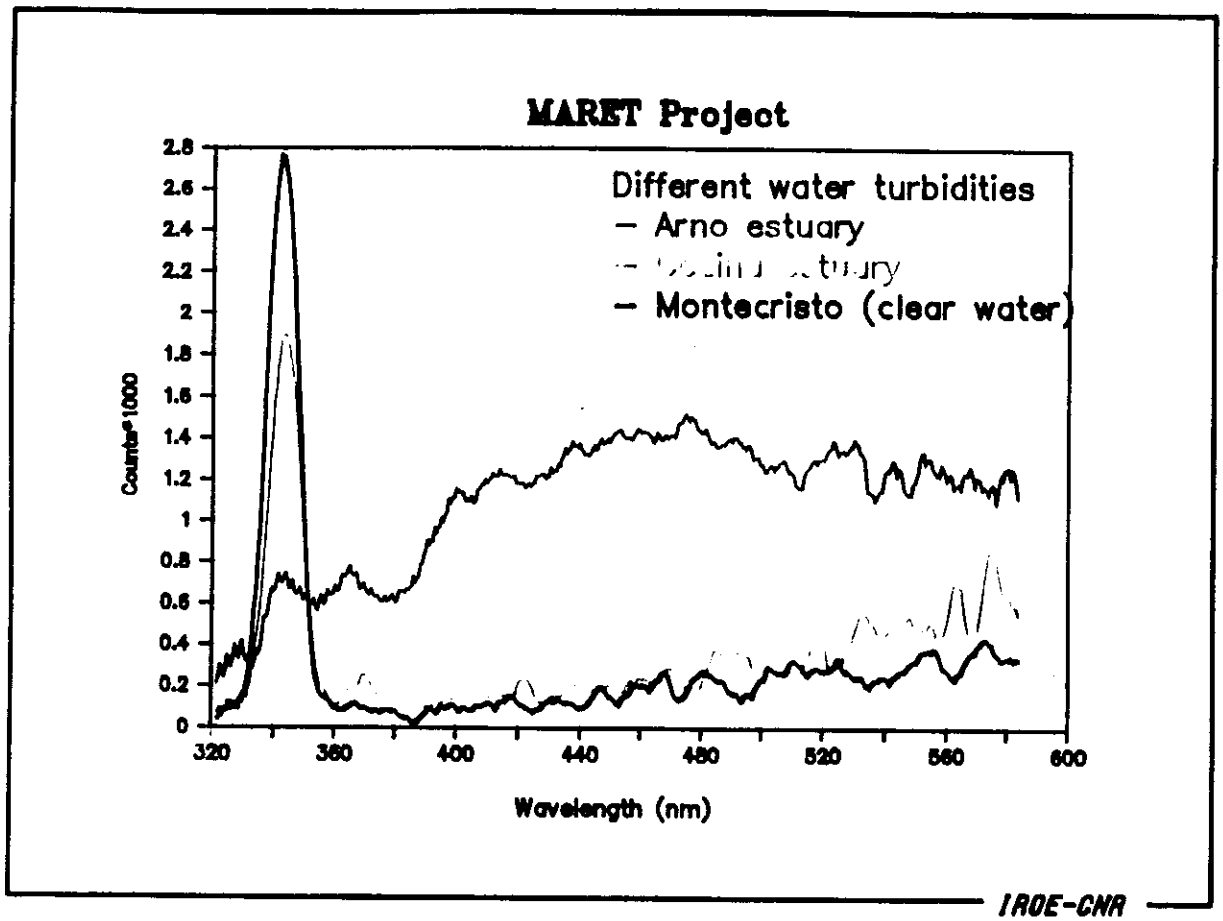
MARET Project
Different water turbidities
– Arno estuary
– Montecristo (clear water)
Counts*1000
Wavelength (nm)
IROE-CNR

67

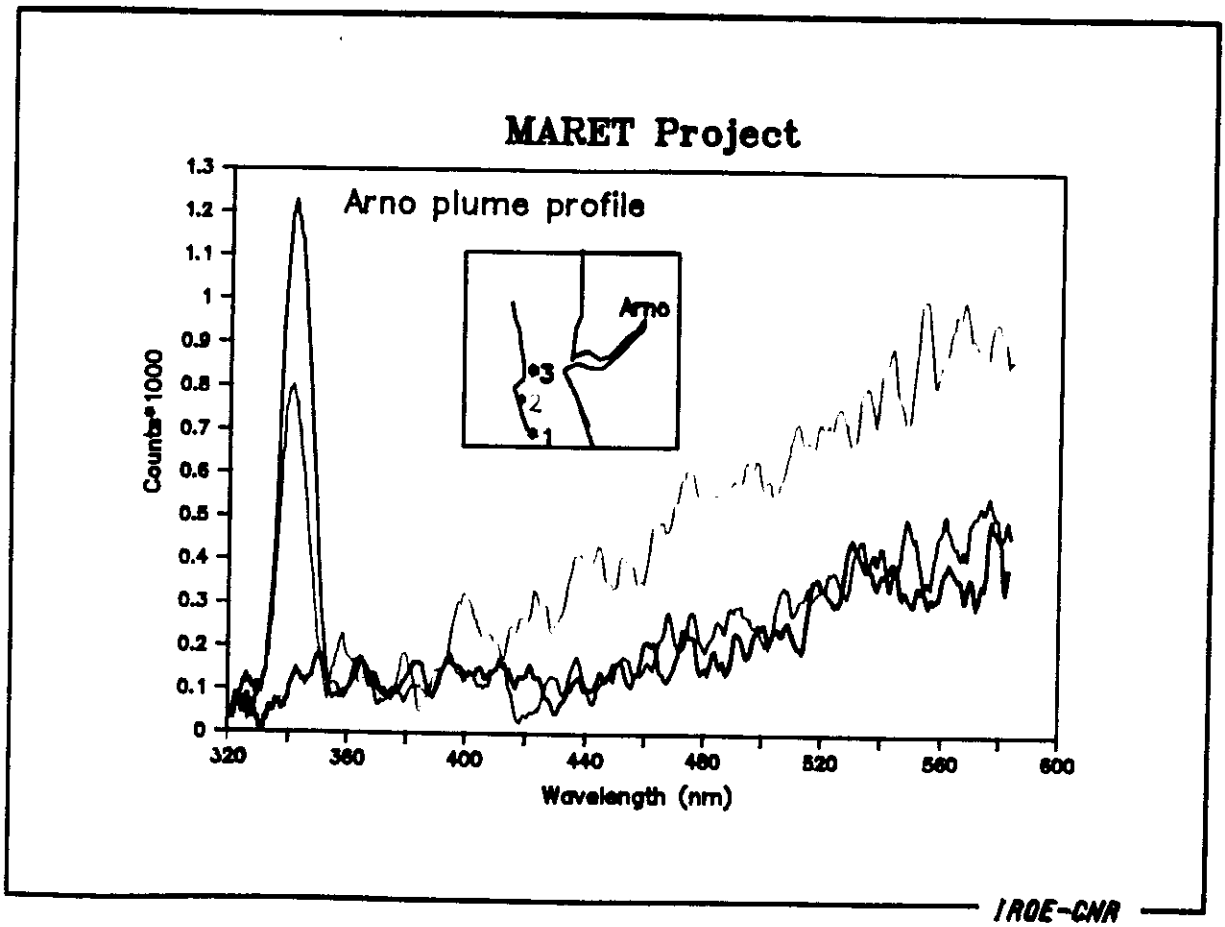
MARET Project
Arno plume profile
Arno
3
2
1
Counts*1000
Wavelength (nm)
IROE-CNR

68

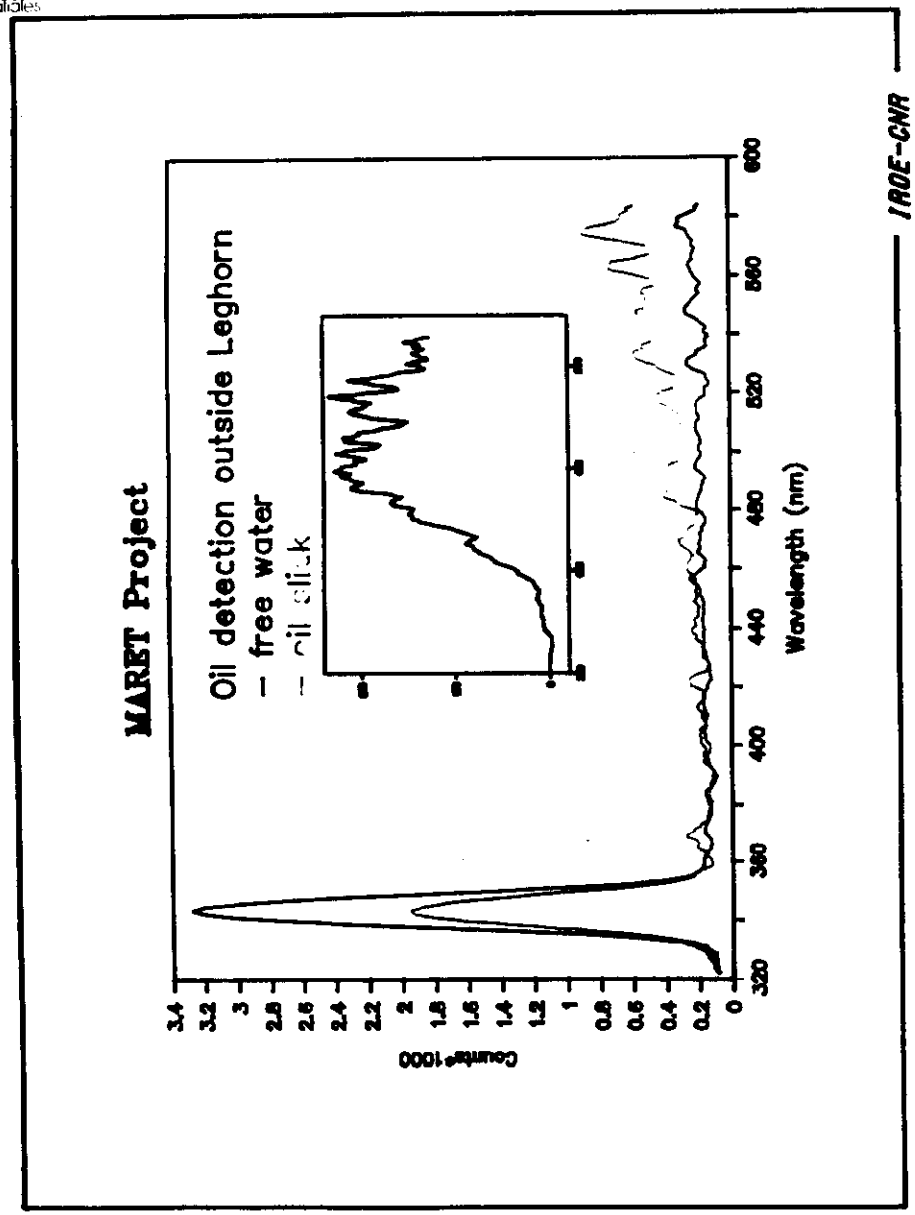

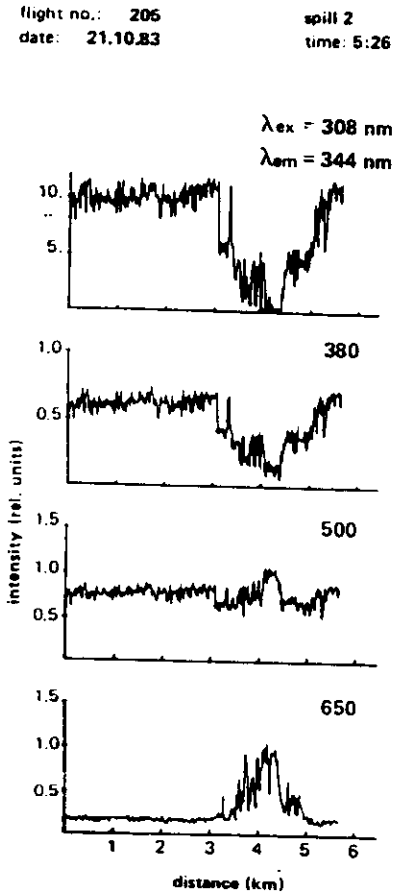

Figure 8.6 - Results obtained during flight n° 205, 21.10.83 5:26 h, over the fuel oil spill. Excitation wavelenghts 308 nm, emission wavelengths 344, 380, 500 and 650 nm.

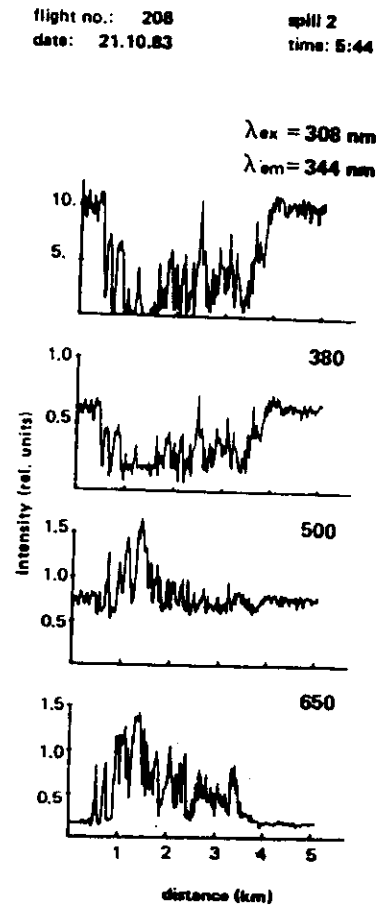

Figure 8.7 - Results obtained during fligh n° 208, 21.10.83 5:44 h, ove the fuel oil spill. Same excitation and emission wavelength as in Fig. 8.6.

two wavelengths analysis

excitation wavelength 337 nm

crude — light oils

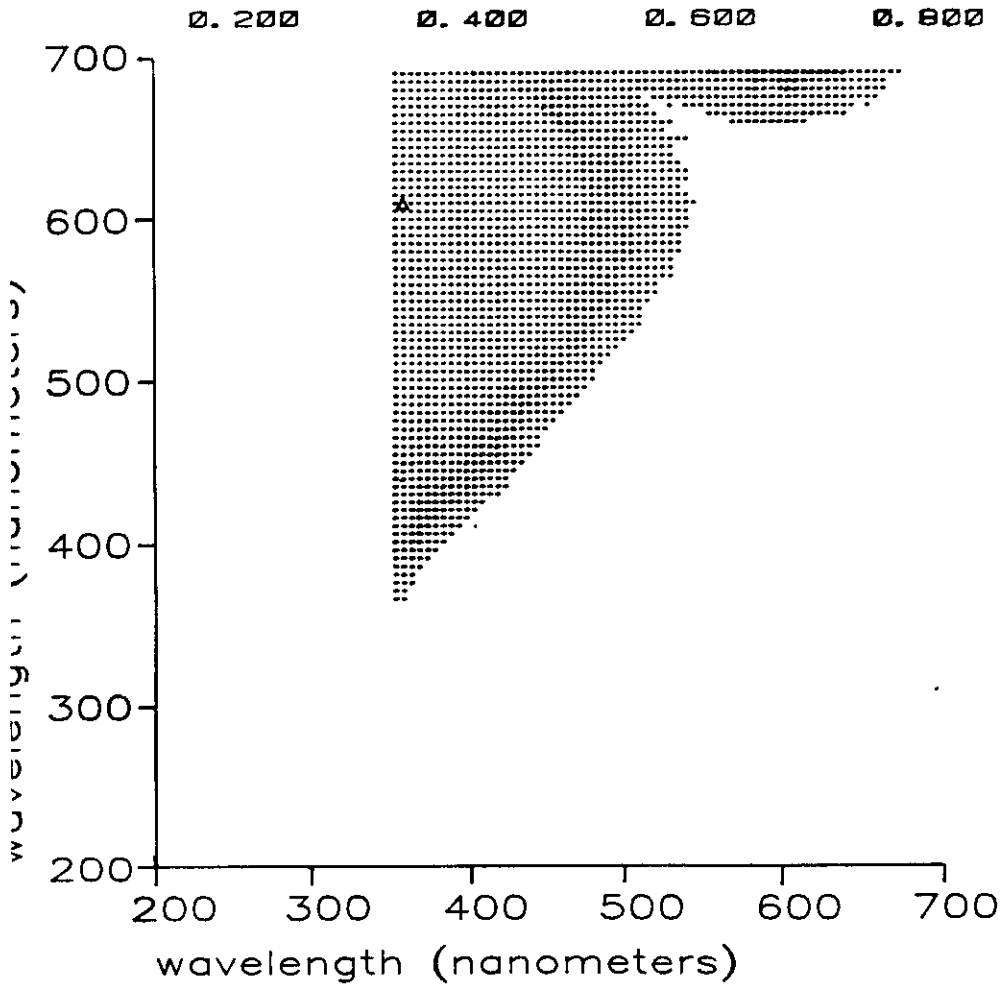

C.N.R. — I.R.O.E.

histogram of ratio $S(\lambda_1)/S(\lambda_2)$

where λ_1=690 nm , λ_2=375 nm

light crude heavy

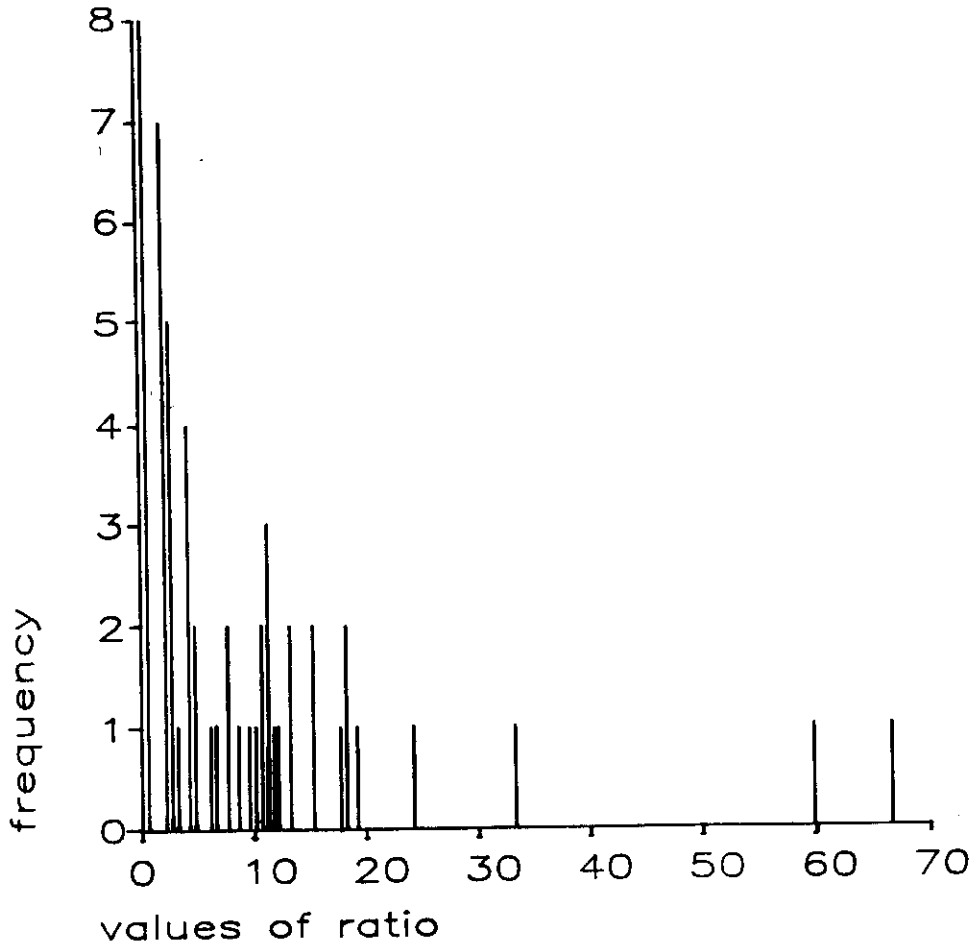

C.N.R. — I.R.O.E.

Example of measurement on the water column with 355 nm excitation

Spectro-temporal image showing the return signal intensity (color code) as a function of wavelength and time. From bottom to top the backscattering, Raman and gelbstoff fluorescence signals are clearly distinguished.

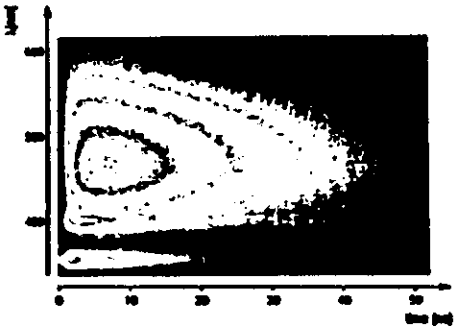

Spectrum of the detected light integrated on the entire time window. The peak at 355 nm is the backscattered UV light, the one at 404 nm the Raman diffusion and the broad spectrum the gelbstoff fluorescence.

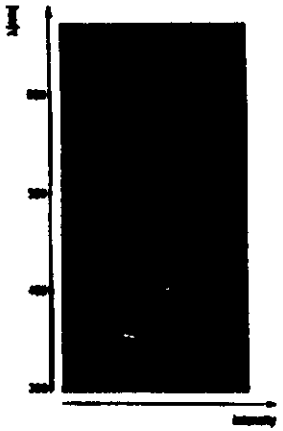

This measurement was realized on a 7 m high column of industrial tap water. The distance was 100 m and the signal was accumulated on 200 laser pulses.

The temporal behaviour of the gelbstoff fluorescence signal : the broad maximum is due to the convolution of the substance natural decay time with the time of flight of the photons emitted along the water column.

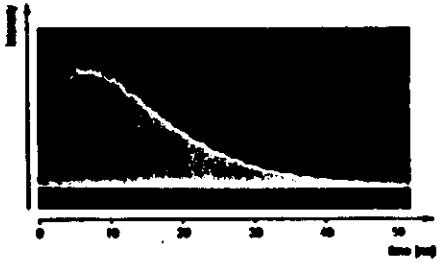

Temporal behaviour of the water Raman signal : the Raman signal decreases exponentially with a rate corresponding to the mean water extinction coefficient at 355 nm and 404 nm.

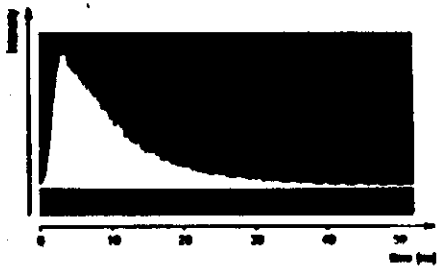

Temporal behaviour of the elastically backscattered light : it decreases with a rate corresponding to the water extinction coefficient at 355 nm.

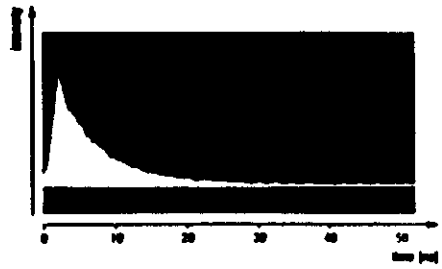

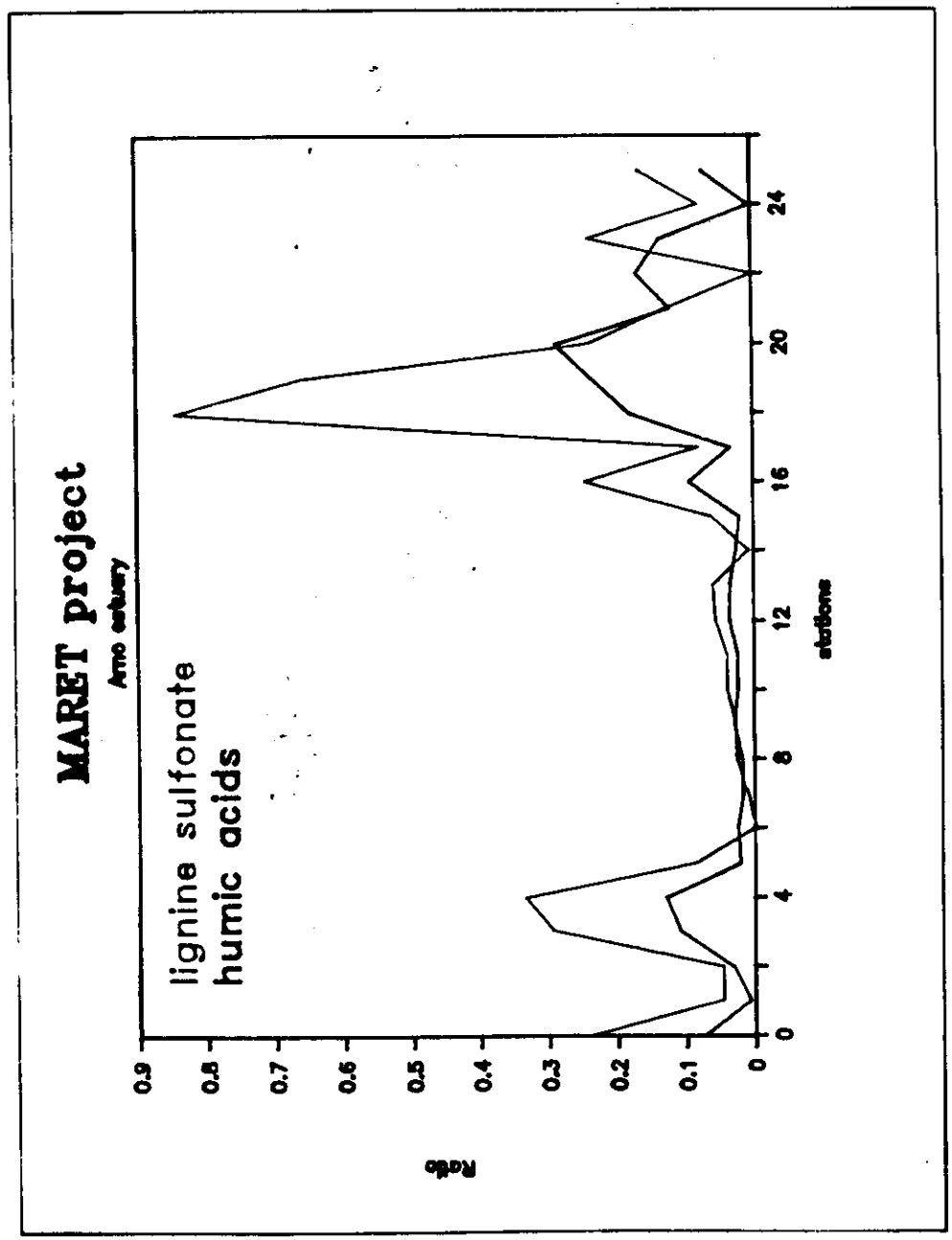

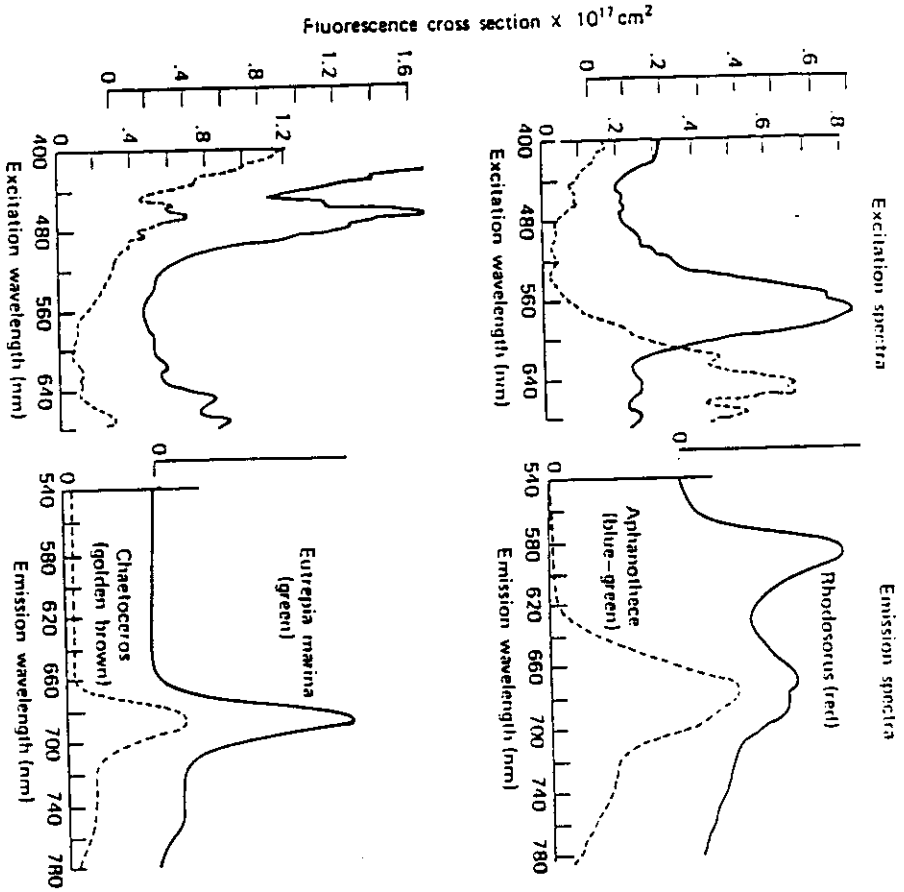

VEGETATION: LABORATORY STUDIES

* chlorophyll fluorescence spectra, taken in vivo →
  possible connection with photosynthetic activity →
  PAR measurement needed

* excitation wavelength optimization (480 nm, 630 nm)

* remote detection with a single shot (10 mJ)

* complementary parameters are extracted
  from passive spectra

IROE-CNR

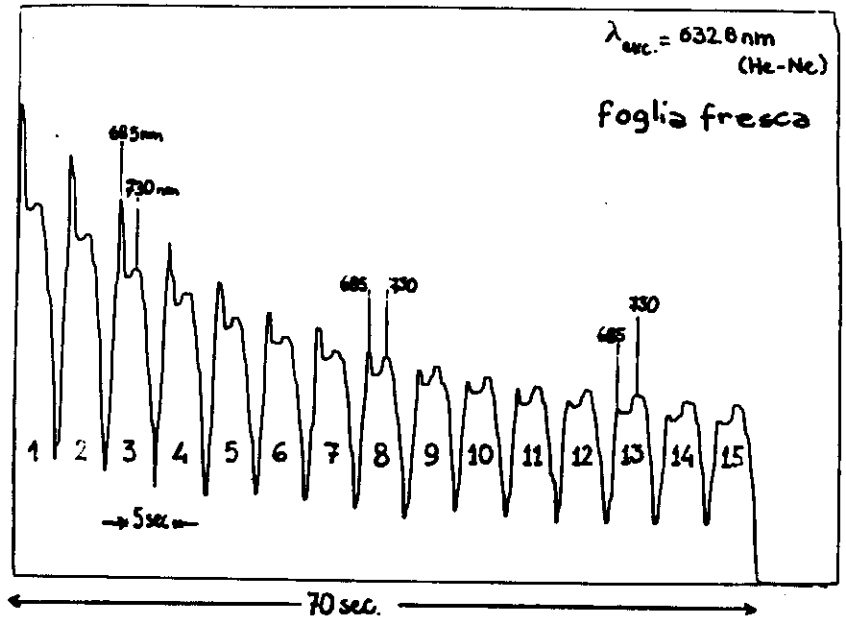
λexc.= 632.8nm
(He-Ne)
foglia fresca
685nm
730nm
685
730
685
730
1 2 3 4 5 6 7 8 9 10 11 12 13 14 15
5sec
70 sec.

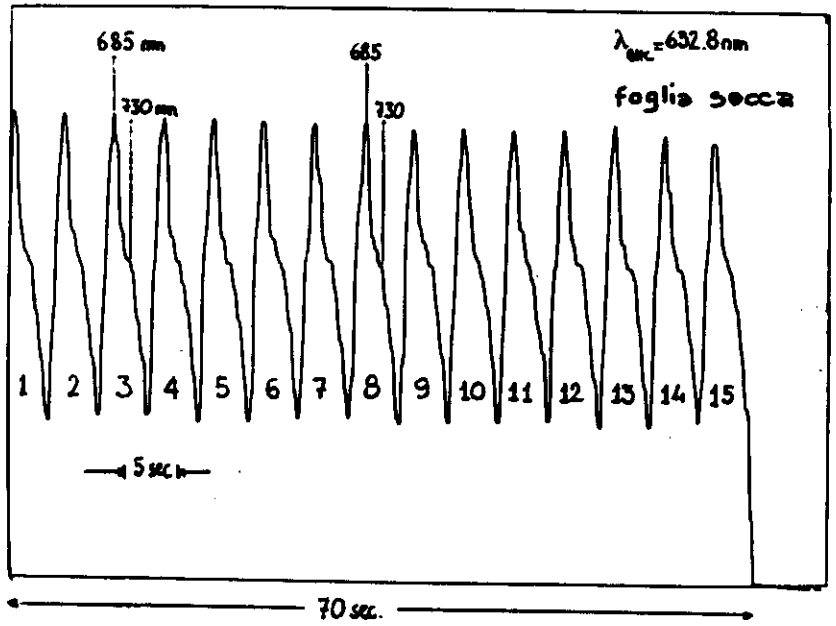
685 nm
730nm
685
730
λexc=632.8nm
foglia secca
1 2 3 4 5 6 7 8 9 10 11 12 13 14 15
5sec
70 sec.

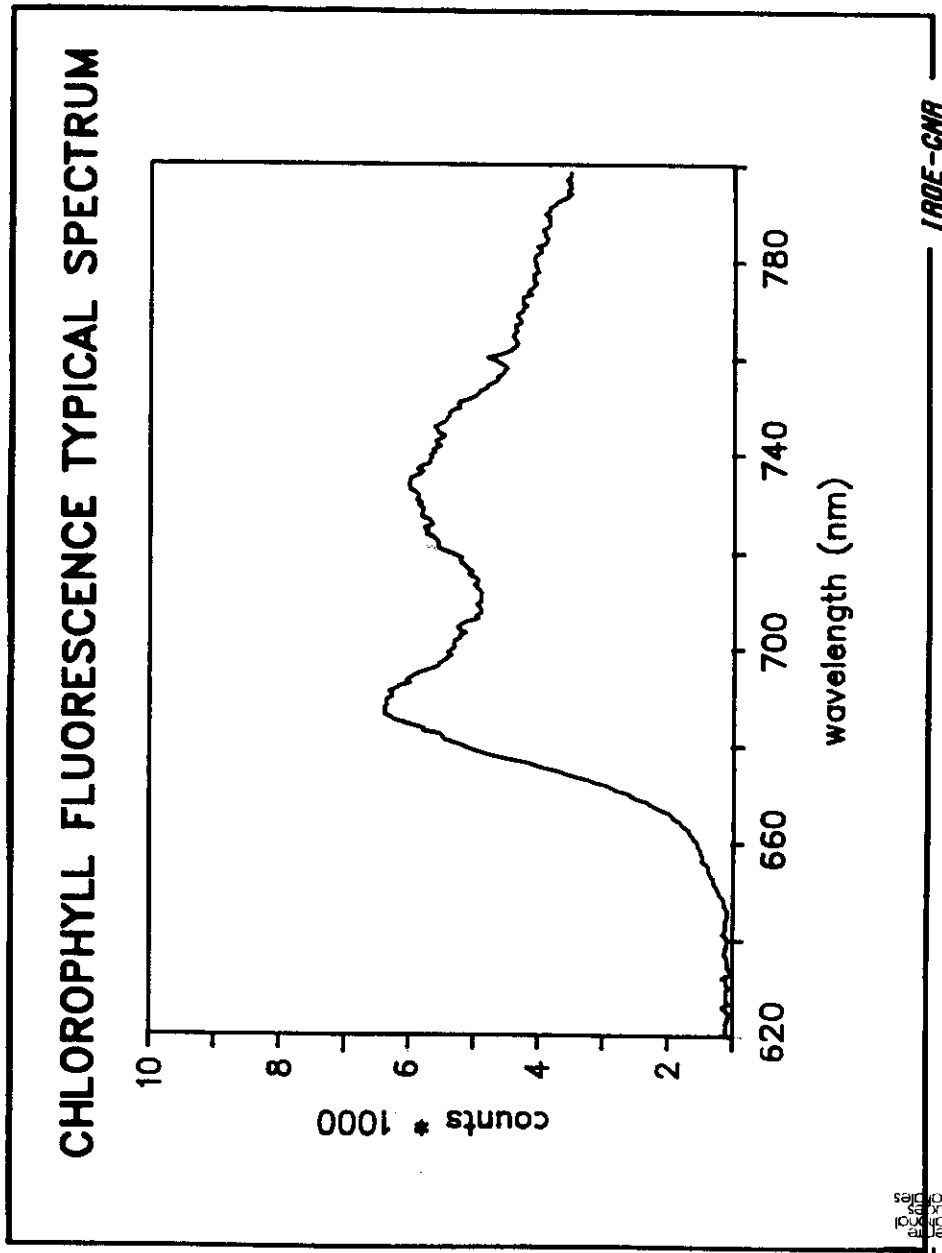
CHLOROPHYLL FLUORESCENCE TYPICAL SPECTRUM
counts * 1000
10
8
6
4
2
620
660
700
740
780
wavelength (nm)
IROE-CNR
Centro Nazionale Ricerche

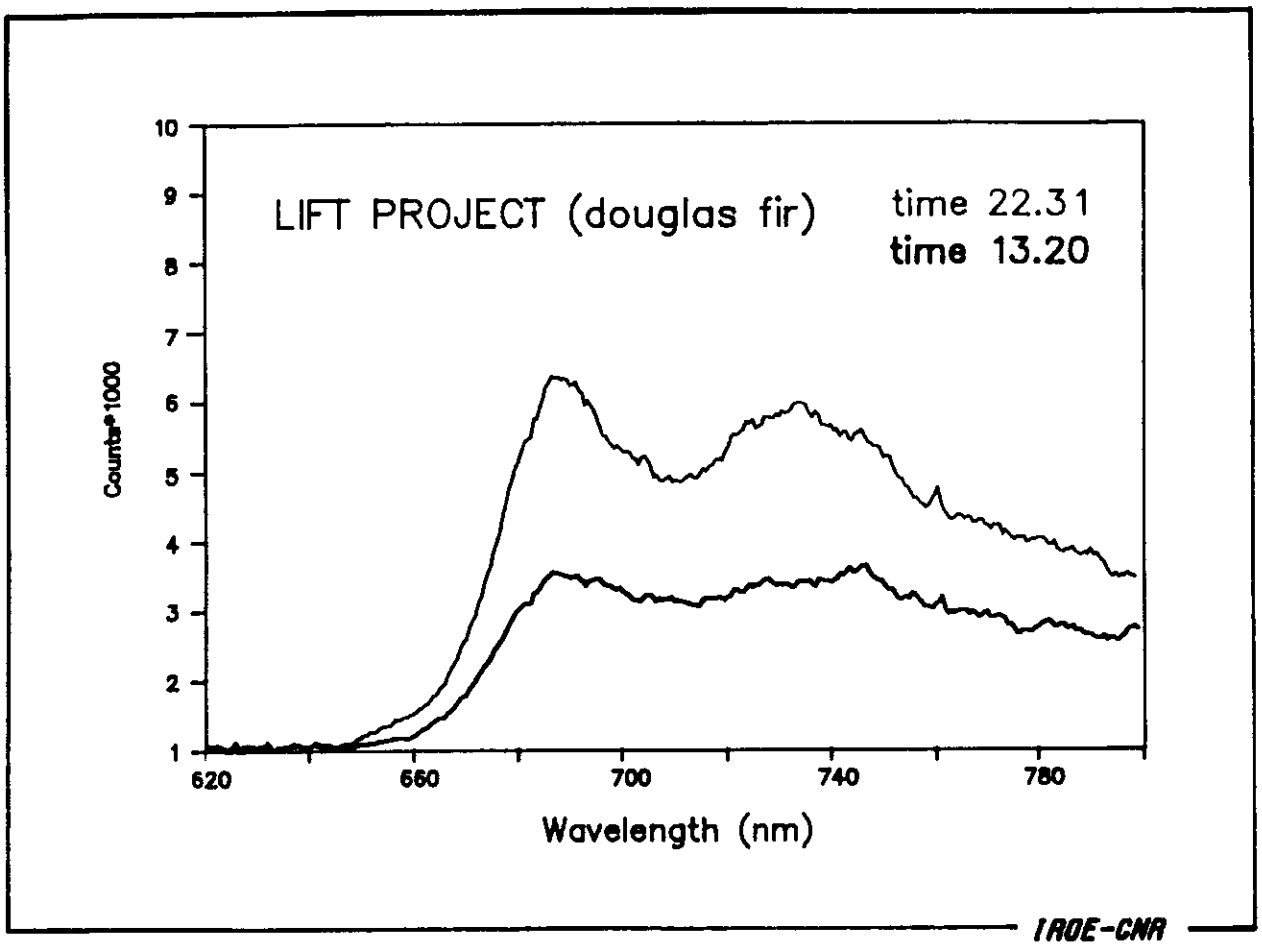
LIFT PROJECT (douglas fir)
time 22.31
time 13.20
Counts*1000
10
9
8
7
6
5
4
3
2
1
620
660
700
740
780
Wavelength (nm)
IROE-CNR

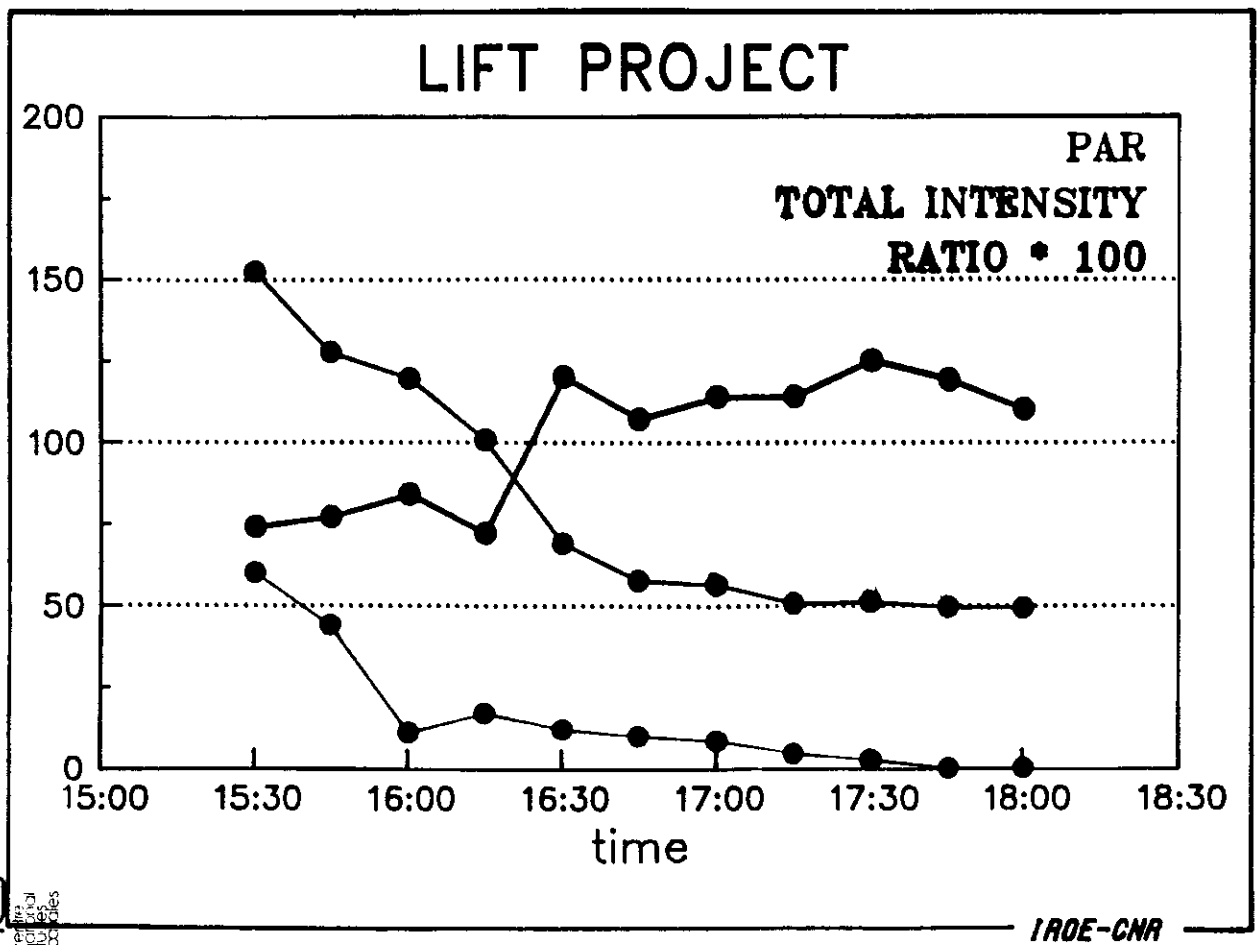
LIFT PROJECT
PAR
TOTAL INTENSITY
RATIO * 100
200
150
100
50
0
15:00
15:30
16:00
16:30
17:00
17:30
18:00
18:30
time
IROE-CNR

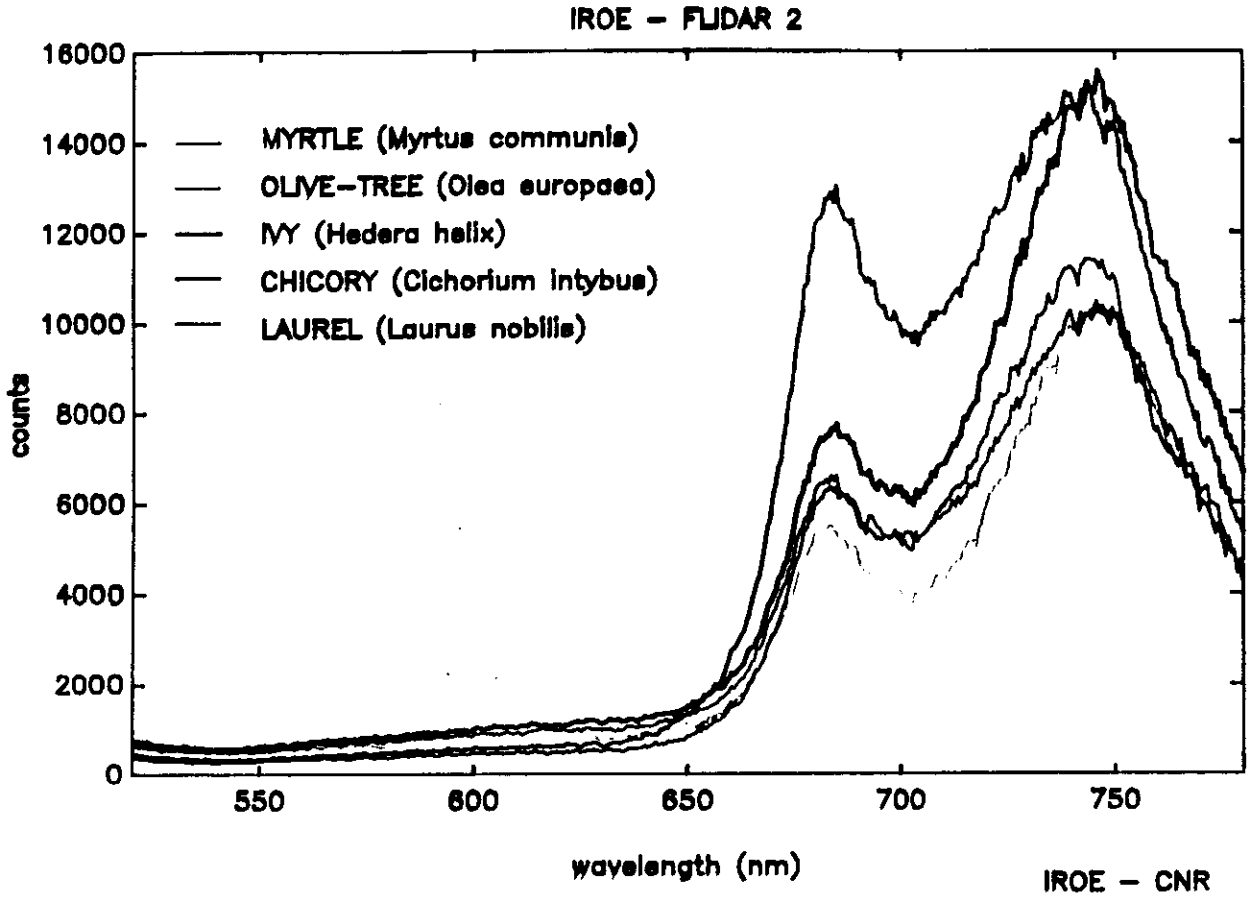
IROE – FLIDAR 2
MYRTLE (Myrtus communis)
OLIVE-TREE (Olea europaea)
IVY (Hedera helix)
CHICORY (Cichorium intybus)
LAUREL (Laurus nobilis)
counts
wavelength (nm)
IROE – CNR

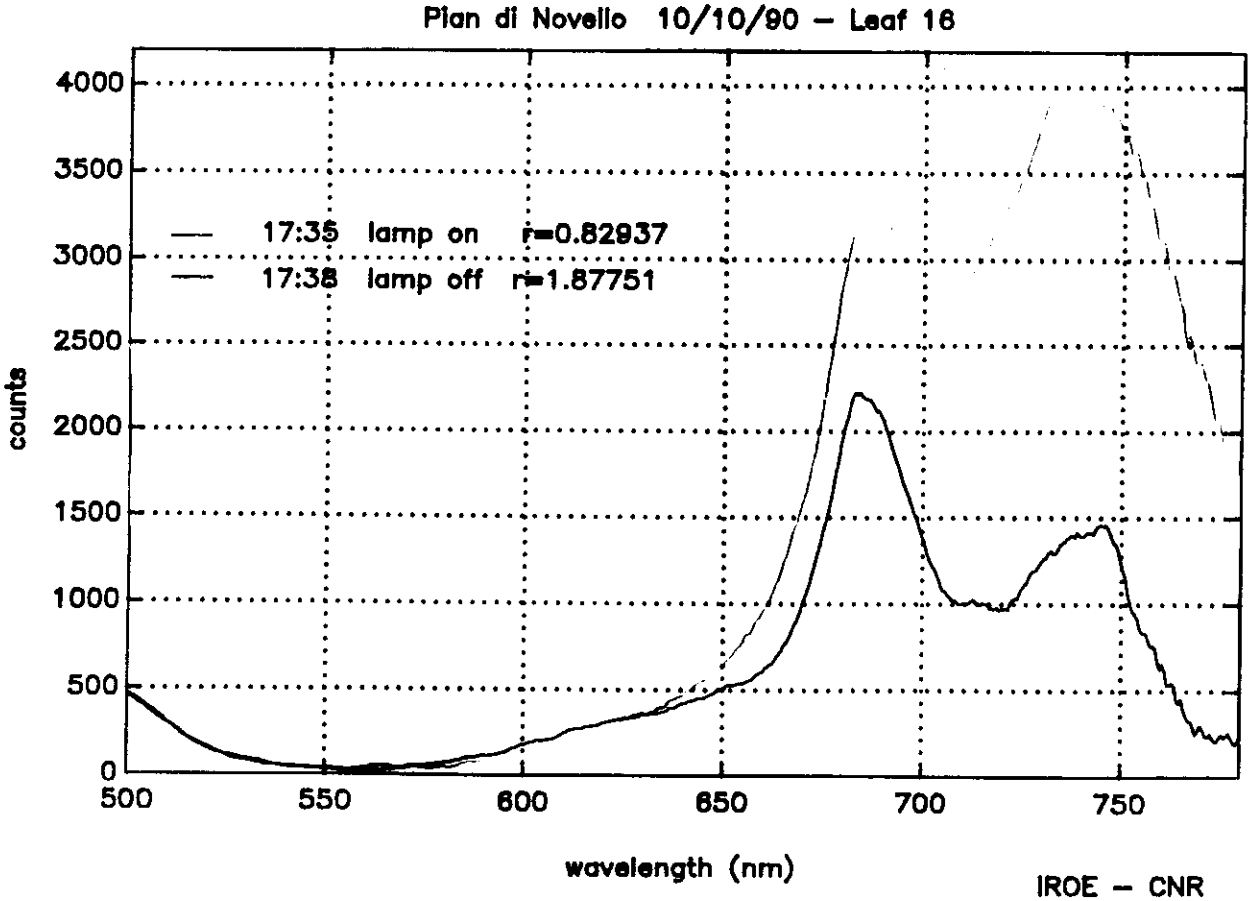
Pian di Novello 10/10/90 – Leaf 16
17:35 lamp on r=0.82937
17:38 lamp off r=1.87751
counts
wavelength (nm)
IROE – CNR

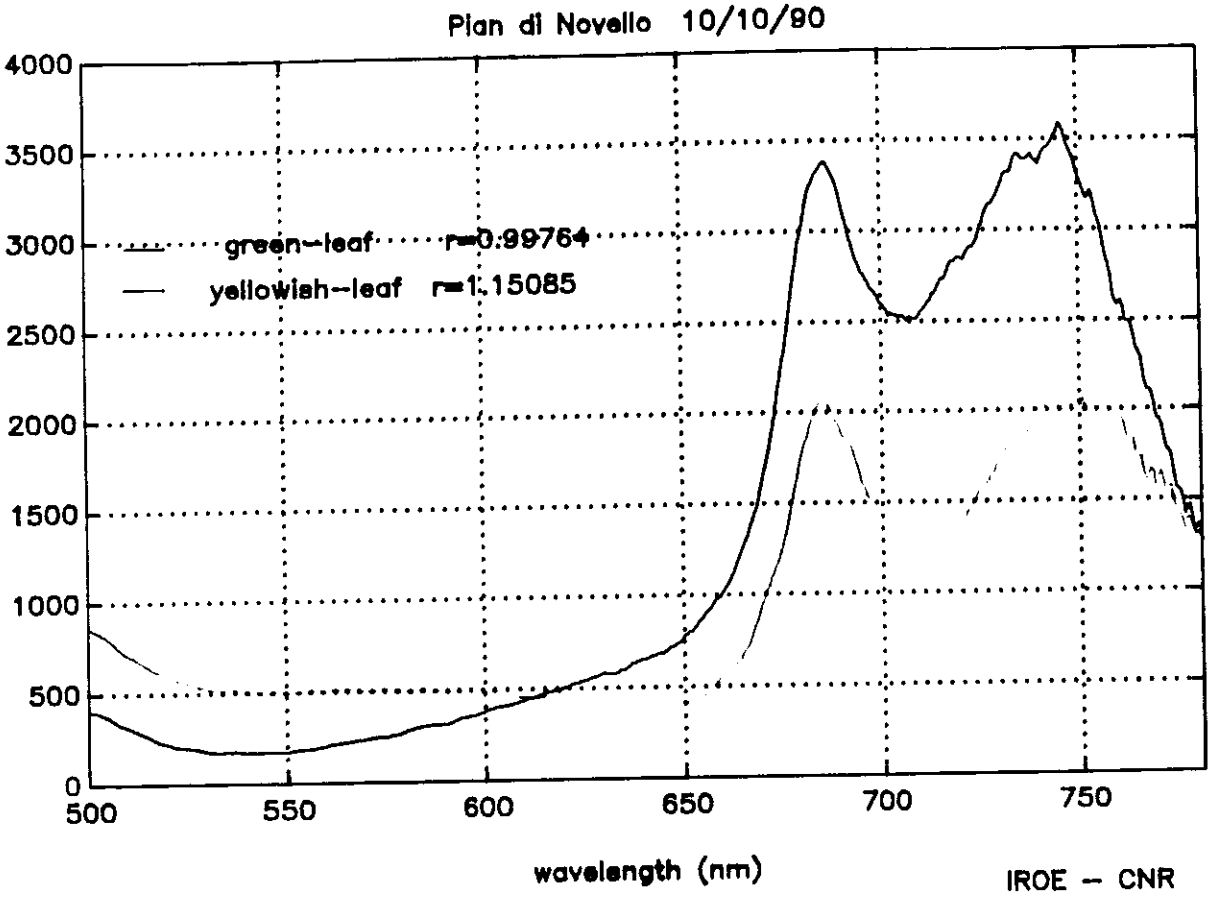
Pian di Novello 10/10/90
green-leaf r=0.99764
yellowish-leaf r=1.15085
4000
3500
3000
2500
2000
1500
1000
500
0
500
550
600
650
700
750
wavelength (nm)
IROE – CNR

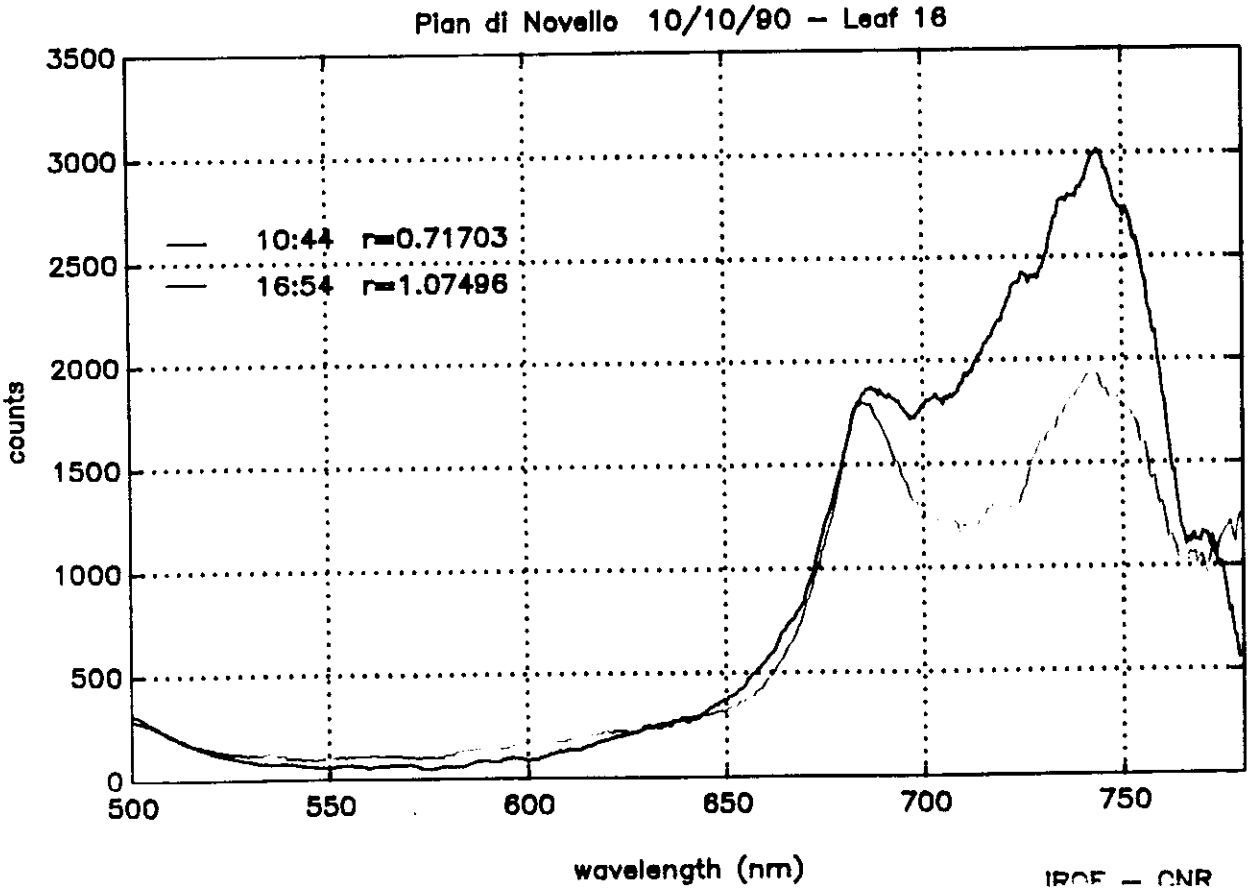
Pian di Novello 10/10/90 – Leaf 16
10:44 r=0.71703
16:54 r=1.07496
counts
3500
3000
2500
2000
1500
1000
500
0
500
550
600
650
700
750
wavelength (nm)
IROE – CNR

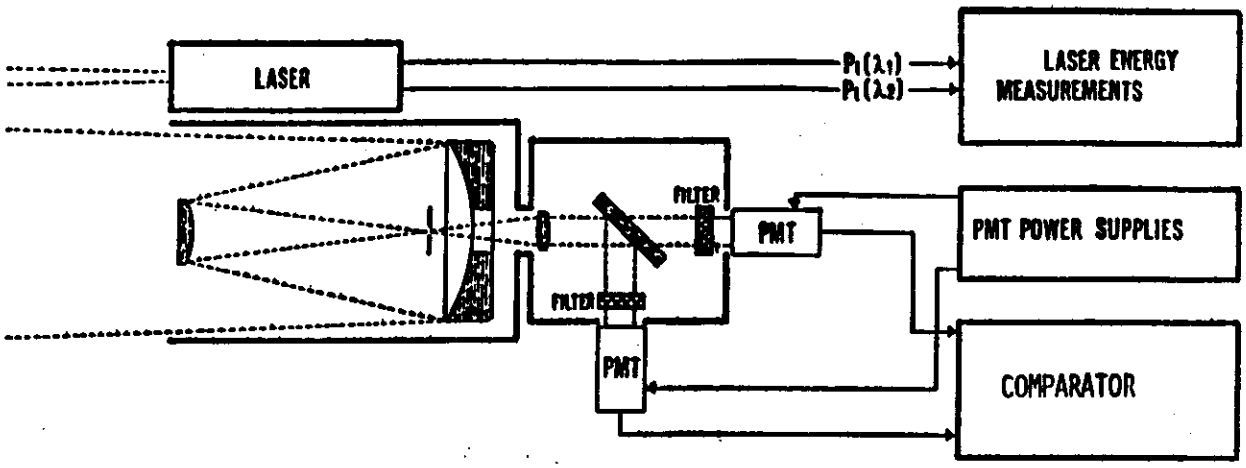

DIFFERENTIAL REFLECTANCE LIDAR.

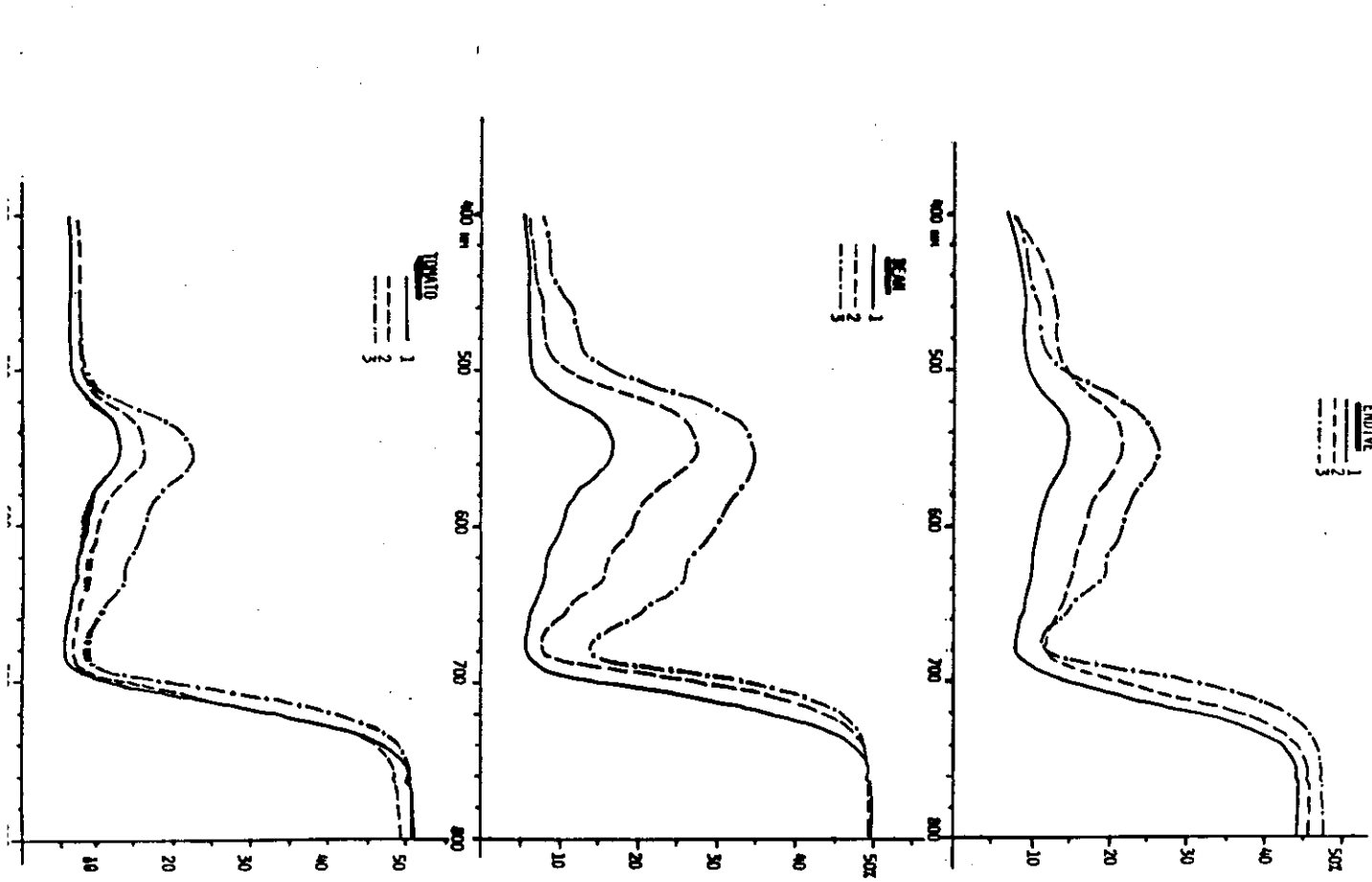

VEGETABLE		740/560	740/600	740/680	740/700	760/700
ENDIVE	1	2.9	3.8	5.3	3.0	3.2
	2	2.1	2.6	4.0	2.0	2.1
	3	1.8	2.1	4.2	1.4	1.5
BEAN	1	2.9	4.5	7.8	3.1	3.3
	2	1.8	2.5	6.1	2.0	2.0
	3	1.4	1.6	3.5	1.5	1.5
TOMATO	1	4.1	6.2	10.0	3.9	3.9
	2	3.0	4.8	7.4	3.0	3.0
	3	2.3	3.6	5.8	2.3	2.3

SPECTRAL REFLECTANCE RATIO OF VEGETABLE LEAVES IN DIFFERENT SENESCENCE STATE. THE SENESCENCE INCREASES WITH THE NUMBER

OLIVE TREE DISEASE	740/550	740/600	740/680	740/700	760/700	760/720
REFERENCE	7.0	8.0	8.9	5.3	5.8	1.8
FUMAGINE	4.8	5.4	5.7	3.9	4.4	1.9
REFERENCE	4.8	6.8	8.2	4.5	5	=
CYCLOCONIUM 1	3.6	5.2	8.8	3.1	3.3	=
2	2.4	2.9	6.1	2.0	2.1	=

SPECTRAL REFLECTANCES OF OLIVE TREE LEAVES WITH DIFFERENT DISEASE THE DATA FOR CYCLOCONIUM WERE EXTRACTED FROM: BALDY & TRIGUI, SYMP. SIGNATURES SPECTRALES D'OBJET EN TELEDETECTION, BORDEAUX, SEPT.1983

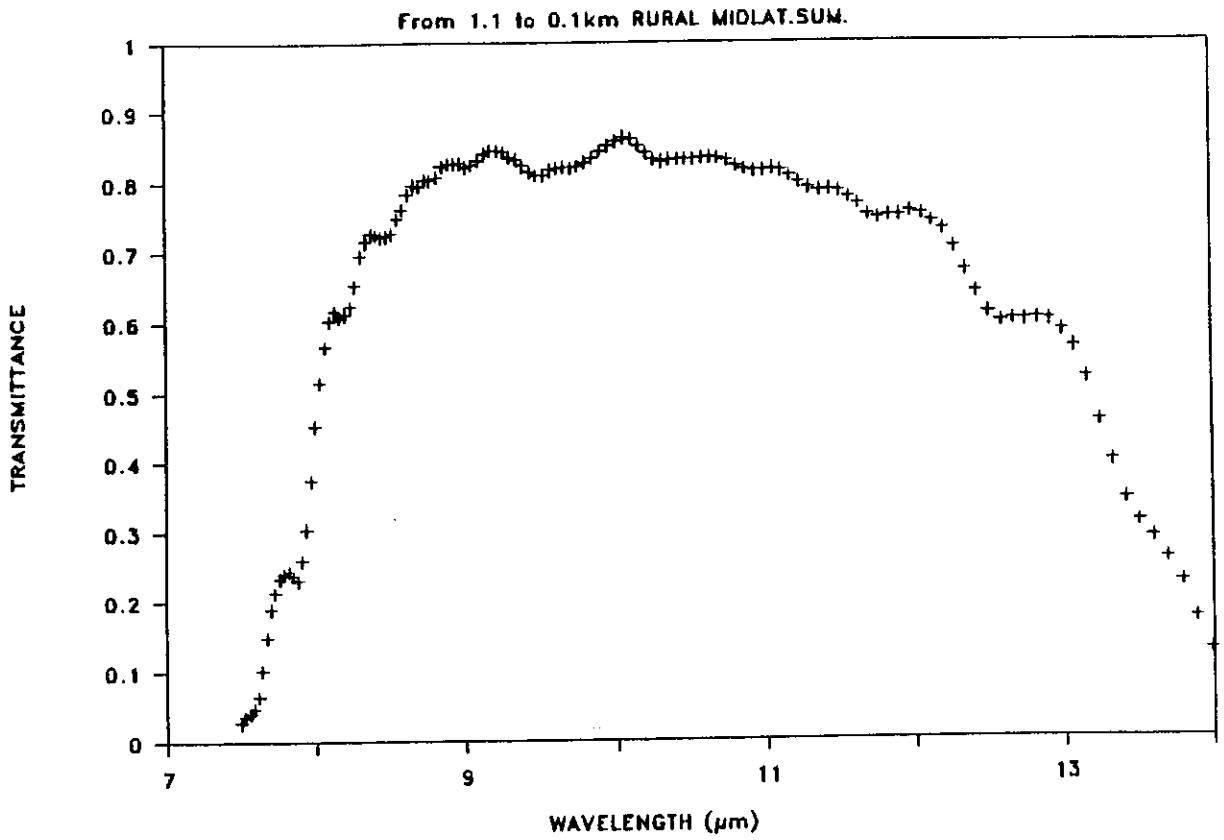
LOWTRAN 7
From 1.1 to 0.1km RURAL MIDLAT.SUM.
TRANSMITTANCE
1
0.9
0.8
0.7
0.6
0.5
0.4
0.3
0.2
0.1
0
7
9
11
13
WAVELENGTH (μm)

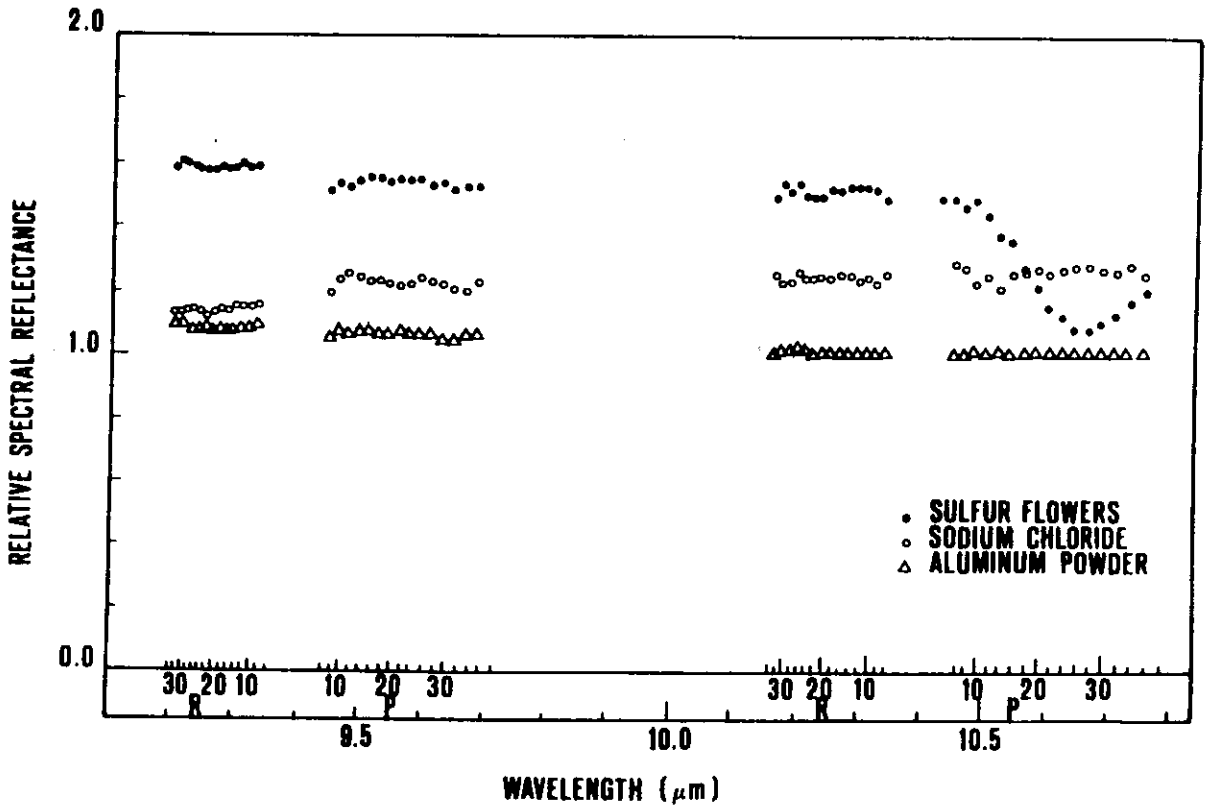
RELATIVE SPECTRAL REFLECTANCE
2.0
1.0
0.0
SULFUR FLOWERS
SODIUM CHLORIDE
ALUMINUM POWDER
30 20 10
R
10 20 30
P
30 20 10
R
10 20 30
P
9.5
10.0
10.5
WAVELENGTH (μm)

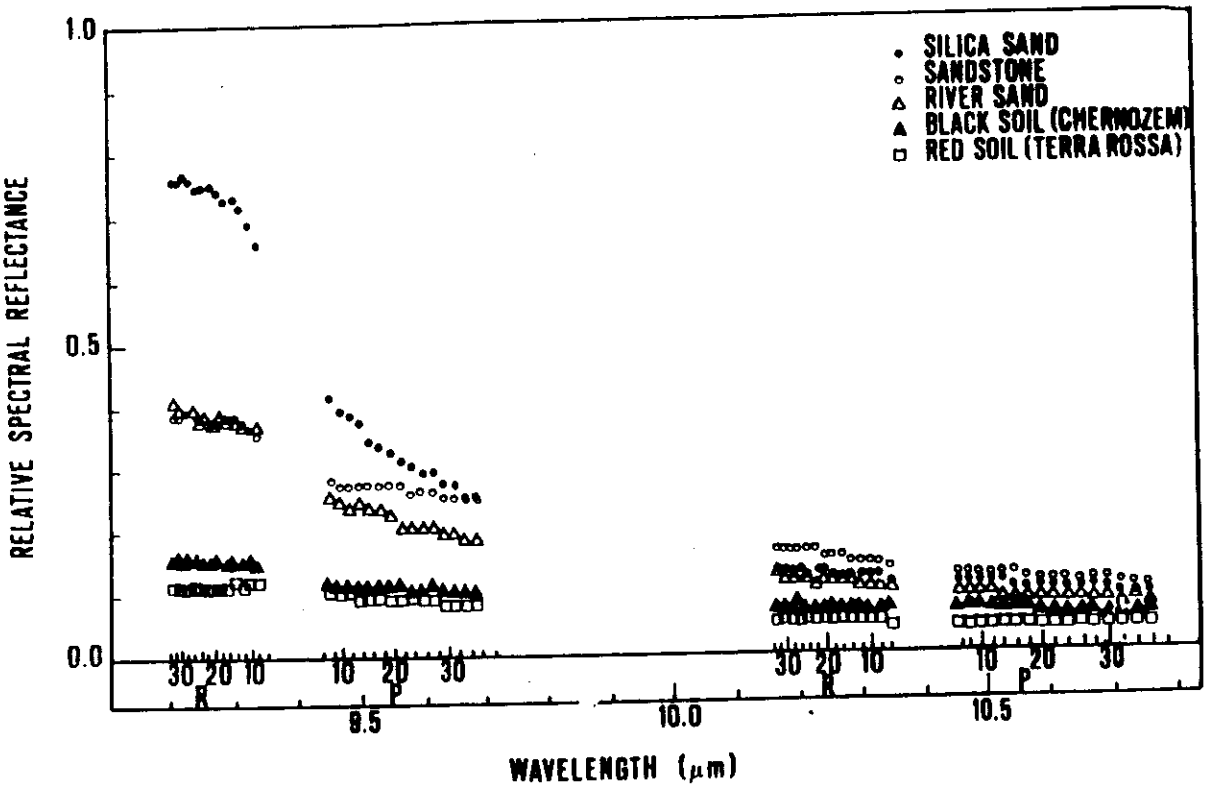
1.0
0.5
0.0
RELATIVE SPECTRAL REFLECTANCE
SILICA SAND
SANDSTONE
RIVER SAND
BLACK SOIL (CHERNOZEM)
RED SOIL (TERRA ROSSA)
30 20 10
R
10 20 30
P
9.5
10.0
10.5
WAVELENGTH (μm)

91

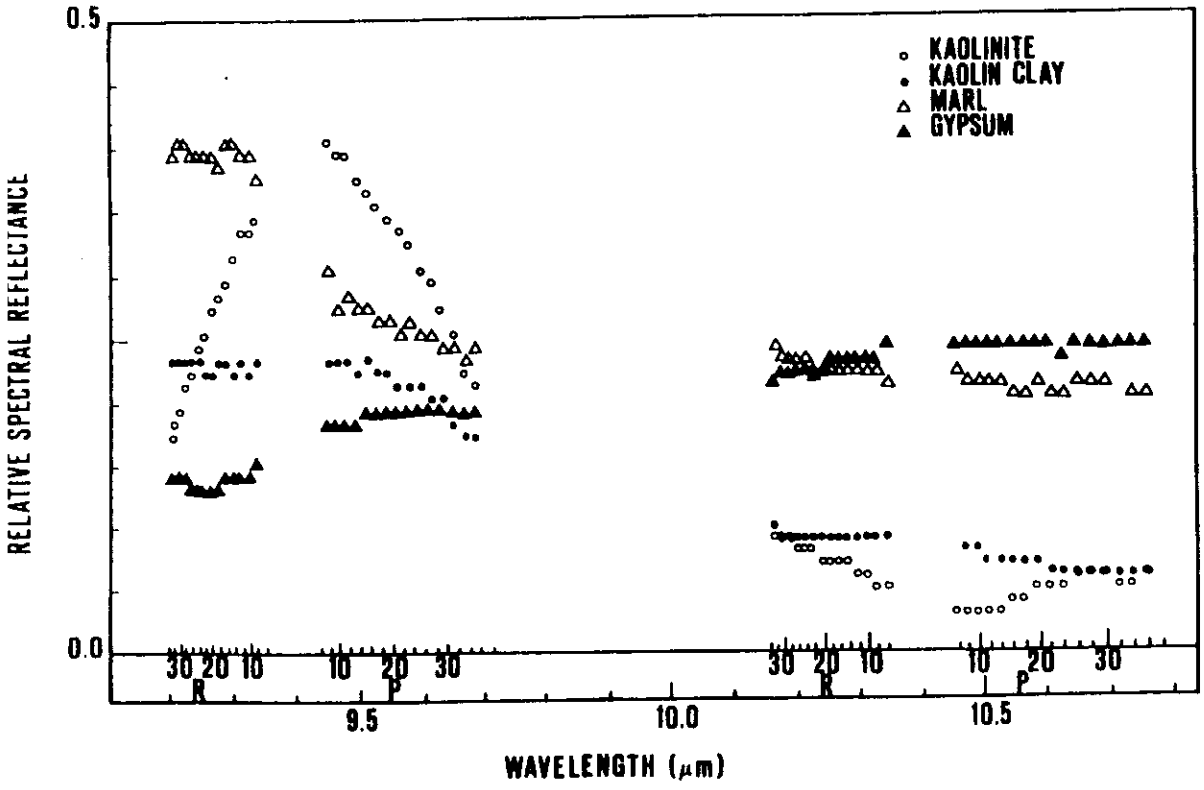
0.5
0.0
RELATIVE SPECTRAL REFLECTANCE
KAOLINITE
KAOLIN CLAY
MARL
GYPSUM
30 20 10
R
10 20 30
P
9.5
10.0
10.5
WAVELENGTH (μm)

92

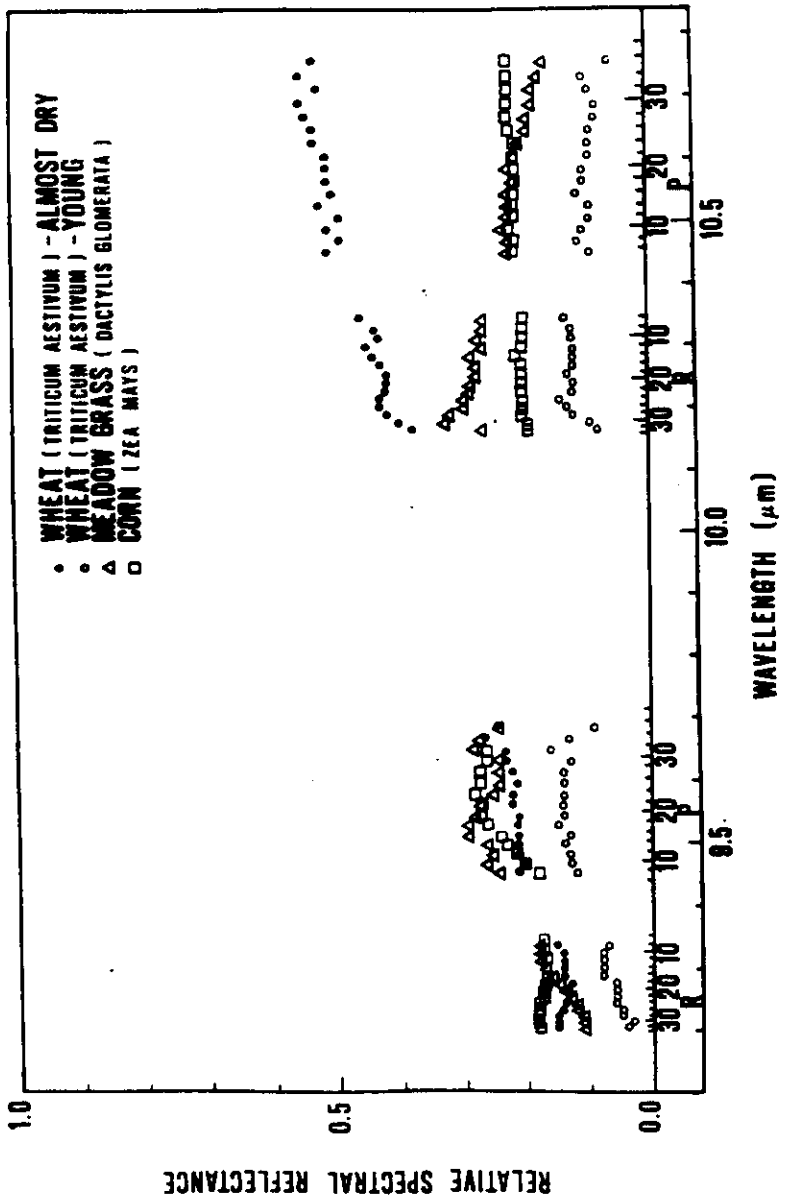

Target		CO_2 laser lines	Reflectance ratio values
Rocks	Granite (black)	9R28,9P1o, 1oR3o,1oP2o, 9R28/9P1o=A 1oR3o/1oP2o=B 1oP2o/9P1o=C 1oR3o/9R28=D	A=o.9 B=1.1 C=1 D=1.3
	Gabbro		A=1.1 B=o.9 C=1.6 D=1.3
	Silica sand		A=2.o B=o.9 C=1.6 D=1.3
	Kaolin(Italy)		A=o.5 B=1.8 C=o.1 D=o.4
	Limestone		A=1.1 B=1.o C=1.o D=1.o
Deciduous trees	Oak	9R2o,1oR2o, 1oR24 1oP24/1oR2o=A 1oP24/9R2o =B	A=1.1 B=1.8
	Ash		A=1.1 B=2.8
	Beech		A=1.o B=1.o
	Hornbeam		A=1.o B=2.1
Coniferous trees	Spruce(P.Excelsa)	9P3o,9R2o 9P3o/9P2o=A	A=o.8
	Spruce(P.omorika)		A=1.o
	Pine		A=1.5
Plants of agricultural interest	Wheat,green	9R26,9P18 1oR26,1oP3o 1oR26/1oP3o=A 9P18/9R26=B	A=1,7 B=3.1
	Wheat,dry		A=o.8 B=1.5
	Grass		A=1.6 B=2.5
	Corn		A=o.9 B=1.4

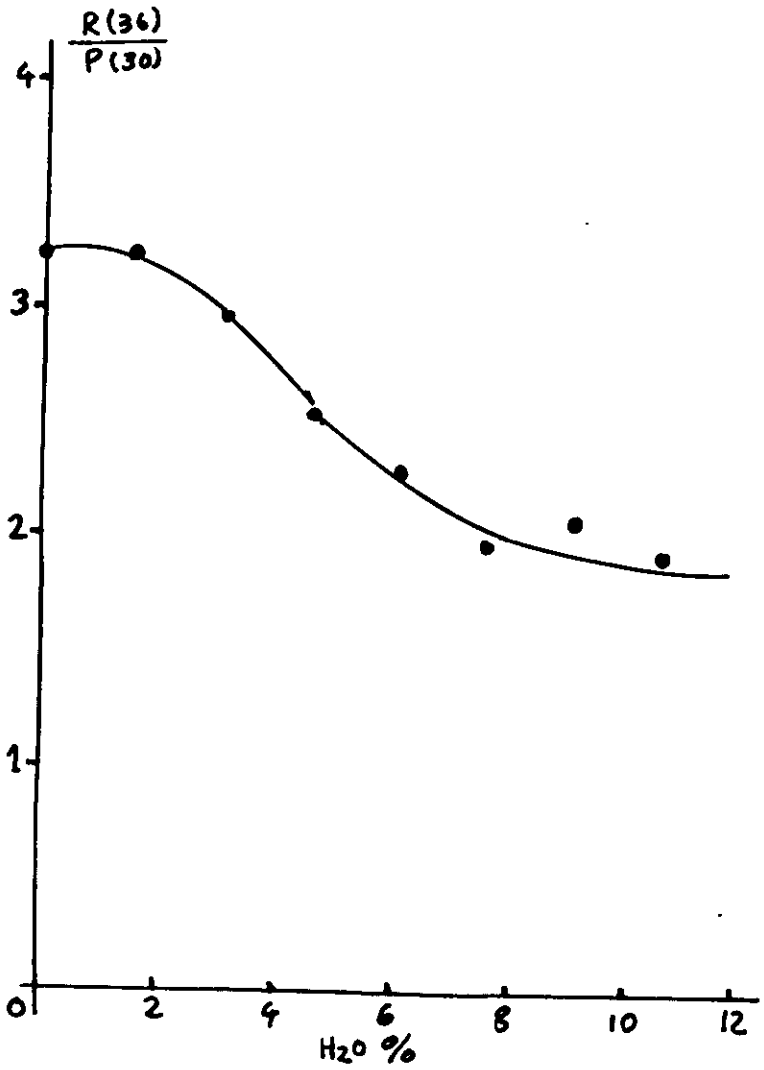

Reprinted from Applied Optics, Vol. 26, page 4323, October 1, 1987

Reflectance spectra of terrestrial surface materials at CO_2 laser wavelengths: effects on DIAL and geological remote sensing

P. Vujkovic Cvijin, D. Ignjatijevic, I. Mendas, M. Sreckovic, L. Pantani, and I. Pippi

Measurements of spectral reflectance of terrestrial surface materials at CO_2 laser wavelengths are reported. Implications on measurement accuracy of long-path airborne differential absorption lidar for atmospheric gas concentration monitoring are discussed. It is also shown that reflectance spectra of most of the terrestrial surface materials are distinguishable enough to enable material identification by remote reflectance measurements at several selected laser wavelengths. This possibility introduces new prospects for active geological (and possibly agricultural) remote sensing.

I. Introduction

Differential absorption lidar (DIAL) based on a CO_2 laser has been successfully used in remote monitoring of a number of trace atmospheric gases.[1,2] Two versions of this instrument exist according to the remote object used to provide the return radiation: (1) range-resolved lidar which makes use of the atmospheric aerosol as a distributed reflector and (2) long-path lidar using topographic targets. Although the first version is more applicable to atmospheric research, many relevant experiments have been performed with long-path lidars used to measure the column content of atmospheric gases.[1-4] In particular, the early research on coherent systems was carried out with lidars of this type.[5-7] Undoubtedly, airborne long-path differential absorption lidars have the highest practical potential among the long-path systems. In this case, the terrestrial surface is irradiated by at least two laser wavelengths, the resonant and the nonresonant for the atmospheric gas of interest, according to the well-known DIAL scheme.[1-4] Gas concentration C averaged over the measurement path is calculated from the equation

$$C = \frac{1}{2R(\alpha^{on} - \alpha^{off})}\left[\ln(P^{off}/P^{on}) + \ln(\rho^{on}/\rho^{off}) + \ln(\eta^{on}/\eta^{off}) - 2R(\beta^{on}/\beta^{off})\right], \quad (1)$$

where the superscripts on and off denote the quantities for the resonant and the nonresonant wavelength, respectively, and where the following symbols have been used: P is the normalized received power, ρ is the target reflectance, η is the system optical efficiency, α is the absorption coefficient for the gas of interest, β is the attenuation coefficient due to scattering and absorption by other atmospheric species, and R is the distance to the target. Obviously, gas concentration measurements made in this way are, among other sources of error, subject to errors originating from nonequal values of ρ^{on} and ρ_{off} (differential reflectance).[8,9]

In the spectral range of the CO_2 laser the target reflectance interference with DIAL measurements can be especially pronounced since this region contains characteristics reststrahlen bands in reflectance of some major minerals, particularly silicates.[7,8,10] From an alternative point of view, the potential to display these spectral features can be used to advantage for active remote sensing of the terrestrial surface lithology based on reflectance measurements.

Historically, the interest in reflectance spectra of terrestrial surface at CO_2 laser wavelengths has been partially induced by experiments with airborne long-path lidars used for trace gas detection. Strong differential reflectance at two CO_2 laser lines was noticed in one of the earliest experiments with an airborne coherent lidar.[11] Differential reflectance has been subsequently studied as an interference effect to atmospheric gas monitoring.[1,8-10,12,13] Remote reflectance measurement as a basis for active geological remote

M. Sreckovic is with University of Belgrade, Faculty of Electrical Engineering, 11001 Belgrade, Yugoslavia; L. Pantani and I. Pippi are with CNR Istituto di Ricerca sulle Onde Elettromagnetiche, 50127 Firenze, Italy; and the other authors are with Institute of Physics, P.O. Box 57, 11001 Belgrade, Yugoslavia.

Received 11 February 1987.
0003-6935/87/194323-07$02.00/0.

sensing has also been the subject of several papers.[13-17] An experiment specifically aimed at active geological remote sensing was carried out with impressive success by Kahle *et al.*[18] who used two CO_2 laser wavelengths available from an airborne coherent lidar originally designed for DIAL measurements of atmospheric gases.

The aim of our paper is to present spectral reflectance data for a number of terrestrial surface materials in an attempt to initiate the larger database apparently needed for the further study of the subject. The present data encompass common samples of terrestrial lithology together with some man-made materials and vegetation samples. This database fulfills a dual goal: (1) to evaluate the possible measurement error in DIAL measurements of atmospheric gases and (2) to give initial parameters for the broader study of laser active remote sensing of the terrestrial surface.

II. Description of the Experimental Apparatus

The laboratory instrument intended to provide spectral reflectance data for lidar monitoring is designed to follow the geometry of the lidar itself. The sample under study is irradiated and observed through small solid angles whose axes are close to each other and close to the normal incidence on the sample (Fig. 1). The laser beam of a grating-tunable pulsed TEA CO_2 laser operating in the TEM_{00} mode is attenuated approximately by a factor of 100 and expanded by a factor of 2.5 giving a 20-mm diam illuminated spot at the sample. The instantaneous energy density at the sample is <1 mJ cm^{-2}. The sample is placed at the center of a turntable rotating at 30 rpm. The transmitted beam strikes the sample off-center. The motion of the sample surface past the transmitted beam permits averaging of the signal fluctuations due to both macroscopic irregularities in the sample surface structure and the coherent speckle effects, as suggested previously.[10] A zinc selenide lens images the illuminated spot to a pyroelectric receiving detector. No provision has been made to distinguish between the components of polarization. A pyroelectric joulemeter monitors the laser output energy and provides the energy normalization signal (Fig. 1). The normalized signal is digitized and stored in the computer memory. The experiment is under computer control through a program which tunes the laser wavelength, fires the laser, acquires the data, and performs data processing. Wavelength tuning is performed by a closed-loop grating positioning system.[19] The data processing procedure includes calculations of the signal mean value, standard deviation, and histogram.

III. Experimental Results

The relative spectral reflectance is generally defined as the ratio of the biconical spectral reflectance of the surface under study to that of the selected standard surface.[20] This quantity has been measured here with the apparatus of Fig. 1. When both the angle of irradiation and the angle of observation are small, the definition of bidirectional spectral reflectance, as a special case of biconical spectral reflectance, is applicable.[20] This holds for lidar and for our laboratory apparatus as well. Consequently, in our case, the relative spectral reflectance equals the ratio of the bidirectional spectral distribution function of the given surface to that of the standard surface, both averaged over finite small angles of observation.

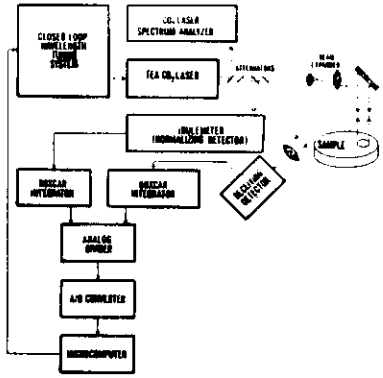

Fig. 1. Experimental apparatus.

Major nonuniformities in the spectral response of the apparatus were found due to the known nonuniform response of the receiving $LiTaO_3$ pyroelectric detector in this spectral range. Accordingly, all the reflectance spectra recorded were normalized to the spectral response of the instrument.

Following the definition of the relative spectral reflectance and the practice of diffuse reflectance spectroscopy in the visible (see, e.g., Ref. 21) to use a certain convenient surface as a standard for reflectance measurements ($BaSO_4$ or MgO in the visible), an appropriate surface in the CO_2 laser wavelength range has to be adopted. Practical reasons dictate that standard surface should have (1) uniform radiance of the scattered radiation in all directions, i.e., Lambertian surface, (2) high reflectance, i.e., close to the ideal Lambertian surface, (3) uniformity of reflectance in the spectral region of interest and, additionally, (4) permanence of surface and its reproducibility. The surface of sublimed sulfur flowers has been studied previously[22-24] for use in the infrared. The reflectance spectrum of sulfur flowers at CO_2 laser wavelengths, as recorded by our apparatus, is presented in Fig. 2 along with other materials studied as possible reflectance standards. It is obvious that sulfur flowers show uniform reflectance only in the 9-μm CO_2 laser band, while there is a remarkable minimum coinciding with the P branch of the 10-μm band.[24] It follows that this material does not fulfill the spectral uniformity requirement in the entire CO_2 laser spectral range. A surface of finely divided sodium chloride was also suggested as a candidate for the reflectance standard because of its high reflectance and close-to-Lambertian distribution, similar to that of sulfur flowers.[22] A reflectance spectrum of finely divided sodium chloride is presented in Fig. 2. The sample was prepared by pestle-and-mortar grinding the sodium chloride and then sifting it through a mesh size 70 sieve. Because of its hygroscopic nature, sodium chloride was kept at higher than ambient temperature during the measurements.

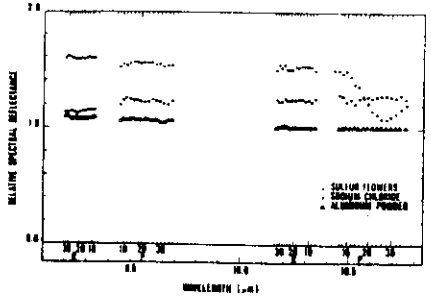

Fig. 2. Reflectance spectra of potential reflectance standards.

Finely divided aluminum was also studied (Fig. 2). This surface was obtained by sifting chemically pure aluminum powder through a mesh size 70 sieve. The surface obtained was afterward left intact. As seen in Fig. 2, the surface of finely divided aluminum offers the best spectral uniformity of the materials considered here. Furthermore, the angular radiance distribution of finely divided aluminum has been measured previously and has been found to approximate closely the Lambertian distribution.[22] However, the grain size of the sample is an important factor since it is known that the ability of this surface to approximate the Lambertian surface is dependent on the grain size (for coarser grains specular reflection appears[22]). It is also expected that finely divided aluminum is more stable against environmental influences than, e.g., sodium chloride, which is otherwise also acceptable. Consequently, the surface of finely divided aluminum, prepared as described above, is adopted here as the standard of reflectance. All the following spectral reflectance data are given in terms of relative reflectance related to this standard surface.

Figure 3 presents the reflectance spectra of silicate rocks dacite, andesite, gabbro, and two types of granite. As expected, reflectance bands appear as rather broad spectral features situated in different portions of the CO_2 laser spectral range depending on the mineral composition of the rock. The presence of the well-known reststrahlen band of quartz in the 9-μm region is evident in the spectra of dacite and white granite. The reflectance spectrum of dacite in Fig. 3 is noisy because of the pronounced porfiric structure of the sample. The reflectance maximum of gabbro is situated at longer wavelengths with respect to quartz-containing rocks since in the mineral composition of the gabbro sample other silicate minerals dominate. Spectra of the two varieties of granite clearly reveal differences in their mineral composition. The spectra of materials with high quartz content are presented in Fig. 4 together with the spectra of two types of soil. An intense reststrahlen band of quartz around 9 μm is exhibited by silica sand, river sand, and sandstone. Both spectra of soils (black farmland soil of the chernozem type and red soil of the Mediterranean terra rossa type) reveal a moderate quartz content. The reflectance spectrum of pure kaolinite (Fig. 5) shows

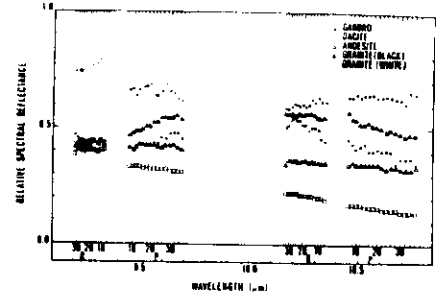

Fig. 3. Reflectance spectra of some silicate rocks.

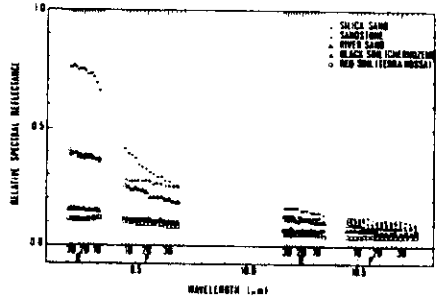

Fig. 4. Reflectance spectra of sand, sandstone, and soil.

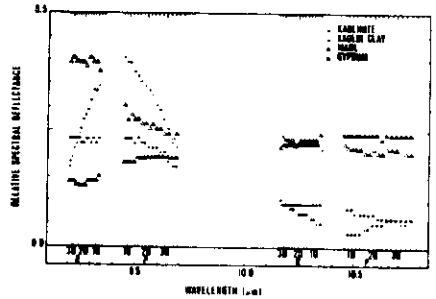

Fig. 5. Reflectance spectra of pure kaolinite, kaolin clay, marl, and gypsum.

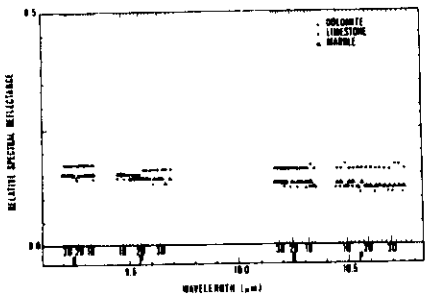

Fig. 6. Reflectance spectra of some carbonate rocks.

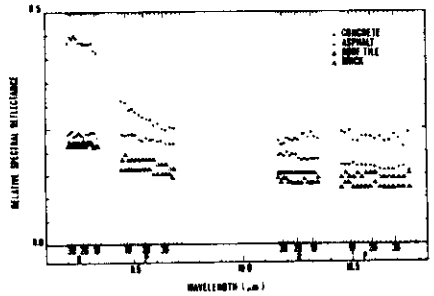

Fig. 7. Reflectance spectra of man-made materials.

the reststrahlen band centered around 9.45 μm. Natural kaolin clay (Fig. 5) apparently contains quartz in addition to kaolinite. The spectra of marl, a mineral containing both carbonates and silicates (obviously quartz in our sample) and gypsum, containing no silicates, are also presented in Fig. 5. Carbonate rocks limestone, marble, and dolomite (Fig. 6) show featureless spectra in this range confirming that carbonates have no reststrahlen bands here.[25]

Man-made construction materials are considered next (Fig. 7). Concrete, brick, and roofing tile contain silicate sands or clays, presumably in large quantities in our case, and accordingly show quartz reststrahlen. The reflectance spectrum of typical road construction asphalt (Fig. 7) is noisy due to the evidently inhomogeneous structure of the material but is otherwise featureless in this range.

Although much less treated in the literature than geological samples, reflectance spectra of vegetation in the middle infrared region are certainly of interest for active remote sensing. Spectra of foliage, grass, and agricultural plants are presented in Figs. 8–10. Due to the large specular component of the reflected radiation, sample rotation (Sec. II) has not been used with the vegetation samples. Consequently, absolute reflectance values for different samples can hardly be compared due to the lack of averaging. Nevertheless,

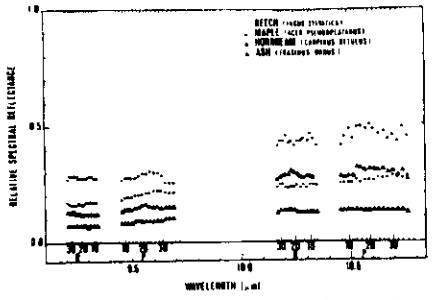

Fig. 8. Reflectance spectra of leaves (deciduous trees).

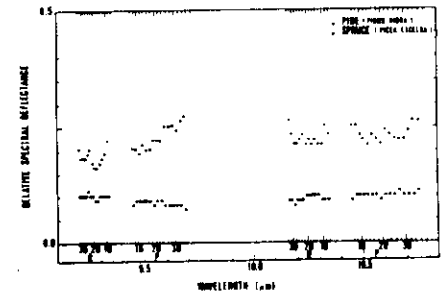

Fig. 9. Reflectance spectra of leaves (coniferous trees).

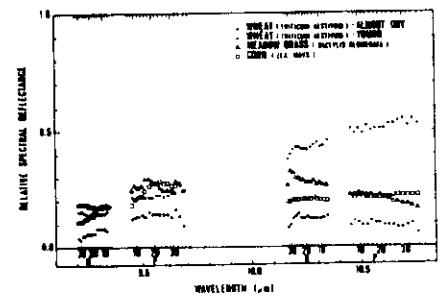

Fig. 10. Reflectance spectra of meadow grass, wheat, and corn leaves.

conclusions regarding the spectra itself (positions and relative intensities of maxima) will in general still hold. Measurements were performed with the samples close to the *in vivo* condition. Water was continuously supplied to the samples from the moment of picking until the end of measurements. Reflectance spectra of leaves of typical deciduous trees (beech, maple, hornbeam, ash) are presented in Fig. 8. Generally, higher reflectance in the 10-μm than in the 9-μm region is

Table I. Long-Path DIAL Gas Concentration Measurement Errors (σN), (ppb · km) Due to Differential Reflectance

Gas	NH_3		O_3			H_2O			C_2H_4			C_2H_3Cl	CCl_2F_2	N_2H_4	UDMH	MMH
λ_{on}	9R(30)	10R(18)	9P(14)	9P(12)	9P(26)	10R(20)	10P(14)	10P(14)	10P(14)	10P(14)	10P(14)	10P(22)	10P(34)	10P(22)	10P(30)	10R(30)
λ_{off}	9R(28)	10R(12)	9P(22)	9P(24)	9P(24)	10R(18)	10P(16)	10P(12)	10P(18)	10P(20)	10P(22)	10P(20)	10P(22)	10P(28)	10R(10)	9R(18)
Ref.	8	26	7, 27	28	6	29,30	31	3	32	33, 34	26	8, 33	26	35	35	35
$\Delta\sigma$(kPa · m)$^{-1}$	55.3	25.5	10.9	11.5	11.6	4.9	7.6×10^{-4}	24.2	27.4	32.0	27.1	30.3	4.8	43.5	2.7	2.0	1.4
Silica sand	−0.1	−5.9	74	89	99	−20	47,000	2.6	−2.2	3.9	7.0	8.4	−14	−10	89	−520	−6,300
Sandstone	−0.3	−9.9	12	15	17	−5	71,000	2.2	−1.8	3.4	6.1	7.5	−13	−11	90	−680	−3,100
Kaolin clay	0.5	−1.3	24	34	35	−15	14,000	8.5	−8.1	12	21	23	−30	−5.1	105	−1,010	−3,200
Dacite	−0.3	−4.6	6.1	7.5	8.2	−1.9	49,000	2.6	2.3	4	7.2	8.6	−14	−10	90	−610	−1,300
Andesite	0.1	−2.3	−6.0	−5.5	−7.1	−0.9	3,200	1.1	−1	1.7	2.9	3.4	−5.1	−3.1	29	−190	−710
Granite (white)	−0.4	−6.4	8.7	11	12	−3.2	47,000	3.1	−2.8	4.7	8.3	9.9	−15.5	−10.7	95.4	−800	−2,200
Marl	−0.1	−3.0	31	37	42	−8	32,000	0.7	−0.6	1	1.8	2.2	−3.5	−2.5	22	−160	−1,900
Limestone	0	0.6	−9	−12	−12	3.2	−7,000	−0.2	0.2	−0.4	−0.6	−0.8	1.2	0.9	−7.7	−60	−230
Dolomite	0.2	−2.3	4.5	5.5	6	−2.9	25,000	0.5	−0.4	0.7	1.3	1.6	2.5	−1.8	15.8	−130	−490
Black soil	−0.3	−0.9	12	16	17	−5.6	9,500	2.7	−2.4	4.2	7.4	8.9	−14	−11	93	−380	−2,700
Red soil	−0.6	−2.7	28	35	39	−9.6	29,000	0	−2.5	0	2.7	3.6	−8	−2.2	0	−440	−2,900
Concrete	0	−2.4	37.2	43.3	49	−8.5	26,000	0.9	−0.8	1.4	2.5	2.9	−4.7	−3.4	30	−300	−2,900
Roof tile	−0.5	−0.9	8.4	12.8	12.8	−6.6	9,500	0.2	−0.2	0.3	0.5	0.5	−0.9	−0.6	5.5	−60	−1,300
Asphalt	0.1	2.2	13	16	18	−4.3	25,000	0.7	−0.6	1.0	1.8	2.2	−3.5	−2.5	22	−80	−290
Maple	0.2	2.7	−35	−38	−45	4.3	−7,600	−1.7	1.5	−2.5	−4.4	−5.2	8.0	5.3	−48	330	1,300
Hornbeam	0.6	−4.6	−31	−38	−42	9.3	29,000	−0.3	0.4	−0.3	−0.3	−0.1	−1.3	−13	47	200	3,000
Ash	0.6	−2	−19	−19	−27	−0.8	18,000	−3.8	3.4	−5.5	−8.9	−9.3	8.1	−13	47	200	−450
Spruce	0.8	−6.8	4.8	10.5	9.1	−8.9	−29,000	−0.8	0.6	−1.3	−2.4	−3.0	5.5	5.0	−46	210	2,500
Grass	−5.1	−5.3	7.8	19	12	−14	49,000	2.1	−1.4	3.6	7.1	9.4	−19	−24	170	−900	2,500
Wheat (young)	−8.4	4.9	−31	−27	−36	−7.0	120,000	0.8	−0.2	1.7	3.9	5.7	−14	−21	140	−770	1,200

Table II. Identification of Terrestrial Surface Materials by Four-Wavelength Reflectance Measurements

Target surface	Characteristic ratios				Wavelengths and characteristic ratios used
A. Geological samples	A_1	A_2	A_3	A_4	
Silica sand	1.85	1.27	0.25	0.17	Wavelengths:
Kaolinite	0.49	1.96	0.11	0.46	9.219 μm(9R30); 9.458 μm(9P8)
Dacite	1.11	1.32	0.60	0.72	10.182 μm(10R30); 10.59 μm(10P20)
Limestone	1.13	0.99	1.07	0.94	Ratios:
Gypsum	0.77	0.90	1.34	1.56	$A_1 = \mu(9R30)/\mu(9P8)$; $A_2 = \mu(10R30)/\mu(10P20)$
Black soil	1.35	1.10	0.59	0.48	$A_3 = \mu(10P20)/\mu(9P8)$; $A_4 = \mu(10R30)/\mu(9P30)$
B. Vegetation samples	B_1	B_2	B_3	B_4	
Maple	1.32	1.16	0.79	0.67	Wavelengths:
Grass	2.27	0.63	1.35	1.68	9.219 μm(9R30); 9.639 μm(9P30)
Spruce	0.90	1.16	0.79	1.01	10.195 μm(10R28); 10.696 μm(10P30)
Wheat (young)	3.37	0.77	1.58	2.13	Ratios:
Wheat (dry)	1.55	1.31	0.44	3.52	$B_1 = \rho(9P30)/\rho(9R30)$; $B_2 = \rho(10P30)/\rho(10R28)$
					$B_3 = \rho(9P30)/\rho(10P30)$; $B_4 = \mu(10P30)/\rho(9R30)$

obvious. Spectra of the coniferous trees foliage, on the other hand, show no tendency of higher reflectance toward longer wavelengths (Fig. 9). Reflectance spectra of meadow grass, wheat, and corn leaves are presented in Fig. 10. Besides the distinctive reflectance maximum of corn at ~9.6 μm, it is probably of interest for agricultural remote sensing to note the different spectrum of young green wheat compared with that of wheat at the time of harvest (almost dry leaves).

IV. Discussion

As pointed out in Sec. I, target differential reflectance tends to interfere with long-path DIAL atmospheric gas concentration measurements. Measurement error due to differential reflectance may be conveniently defined[8] as the concentration-path-length product $(CR)_\epsilon$ resulting from Eq. (1) for $P^{on} = P^{off}$, $\eta^{on} = \eta_{off}$, and $\beta^{on} = \beta^{off}$. Calculated values of $(CR)_\epsilon$ are tabulated in Table I. To minimize the uncertainty originating from the experimental error associated with, in some cases, noisy reflectance spectra, a least-squares polynomial fit was performed on reflectance spectra prior to calculation of the $(CR)_\epsilon$. Table I contains nine gases reported previously to be measured by CO_2 differential absorption lidars: ammonia (NH_3), ozone (O_3), water vapor (H_2O), ethylene (C_2H_4), vinyl chloride (C_2H_3Cl), Freon 12 (CCl_2F_2), hydrazine (N_2H_4), unsymmetrical dimethylhydrazine—UDMH [$(CH_3)_2N_2H_2$] and monomethylhydrazine—MMH ($CH_3N_2H_3$). References to the original publications are given in Table I together with the laser lines used (λ^{on} and λ^{off}) and the gas differential absorption coefficients $\Delta\alpha = \alpha^{on} - \alpha^{off}$.

Results given in Table I show large quartz restatrahlen band interference with ozone concentration measurements, as expected.[8,16] This interference is noticeable with all natural and man-made materials containing quartz. Gas concentration measurement errors calculated here for the silica sand target are in close agreement with the results published previously.[8,9] It is also evident from Table I that nonuniformities of the vegetation reflectance spectra can seriously affect gas concentration measurements (particularly ozone again). Generally, these results show that for any real terrestrial surface, two effects increase the gas concentration measurement error: (1) small value of the differential absorption coefficient $\Delta\alpha$, and (2) large separation between the sounding laser wavelengths. When both of these adverse effects are present, the resulting errors are excessively large, as in unsymmetrical dimethylhydrazine $(CH_3)_2N_2H_2$ and monomethylhydrazine $CH_3N_2H_3$. It is important to point out that, although the errors in water vapor concentration measurements are large in terms of ppb · km (Table I), these values are within a few percent of the usual water vapor concentrations in the atmosphere.

The reflectance spectra of terrestrial surface materials presented here indicate the possibility of identification of a significant number of those materials by measuring their reflectance at selected CO_2 laser wavelengths. This possibility, as noted before,[10,13-18] introduces new prospects for active remote sensing of the earth's surface from airborne or spaceborne platforms. The complexity of the actual airborne or spaceborne apparatus for this purpose will critically depend on the number of CO_2 laser wavelengths necessary for reliable identification. Consequently, the possibility of target classification by using a limited (as small as possible) set of laser wavelengths is highly important. We estimate that a four-wavelength lidar can be built at the present level of technology, so the identification of reflectance spectra by four-wavelength sounding is preliminarily considered here. The ratios of reflectance data at selected wavelengths are calculated and used to characterize the sample. In Table II, four ratios characterize each sample. Sounding wavelengths have been chosen to probe the characteristic features of the spectra in Figs. 3–10. It is evident that good discrimination of target materials in two classes (geological and vegetation) can be obtained in this way. It is expected that number and/or positions of laser wavelengths can be further optimized by a more elaborate wavelength selection procedure.

V. Conclusions

The potential gas concentration measurement errors presented in Table I show that the interference due to the differential reflectance effect may turn out to be the largest single source of error with long-path lidars. Since a DIAL is usually envisioned as a device for accurate measurements at trace concentration levels, errors ranging from several ppb · km to several tens of ppb · km are generally not tolerable. Improvements in topographic target return DIAL methodology is obviously required, as noted earlier.[8,9,13] Two approaches could be taken to minimize the differential reflectance interference.[8,9] The first approach is to minimize the spacing between the resonant and the nonresonant lines either by using CO_2 lasers of different CO_2 isotopes to obtain wavelength separation smaller than between the ordinary lines or by using continuously tunable (high pressure) CO_2 lasers. The second approach would be to use two or more nonresonant wavelengths to interpolate or extrapolate the effects of nonuniform target reflectance.[9]

Reflectance spectra of most of the terrestrial surface materials studied herein are distinguishable enough to enable material identification by remote reflectance measurements at a practical number of laser wavelengths. Consequently, active remote sensing based on reflectance measurements should be regarded as a potentially powerful alternative or addition to the existing passive remote sensing techniques in the thermal infrared channel. Although geological remote sensing based on emittance measurements has achieved remarkable success in the past, several advantages of the active technique based on reflectance measurements are anticipated[17,18]: (1) higher signal-to-noise ratio is attainable with the laser-based reflectance technique, (2) better spectral resolution is available, (3) higher immunity to background effects exists, since measurements are little affected by surface temperature, and (4) adverse atmospheric effects are expected to have less influence on measurements. However, two disadvantages of the active approach should be immediately pointed out. First, the spectral range of the standard $^{12}C^{16}O_2$ laser restricts the applicability of the technique in comparison with the broadband passive sensors. This limitation could be nearly removed by using isotopic CO_2 lasers to extend the spectral range well beyond 11 μm, thereby reaching the sharp reflectance band of carbonate rocks situated at 11.3 μm.[25] Second, at the present level of development, the laser system picks out reflectance data from a narrow stripe on the terrestrial surface as the instrument passes overhead, in contrast to the passive sensor which has large areal coverage in a single pass.[18] With the implementation of rapid beam-scanning systems, this problem should be alleviated in the future, but at the cost of somewhat increased system complexity.

This work was partially supported by the Yugoslav–Italian government agreement on scientific cooperation. L. Pantani and I. Pippi also acknowledge the partial support of CNR and that of IPRA subproject 1 (No. 1288).

References

1. D. K. Killinger and A. Mooradian, Eds., *Optical and Laser Remote Sensing* (Springer, Berlin, 1983).
2. W. B. Grant and R. T. Menzies, "A Survey of Laser and Selected Optical Systems for the Remote Measurements of Pollutant and Gas Concentrations," J. Air Pollut. Control Assoc. **33**, 187 (1983).
3. D. K. Killinger and N. Menyuk, "Remote Probing of the Atmosphere Using a CO_2 DIAL System," IEEE J. Quantum Electron. **QE-17**, 1917 (1981).
4. W. B. Grant, "He–Ne and cw CO_2 Laser Long-Path Systems for Gas Detection," Appl. Opt. **25**, 709 (1986).
5. R. T. Menzies and M. S. Shumate, "Remote Measurements of Ambient Air Pollutants with a Bistatic Laser System," Appl. Opt. **15**, 2080 (1976).
6. R. T. Menzies and M. S. Shumate, "Tropospheric Ozone Distributions Measured with an Airborne Laser Absorption Spectrometer," J. Geophys. Res. **83**, 4039 (1978).
7. M. S. Shumate, R. T. Menzies, W. B. Grant, and D. S. McDougal, "Laser Absorption Spectrometer: Remote Measurement of Tropospheric Ozone," Appl. Opt. **20**, 545 (1981).
8. W. B. Grant, "Effect of Differential Spectral Reflectance on DIAL Measurements Using Topographic Targets," Appl. Opt. **21**, 2390 (1982).
9. N. Menyuk and D. K. Killinger, "Assessment of Relative Error Sources in IR DIAL Measurement Accuracy," Appl. Opt. **22**, 2690 (1983).
10. M. S. Shumate, S. Lundqvist, U. Persson, and S. T. Eng, "Differential Reflectance of Natural and Man-Made Materials at CO_2 Laser Wavelengths," Appl. Opt. **21**, 2386 (1982).
11. W. Wiesemann, R. Beck, W. Englisch, and K. Gurs, "In-Flight Test of a Continuous Laser Remote Sensing System," Appl. Phys. **15**, 257 (1978).
12. K. Asai and T. Igarashi, "Interference from Differential Reflectance of Moist Topographic Targets in CO_2 DIAL Ozone Measurement," Appl. Opt. **23**, 734 (1984).
13. W. Wiesemann and F. Lehmann, "Reliability of Airborne CO_2 DIAL Measurements: Schemes for Testing Technical Performance and Reducing Interference from Differential Reflectance," Appl. Opt. **24**, 3481 (1985).
14. W. Wiesemann, F. Lehmann, and Ch. Werner, "Probing of the Earth's Surface and the Atmosphere with an Airborne Laser Spectrometer," Infrared Phys. **25**, 467 (1985).
15. F. Lehmann, C. Werner, and W. Wiesemann, "LIMES: An Optical Multisensor Combining Mid-IR Laserscanner and Multispectralscanner," in *Proceedings, EARSeL/ESA Symposium on European Remote Sensing Opportunities*, Strasburg, ESA SP-233 (May 1985), p. 115.
16. P. Vujkovic Cvijin, D. Ignjatijevic, M. Sreckovic, L. Pantani, and I. Pippi, "Spectral Reflectance of Topographic Target Surface Materials: Implications on Wavelength-Scanning CO_2 Laser-Based Lidars," in *Proceedings, Twelfth International Laser Radar Conference*, Aix-en-Provence (1984), p. 357.
17. J. E. Eberhardt, J. G. Haub, and A. W. Pryor, "Reflectivity of Natural and Powdered Minerals at CO_2 Laser Wavelengths," Appl. Opt. **24**, 388 (1985).
18. A. B. Kahle, M. S. Shumate, and B. D. Nash, "Active Airborne Infrared Laser System for Identification of Surface Rock and Minerals," Geophys. Res. Lett. **11**, 1149 (1984).
19. D. Ignjatijevic, P. Vujkovic Cvijin, M. Sreckovic, and I. Pippi, "A Simple Microcomputer-Controlled CO_2 Laser Wavelength Tuning System," Opt. Laser Technol. **17**, 96 (1985).
20. J. F. Snell, "Radiometry and Photometry," in *Handbook of Optics*, W. G. Driscoll and W. Vaughan, Eds. (McGraw-Hill, New York, 1978).
21. W. W. Wendlandt and H. G. Hecht, Reflectance Spectroscopy (*Interscience*, New York, 1966).
22. J. T. Agnew and R. B. McQuistan, "Experiments Concerning Infrared Diffuse Reflectance Standards in the Range 0.8 to 20.0 Microns," J. Opt. Soc. Am. **43**, 999 (1953).
23. M. J. Kavaya, R. T. Menzies, D. A. Haner, U. P. Oppenheim, and P. H. Flamant, "Target Reflectance Measurements for Calibration of Lidar Atmospheric Backscatter Data," Appl. Opt. **22**, 2619 (1983).
24. D. B. Nash, "Mid-Infrared Reflectance Spectra (2.3–22 μm) of Sulfur, Gold, KBr, and Halon," Appl. Opt. **25**, 2427 (1986).
25. R. K. Vincent, "The Potential Role of Thermal Infrared Multispectral Scanners in Geological Remote Sensing," Proc. IEEE **63**, 137 (1975).
26. P. Vujkovic Cvijin and N. Konjevic, "Molecular Air Pollution Monitoring by Pulsed CO_2 Laser-Based Long-Path Technique," Spectrosc. Lett. **13**, 861 (1980).
27. R. W. Stewart and J. L. Bufton, "Development of a Pulsed 9.5 Micrometer Lidar for Regional Scale Ozone Measurement," Opt. Eng. **19**, 503 (1980).
28. K. Asai, T. Itabe, and T. Igarashi, "Range-Resolved Measurements of Atmospheric Ozone Using a Differential Absorption CO_2 Laser Radar," Appl. Phys. Lett. **35**, 60 (1979).
29. E. R. Murray, R. D. Hake, Jr., J. E. van der Laan, and J. G. Hawley, "Atmospheric Water Vapor Measurements with an Infrared (10 μm) Differential-Absorption LIDAR System," Appl. Phys. Lett. **28**, 542 (1976).
30. P. W. Baker, "Atmospheric Water Vapor Differential Absorption Measurements on Vertical Paths with a CO_2 Lidar," Appl. Opt. **22**, 2257 (1983).
31. E. R. Murray and J. E. van der Laan, "Remote Measurement of Ethylene Using a CO_2 Differential-Absorption Lidar," Appl. Opt. **17**, 814 (1978).
32. K. W. Rothe, "Monitoring of Various Atmospheric Constituents Using a CW Chemical Hydrogen/Deuterium Fluoride Laser and a Pulsed Carbon Dioxide Laser," Radio Electron. Eng. **50**, 567 (1980).
33. B. Marthinsson, J. Hohansson, and S. T. Eng, "Air Pollution Monitoring with a Computer-Controlled CO_2-Laser Long-Path Absorption System," Opt. Quantum Electron. **12**, 327 (1980).
34. S. Lundqvist, C-O. Falt, U. Persson, B. Marthinsson, and S. T. Eng, "Air Pollution Monitoring with a Q-Switched CO_2-Laser Lidar Using Heterodyne Detection," Appl. Opt. **20**, 2534 (1981).
35. N. Menyuk, D. K. Killinger, and W. E. DeFeo, "Laser Remote Sensing of Hydrazine, MMH, and UDMH Using a Differential-Absorption CO_2 Lidar," Appl. Opt. **21**, 2275 (1982).

A NEW LIDAR SYSTEM FOR APPLICATIONS OVER LAND AND SEA

F Castagnoli*, G Cecchi*, L Pantani*, B Radicati* & P Mazzinghi**

*Istituto di Ricerca sulle Onde Elettromagnetiche
C.N.R.
Firenze, Italy

**Istituto di Elettronica Quantistica
C.N.R.
Firenze, Italy

A.Barbaro, M.Romoli
University of Firenze, Italy

ABSTRACT

SIx years of researches were carried out on the use of fluorescence lidars for environmental monitoring. As a result a sensor prototype was designed and built which can operate as a fluorescence lidar and a passive spectrometer in the visible, in both cases with a high spectral resolution. This paper describes the researches carried out, the sensor, and the first field experiments on sea and vegetation remote sensing.

Keywords: Lidar, Remote Sensing, Environmental Control, Fluorosensor, Vegetation Monitoring, Pollution Monitoring, Oil Spills

1. INTRODUCTION

The lidar is one of the most powerful tools for environmental remote sensing; its applications range from meteorological measurements to pollution monitoring, from upper atmosphere investigations, to water bathymetry (Ref.1).

Between the different lidar systems the fluorescence lidar is a very attractive one which shows an interesting potential in the remote sensing of marine and vegetation parameters. Researches on fluorescence lidar systems and applications were carried out in the last 6 years at the IROE-CNR in cooperation with the IEQ-CNR; the FLIDAR 2 prototype is the result of these researches.

This paper describes the researches carried out, the sensor, and the results of the first field experiments performed on both vegetation and natural water.

2. CHLOROPHYLL REMOTE SENSING

Chlorophyll plays a fundamental role in the photosynthetic process of living plants, therefore such processes related to chlorophyll may be also related to the photosynthetic process. Since chlorophyll a shows a strong fluorescence emission in the wavelength region between 670 nm and 740 nm it is attractive to analyze the potential of laser fluorosensors in the remote sensing of living plants (Ref.2).

A research program on the use of laser induced fluorescence applications to the remote sensing of vegetation was started as a part of a national program on agricolture improvements (IPRA Project). The laser induced fluorescence in living plants was analyzed by means of a lidar simulator composed by different laser heads, a suitable focusing and receiving optics, a grating spectrometer and a PAR OMA-2 multichannel analyzer. High resolution fluorescence spectra were detected and processed in order to investigate their behavior and the relationships with the photosynthetic process for a forecasting of the lidar fluorosensor potential in the detection of plant health (Ref.3, 4). Different phenomena were taken into account like the change of the intensity and behavior of the spectrum with the excitation wavelength, the exposure time to the laser radiation, the background radiation level, etc. (Ref.5).

As a result a physical model of chlorophyll fluorescence in living plants and of its relationships with the photosynthetic process was developed; this model fits quite well the experimental results (Ref.6).

A second part of the laboratory experiments was devoted to the detection of laser induced fluorescence spectra of living plants submitted to water stress and cold stress. These experiments showed the influence of the stresses in the ratio between the two peaks of the fluorescence spectrum at 685 nm and 730 nm.

3. SEA REMOTE SENSING

A systematic analysis of fluorosensor performances in detection and characterization of oil films

was carried out as a part of the IROE program of environmental remote sensing. The investigation concerned (Ref.7, 8, 9) the definition of the best laser wavelength, the measurement of oil film thickness, the minimum, detectable film thickness, the identification of the oil which composes the film.

The analysis was mainly done using the lidar simulator. The first experiments were devoted to the identification of the most suitable laser source for oil detection. The parameters taken into account were:

- The oil fluorescence efficency
- The atmospheric absorption at both the excitation and fluorescence wavelengths
- The laser efficency

The Xe-Cl excimer laser gave the best compromise for thin oil films while an excimer pumped dye laser operating at about 420 nm gave the best compromise for thick layers. The minimum detectable thickness for Xe-Cl excitation was identified in about 10 nm.

If the film thickness is lower than the optical penetration depth in the oil at the involved wavelengths it can be measured or by the intensity of the fluorescence signal, which increases with the thickness, or by the intensity of the water Raman signal, which decreases with the thickness. The experiments showed that the use of the Raman signal depression is more suitable for thicknesses below 1m.

In the measurement of film thickness the oil absorption at the involved wavelengths is an important parameter which is practically impossible to obtain by standard techniques. An original and easy technique for the measurement of the extinction coefficient in high absorbing liquids was identified during these experiments (Ref.10).

The potential of the lidar fluorosensor in the identification of the oil which composes the film was investigated with the aid of a library of fluorescence spectra of more than 60 different mineral oils (Ref.3). The well known crosscorrelation techniques showed a a good potential in the identification of the oil class (crude, light, heavy) but require the detection of the complete spectrum and a long data processing. An original technique was developed which gives the same results as the crosscorrelation techniques with the use of two properly selected fluorescence wavelengths. With more than two wavelengths this technique allow a discrimination inside the class.

4. THE SYSTEM

The FLIDAR 2 (Ref.11) is the first lidar fluorosensor having a high spectral resolution, and it is based on a new idea in remote sensing of the environment because it operates at the same time as a lidar fluorosensor and a passive spectrometer. The use of the same device for active and passive remote sensing allows a perfect comparison between the data and reduces weight and cost.

The FLIDAR 2 is divided in three modules:

SENSOR - This module contains the excitation laser, the receiving system, and a standard TV camera. The laser was expressly designed for this application and is composed of an excimer laser operating at 308 nm, and an excimer pumped dye laser. This solution gives an excitation wavelength which can be shifted from UV to the near IR. The receiving system is composed by a newtonian telescope, a grating spectrometer, and an intensified and gatable ccd array (fig.1).

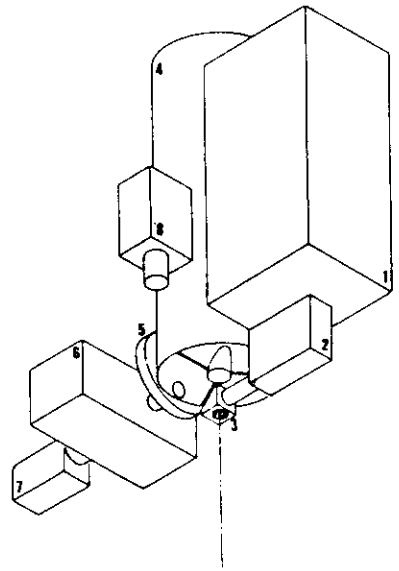

Fig.1 - Sensor Module. 1) Excimer laser, 2) dye laser 3)steering mirror, 4) telescope, 5) filter weel, 6) grating spectrometer, 7) ccd array.

CONTROL ELECTRONICS - This module contains the minicomputer which controls the acquisition, presentation, and recording of the data. It contains also the battery power supply and the TV recorder.

GAS HANDLING - This module is connected to the lidar only during the refilling of the excimer laser; this solution allows an important reduction of weigth and size during the field experiments.

The block dyagram of the FLIDAR 2 is shown on fig.2 and its characteristics are described in

table I.

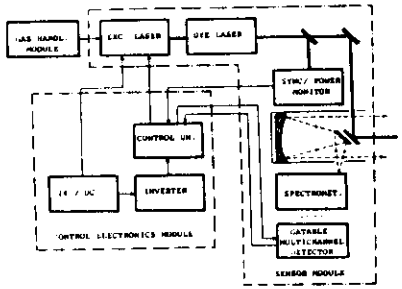

Fig.2 - Block dyagram of the FLIDAR 2

SENSOR MODULE (1x1.2x0.6 m, 84 kg)
Excimer Laser (Xe-Cl, 308 nm)
Pulse Energy 90 mJ Pulse Length 15 ns
Max prf 10 Hz
Dye Laser (Data depending from the dye)
Receiver System
- f:4, 250 mm Ø Newtonian telescope
- f:4 grating spectrometer with three gratings:
Dispersion (nm/mm) 3.0 6.0 24.0
Spect. range (nm) 37.5 75.0 300.0
- 512 elements, intensified, gatable ccd array
CONTROL ELECTRONICS MODULE (0.77x0.5x0.5 m, 63 kg)
- Console PAR OMA-3, 20 Mb hard disk and floppy
- Batteries, inverter, video recorder
GAS HANDLING MODULE (1.5x0.5x0.7 m)
- Gas cilinders, tubing, manometers
- Weight depending from the cilinders
POWER REQUIREMENTS
- 24 V dc, 30 A/h (laser), 63 A/h (elctronics) or 220 V, 50 Hz

Table I - Characteristics of the FLIDAR 2

the software packages stored in the control module allow the processing of the detected passive and active spectra in order to:
- Measure oil film thickness
- Identify oil spills
- Analyze the photosynthetic process in living plants

Fig. [illegible] - The FLIDAR 2 and its control module are particularly suitable for airborne use also with small aircrafts. Here the system is inside a Partenavia plane "Observer"

5. FIELD EXPERIMENTS

A first campaign of vegetation remote sensing was carried out at Wageningen (NL) in October 1986 (Ref.12) and a second one in a wood near Garderer (NL) in June-July 1987 (Ref.13), in both cases the FLIDAR 2 was based at ground (fig.4).

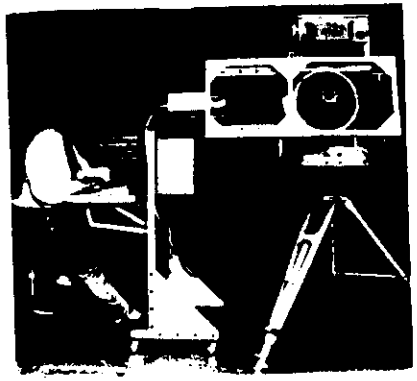

Fig.4 - The FLIDAR 2 in operation at Wageningen (October 1986)

The FLIDAR 2 operated at the same time as a fluorosensor and as a passive spectrometer (fig.5). The reflectance spectra, detected in the spectrometer operation, were used both for the subtraction of background from fluorescence spectra and for the evaluation of the leaf area index (LAI). The change of the fluorescence spectrum with the solar radiation intensity was investigated on Douglas firs and a good agreement was found between the intensity of the photosynthetic active radiation (PAR) and the ratio between the fluorescence emission at 685 nm and 730 nm (fig.6). These results confirmed the potential of laser fluorosensors in the detection of the photosynthetic process behavior in operational conditions.

A first campaign on natural waters was carried out in October 1987 in Tuscan coastal waters (Ref.14). The FLIDAR 2 was installed inside the research ship "Minerva" with the optical axis impinging on the water surface under an angle of about 10° (fig.7). Fluorescence and Raman spectra were detected in different water conditions like clear waters, harbors, river plumes, etc. (fig.8).

6. FUTURE IMPROVEMENTS

Also if the FLIDAR 2 is a very powerfull remote sensor its performances can be improved with a time resolved channel, for bathymetry and vegetation thickness measurement, a scanning mirror and an increased laser prf, for the use as an imaging lidar/spectrometer, and new software, for the extraction of informations on chemicals and other pollutants dissolved in water or floating over

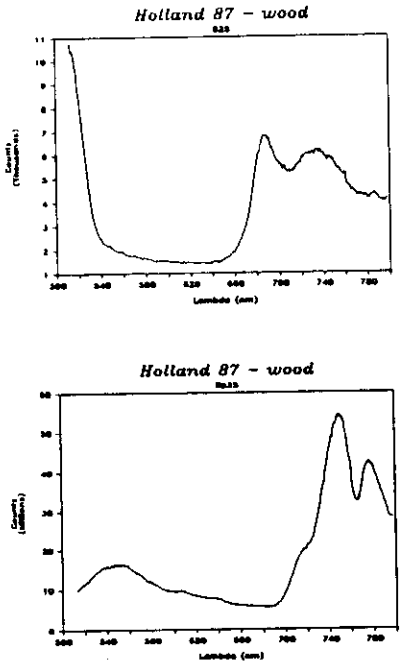

Fig.5 - Fluorescence spectrum (up) and reflectance spectrum (down) of a Douglas fir wood (Garderer, June 1987). Excitation wavelength 480 nm, distance of the target 60 m

the water surface. A particular attention will be devoted to the development of the appropriate software for the use of the FLIDAR 2 as a design tool for sensors, fluorescence lidars and spectrometers, for specific applications. In fact the high resolution spectra detected by the FLIDAR 2 can be used in order to simulate the performances of lower resolution systems for selecting the best working wavelengths for each application.

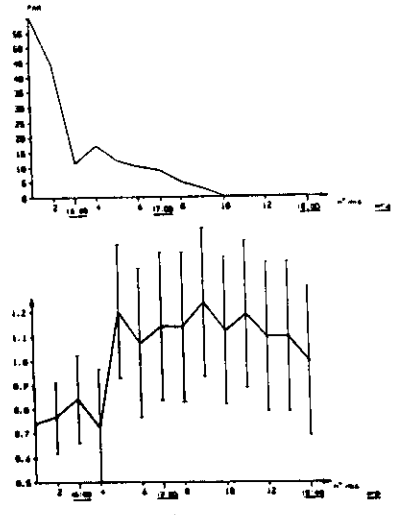

Fig. 6 - Behavior of the photosynthetic active radiation, PAR (up) and of the ratio between the two peaks of the laser induced fluorescence in Douglas firs. Measurements done around the sunset (Wageningen, October 1986), excitation wavelength 480 nm, distance of the target 50 m

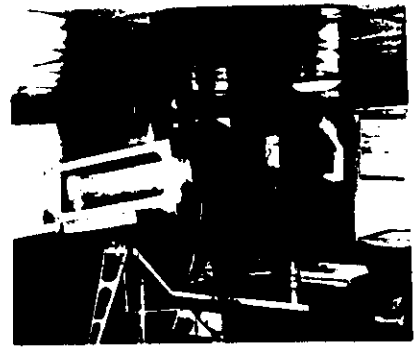

Fig.7 - The FLIDAR 2 inside the research ship "Minerva" during the field experiment in the Tuscan coastal waters (October 1987).

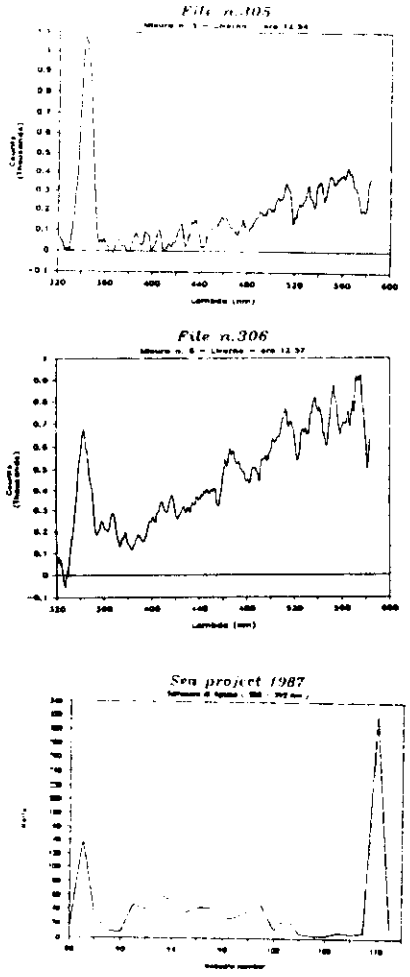

Fig. 3 - Fluorescence spectra detected during the field experiment on the "Minerva", excitation wavelength 308 nm. Up) Clear water. Center) Thin oil slick. Down) Ratio between the fluorescence in the band between 388 nm and 392 nm and Raman emission for a sery of spectra detected between Livorno and Migliarino, the peak corresponds to the Arno plume.

6. REFERENCES

1. Measures R.M. 1983 "Laser remote sensing" New York, John Wiley & Sons

2. Cecchi G., Pantani L., Pippi I., Magli R., Mazzinghi P. 1985 "Vegetation remote sensing: a new field for lidar applications" ECOOSA 84, SPIE Vol.492, 180, Bellingham, SPIE

3. Cecchi G., Pantani L., Mazzinghi P., Barbaro A. 1986 "Fluorescence lidar remote sensingof the environment: laboratory experiments for the chacterization of oil spills and vegetation" Laser Optoelectronics in Engineering, 660, Berlin, Springer Verlag

4. Cecchi G., Pantani L., Pippi I. 1986 ZLidar remote sensing of vegetation" Physics in Environmental and Biomedical Research, 375, Singapore, World Scientific Pub. Co.

5. Cecchi G., Fagotti C., Paoli P. 1985 "Misure di fluorescenza di clorofilla in vivo" Quaderni Metodologici n.4, Roma, CNR-IPRA

6. Romoli M. 1987 "Studio della fluorescenza di clorofilla in vivo stimolata da radiazione laser e sue applicazioni al telarilevamento della vegetazione" Dr.Thesis, Physics Dept., University of Firenze

7. Burlamacchi P., Cecchi G., Mazzinghi P., Pantani L. 1983 "Performance evaluation of UV sources for lidar fluorosensing of oil spills" App. Opt., 22, 48

8. Cecchi G., Mazzinghi P., Pantani L., Susini C. 1983 "Lidar investigation of oil films on natural waters" Optoelectronics in Engineering, 517, Berlin, Springer Verlag

9. Castagnoli F., Cecchi G., Pantani L., Pippi I., Radicati B., Susini C., Mazzinghi P., Barbaro A. 1985 "Remote sensing of oil on the sea: lidar and passive IR experiments" ESA SP233, 121, Paris, ESA

10. Barbaro A. 1987 "Lidar a fluorescenza: caratterizzazione di film inquinanti sulle acque naturali" Dr. Thesis, Physics Dept., University of Firenze

11. Castagnoli F., Cecchi G., Pantani L., Pippi I., Radicati B., Mazzinghi P. 1986 "A fluorescence lidar for land and sea remote sensing" Laser Technology and Applications, SPIE Vol.663, 212, Bellingham, SPIE

12. Cecchi G., Castagnoli F., Pantani L., Pippi I., Radicati B., Romoli M., Rosema A., Kliffen C., van Kooten O., van Hove L.W.A., Cortez P. 1987 "Results of the Itry out campaign" Delft, EARS

13. Cecchi G., Pantani L., Radicati B., Romoli M., Mazzinghi P. 1987 "Lift project June 1987", Firenze, IROE-CNR

14. Pantani L., Radicati B., Romoli M., Cannarsa S. 1987 "Progetto Mare 1987", Firenze, IROE-CNR